# Impurity Transport Study Using High-n Rydberg Spectroscopy at W7-X

By

Colin K. Swee

A dissertation submitted in partial fulfillment of

the requirements for the degree of

Doctor of Philosophy

(Nuclear Engineering and Engineering Physics)

at the

University of Wisconsin-Madison

2024

Date of final oral examination: 07/18/2024

The dissertation is approved by the following members of the Final Oral Committee:

Benedikt Geiger, Associate Professor, Engineering Physics

Cary Forest, Professor, Physics

Chris Hegna, Professor, Engineering Physics

Mark Nornberg, Associate Scientist, Engineering Physics

Carl Sovinec, Professor, Engineering Physics

# Acknowledgements

The work that I will present in the following pages was only possible thanks to a large number of people who have supported me on my journey as a student. It isn't possible to convey how thankful I am in this short forward though I will try.

I could not have gotten to where I am today without the love and support of my parents, Karl and Christine, as well as my sister Lauren. My sister is one of my best friends and someone I can talk to about anything. They say you can't pick who your family is, but I couldn't pick a better one if I tried. From an early age, I had a curiosity and excitement surrounding science and engineering. My parents fueled this by continuously supplying me with science themed children's books, erector sets, and after school activities. Every interest I developed throughout my childhood was wholeheartedly encouraged and supported by my entire family and for that I am eternally thankful. By the time I reached high-school, I was thoroughly hooked on physics and was searching for material to satisfy my curiosity about the universe. My physics teacher Michael Hamann saw this curiosity and lit a fire underneath it. Each Friday, we took a break from the curriculum to learn about a new mind-bending physics topic such as black holes, exotic states of matter, or quantum entanglement. Mr. Hamann's ability to convey such complex topics to a room of high-school students, while simultaneously imparting some of his own excitement about the natural world is one of the main reasons I chose physics as a career path. I consider myself lucky to have been taught by such a great educator.

I also want to acknowledge those who had a major impact on me during my time as an Undergraduate student since those first exposures to research guided me down the path I am currently on. Professor Amy Wendt offered me the privilege of working with her and gave me my first exposure to plasma diagnostic work. She

is an excellent mentor and taught me for the first time, how to work as a scientific researcher. Additionally, I want to recognize some of my greatest friends Micah and Elliot, who I spent most of my time with during my undergraduate years. The three of us together learned how to work hard, achieve our goals, and then take the time to relax and appreciate our successes. This mentality has helped me to never lose sight of what is important and gives me the energy to push myself towards new opportunities. We are all on such exciting trajectories for our careers, I am eager to see where we all end up!

Next, I would like to thank my advisor, Benedikt Geiger who, over the years, has mentored me in all areas of my research, provided excellent feedback on my analysis and writing, and has always helped me keep moving forward. Benedikt is a kind mentor who truly wants each of his students to succeed in whatever their goals may be. During my first couple years, his attentiveness and excitement for research helped jump-start my PhD topic allowing me to carry my momentum into the second half of my degree. Additionally, my time as a PhD student would not have been nearly as enjoyable without such an excellent cohort of fellow students. Our after-work get-togethers and lunchtime card games provided a much needed breather from the day to day grind of doing academic research. There are too many names to list here but each student that I shared my graduate experience with was kind, uniquely interesting, and remarkably intelligent. I am thankful to have worked in Benedikt's research group and am excited to see the results of everyone's ongoing research topics. I would also like to thank Santhosh Kumar, who provided me with significant guidance during my first couple years learning plasma diagnostic procedures at HSX as well as Mark Nornberg who, in the last couple years, has been willing to discuss anything on the topics of impurity transport and Bayesian analysis. In addition, I recognize all of the hard work and expertise that the professors in the Nuclear Engineering, Electrical

Engineering, and Physics departments provide via the excellent curriculum that goes along with the doctoral program.

Finally, I want to thank my soon to be wife, Angela, who undoubtedly has had the greatest impact on me over the last 6 and a half years. Every day when I come home from work, any worries I might have are washed away when I walk through the door and see her there to greet me along with our two goofy dogs. Angela is an excellent researcher in her own work and amazes me with her intelligence, hard work, and professionalism. By sheer proximity, I think some of these qualities have rubbed off on myself, allowing me to apply them to my own work. As my partner in life, Angela is always there to cheer for my successes, help me learn from my failures, and comfort me in times of great stress. She makes me a better person in every way and I would not have been able to achieve this great accomplishment without her. I am as excited about her future as I am about mine and cannot wait to see what adventures await us next.

*I am blessed to have such a wonderful set of friends, family, and mentors. Thank you all so much.*

**Abstract**

Impurities will play a significant role in the plasma environments found inside fusion reactors. For example, accumulation of light impurities such as helium ash from fusion reactions can dilute the fuel mixture and reduce overall fusion rates. In the case of highly ionized heavy impurities, inner shell electrons undergo strong line transitions which radiate away the thermal plasma energy. To avoid such scenarios, a detailed understanding of impurity transport in fusion plasma is necessary. This dissertation describes novel work done on the W7-X stellarator to both measure impurity radiation and model impurity transport.

At W7-X, a new charge exchange recombination spectroscopy (CXRS) diagnostic is used to measure heavy impurities injected using the laser blow off (LBO) method[1]. This system was designed with improved photon throughput and speed compared to the existing CXRS system at W7-X and installed for the most recent experimental campaign (OP 2.1). To analyze the CXRS measurements, a novel approach has been developed for the determination of impurity densities based on the observation of visible wavelength, high-n Rydberg-like transitions of highly ionized heavy impurities. These emissions provide several benefits including simple line identification and a lack of passive emission components.

The diagnostic measurements are forward modeled using a python framework consisting of the pySTRAHL impurity transport code[2] and the Monte Carlo neutral simulation code known as pyFIDASIM[3]. By using Bayesian inference to match the modeled signals to experimental measurements, impurity diffusion and convection velocities can be determined. Additionally, an integrated data analysis framework has been developed to self consistently model multiple complementary impurity diagnostics. By evaluating the inference un-

certainty for the impurity transport when considering different combinations of diagnostics, a better understanding of the importance of each measurement is developed. Finally, the inferred impurity transport is found to be in qualitative agreement with theoretical calculations of turbulent impurity transport indicating pinch contributions to the total flux. The presented techniques are now readily available and can be applied to upcoming experimental campaigns.

# Contents

# 1 Introduction

## 1.1 Fusion Plasma

Nuclear fusion has been long desired due to its promise of providing an abundant and clean energy source. At the atomic scale, fusion-energy is released when two light nuclei overcome their electrostatic repulsion and combine into a new, heavier element. The fusion process has fueled our sun for billions of years and provides enough power to sustain life on our planet almost 100 million miles away. However, harnessing fusion on earth for the purposes of controlled energy production is still being actively researched by modern physicists.

The most common candidate for a fusion fuel is a mixture of the Hydrogen isotopes, Deuterium and Tritium which can undergo the following nuclear reaction:

$$^3T +^2 D \rightarrow {}^1n\,(14.1\,\mathrm{MeV}) +^4 He\,(3.5\,\mathrm{MeV}) \tag{1}$$

D-T fusion is typically considered due to the relatively large fusion cross section compared to other fuel candidates. Figure 1 shows a summary of various fusion cross sections.

In order to facilitate the fusion reaction, the fuel of choice must be contained within a given volume at an extreme temperature. In such conditions, the thermal energy is high enough that electrons are liberated from nuclei creating a plasma. The exact distinction between a plasma and a partially ionized gas can vary, though one of the more accepted definitions is that it (usually) exhibits quasi-neutrality over the bulk of the plasma and experiences collective behavior. Quasi-neutrality is the idea that if any one region of the plasma accumulates a net charge due to the build up of either ions or electrons, fields will naturally develop to move electrons to neutralize

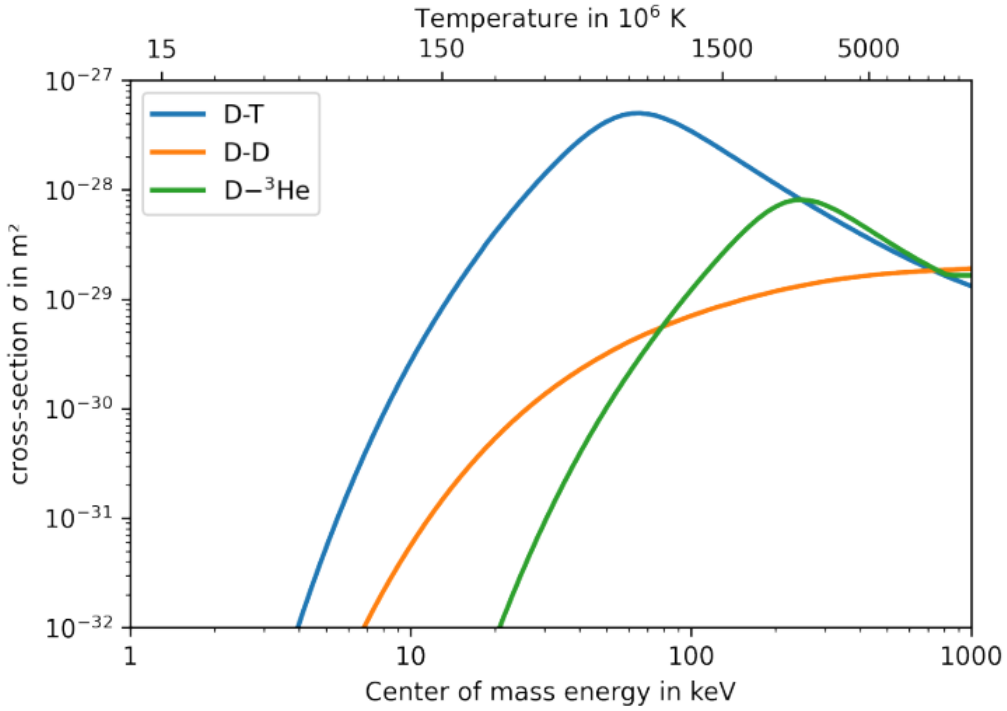


Figure 1: Fusion cross sections as a function of collision energy for three potential fueling approaches. Figure credit [4].

that charge. The effect is that on a macroscopic scale, any particular volume with a size larger than the so-called Debye length, $\lambda_D = k_B T/4\pi n z^2$, has zero net charge. Here, $k_B$ is the Boltzman constant, $T$ and $n$ are the plasma temperature and density, and $z$ is the charge of the individual species. Note that exotic non-neutral plasmas can be generated in laboratory experiments or in the boundary regions between the main plasma and a solid surface known as the sheath. Collective behavior is the idea that long range Coulomb interactions can couple the dynamics of plasma volumes separated by large distances[5], leading to many complicated physical phenomena such as self generating electric and magnetic fields or collisionless plasma waves.

To generate net power in a fusion reactor, the power lost to radiation and transport must be outweighed by the power generated using external heating schemes and

fusion reactions. This power balance depends on the plasma density $n$ and the temperature $T$, which will determine the fusion rate. One also needs to consider the energy confinement time $\tau_E$, which accounts for power loss due to both transport and radiative processes. These contributions to the power balance are described by the "triple-product", defined as $nT\tau_E$. It is expected that the minimum triple product value for which net energy can be generated is $\sim 3 \times 10^{21}$ keV s/m$^3$. [6].

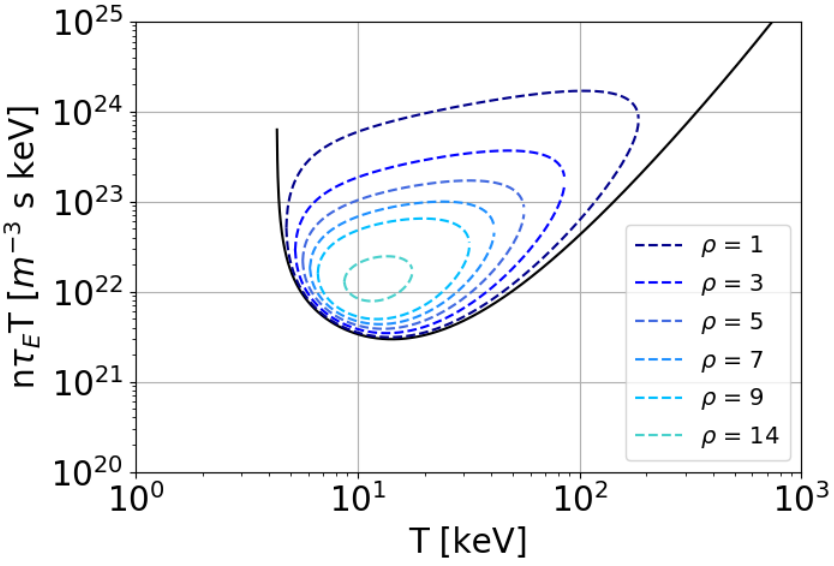


Figure 2: Burn curves for a deuterium-tritium plasma. Inside of the curves, $\alpha$ heating exceeds power losses. The size and shape of the curves additionally depend on the particle confinement time to energy confinement time ratio: $\rho = \tau_p/\tau_E$. When this ratio is zero, we recover the triple product condition when neglecting helium ash. Fusion cross section credit: [7].

The basic triple product treatment however, tends to neglect the effect of fuel dilution due to the accumulation of helium ash, the thermalized alpha particles which remain in the fusion plasma. If particle confinement is too high, helium accumulates and reduces the efficiency of fusion reactions. Taking into account the effect of the particle confinement time, $\tau_p$, one can perform a similar power balance approach [8]. In this case, rather than setting a lower bound on the necessary $n\tau_E T$, burn

contours are identified inside which $\alpha$ heating exceeds power losses. Increasing ratios of particle to energy confinement times, $\rho = \tau_p/\tau_E$, reduces the size of the parameter space in which one expects positive net power. This can be seen in Fig. 2 where large values of $\rho$ exhibit fuel dilution and reduced fusion efficiency. One can also recover the prediction of the simplified triple product by considering the case where $\rho = 0$ (shown by the open black curve).

In addition to the buildup of helium ash, heavier impurities can enter the fusion plasma from erosion of first wall materials (Carbon, Iron, Tungsten, etc.). In some cases, impurities are deliberately injected to mitigate heat fluxes onto exhaust tiles [9, 10, 11] or to interrupt the formation of catastrophic instabilities [12, 13, 14]. Therefore, attention must be given to prevent their buildup, particularly in reactor concepts that utilized long-pulse or steady state plasmas. The main way by which heavy impurities negatively impact reactor performance by radiating away thermal energy. The two main radiative power loss mechanisms are radiation from line transitions and Bremsstrahlung. Line transitions occur when an impurity ion is excited following ionization, recombination, electron impacts, or charge exchange. As the ion relaxes to a lower energy level, a photon is emitted, carrying with it the energy that used to be contained in the kinetic energy of the plasma. Heavy impurities tend to radiate in the high energy X-ray range and act as a strong loss channel for plasma energy. In addition, since impurities can ionize several times, they can significantly increase the number of free electrons in the plasma. The increased electron density in turn leads to an increase in the so-called Bremmstrahlung emission which occurs as a charged particle undergoes acceleration (in this case the acceleration experienced due to Coulomb collisions with neighboring ions/electrons). An example of a fusion plasma which experiences impurity accumulation and subsequent radiative collapse is given in figure 3.

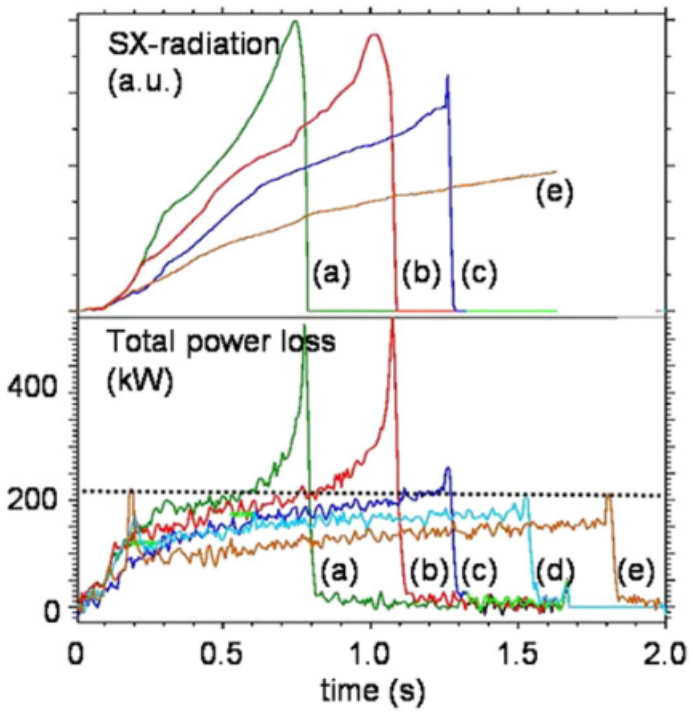


Figure 3: Measured impurity radiation in several W7-AS discharges. Electron densities increase from (e) to (a) indicating unfavorable impurity confinement for higher density plasmas and illustrates the mechanism for the stellarator density limit. For experiments (a), (b), and (c) the radiation becomes so intense that the discharge terminates prematurely. Figure credit: [15]

The net radiated power can be characterized by the so-called cooling rate coefficients, $L_z$ which describe the power loss per impurity density and electron density [16]. Adding this factor to the Lawson criterion power balance, one can once again generate burn contours. An example of such a calculation which considers various Xenon concentrations is given in figure 4. In this case, the parameter space suitable for positive net power is additionally reduced by an increase in the Xenon concentration.

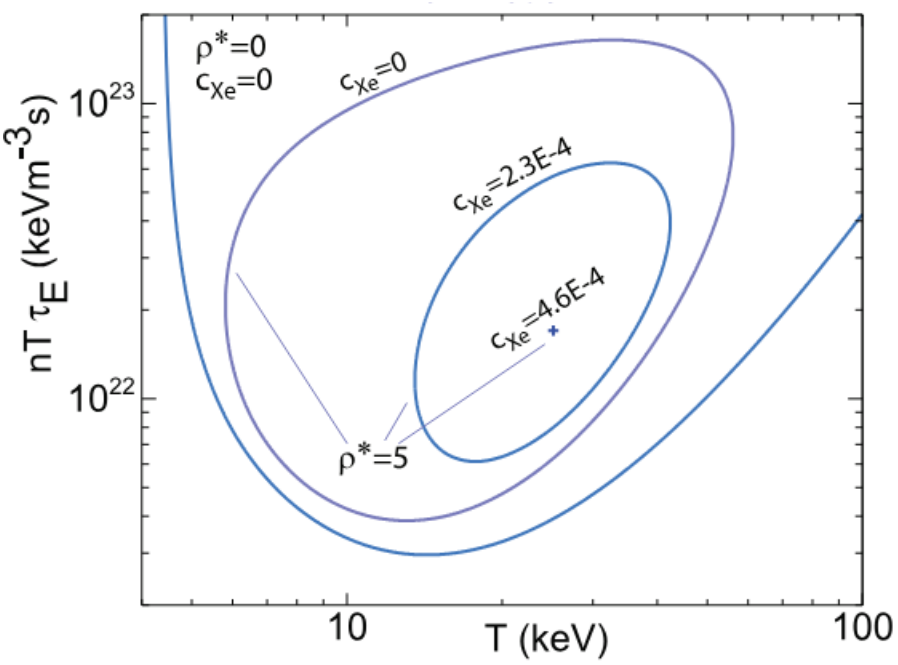


Figure 4: Burn curves for a deuterium-tritium plasma containing a varying concentration of Xenon impurities. Here, $\rho^*$ refers to the effective confinement time ratio taking into account recycling processes. Figures credit: [17]

## 1.2 Magnetic Confinement

As described in section 1.1, it is necessary to confine the plasma to a finite volume long enough to facilitate fusion reactions. This confinement is typically achieved by taking advantage of the response plasma species have to a carefully designed magnetic field. One consequence of plasma ions and electrons having a net charge is that in the presence of a magnetic field, they experience the Lorenz force as they move. This causes the particles to gyrate perpendicular to the magnetic field lines effectively confining them to motion along the field. To prevent losses along the field direction one can utilize closed magnetic topologies such as a torus.

In magnetic confinement devices the force balance equation describes the relation between the pressure gradient $\nabla p$, the current density $j$ and the magnetic field:

$$\vec{\nabla} p = \vec{j} \times \vec{B} \tag{2}$$

One can immediately see that in this equation, the balancing $\vec{j} \times \vec{B}$ force is in the direction of the pressure gradient. Additionally considering that $\nabla \cdot \vec{B} = 0$, this implies surfaces of constant pressure parallel to the confining field. These nested "flux surfaces" are defined as smooth surfaces such that: $\nabla \vec{B} \cdot \vec{n} = 0$ everywhere on the surface. Here, $\vec{n}$ is the surface normal.

A given surface is commonly labeled by its enclosed magnetic flux, either in the toroidal or poloidal direction:

$$\Psi = \int_{S_p} \vec{B} \cdot \vec{n} dS, \tag{3a}$$

$$\Phi = \int_{S_t} \vec{B} \cdot \vec{n} dS. \tag{3b}$$

In the case of toroidal flux, $\Phi$, the surface which the magnetic flux passes through is simply a poloidal cross section. In the case of toroidal flux, $\Psi$, it would be a ribbon which extends around the torus (see Fig. 5). In most cases, these fluxes change monotonically as one moves further from the magnetic axis.

Additionally, since charged particles will tend to stream along the magnetic field lines at thermal velocities, transport on a flux surface is generally much faster than perpendicular transport. For this reason, many plasma characteristics such as temperature and density equilibrate very quickly along these surfaces and are known as "flux functions".

Naively, one might expect charged particles to be perfectly confined to flux surfaces as they mainly stream along the field lines. However, additional dynamics are brought on when considering a toroidal geometry. Specifically, the curvature and the $\nabla B$ drifts

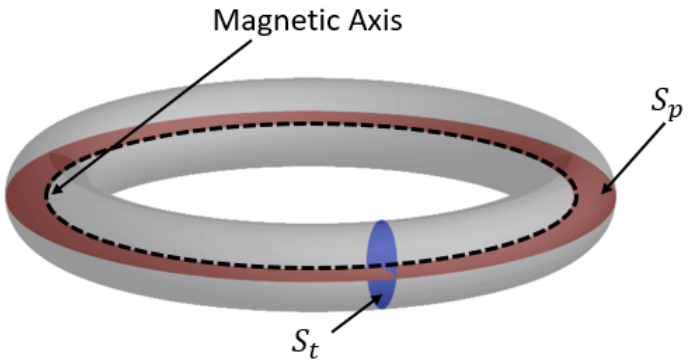


Figure 5: Surfaces used to evaluate toroidal and poloidal fluxes for a given flux surface. Toroidal flux is measured as passing through the cross section shown in blue (marked $S_t$). Poloidal flux is measured as passing through the ribbon shown in orange (marked $S_p$). Figure adapted from [18]

cause particles to deviate from a given flux surface with the following drift velocities:

$$\vec{v}_{\nabla B} = \frac{K_\perp}{qB}\frac{\vec{B}\times\nabla B}{B^2}, \tag{4}$$

$$\vec{v}_k = \frac{2K_\parallel}{qB}\frac{\vec{R}_c\times\vec{B}}{R_c^2 B}. \tag{5}$$

Here, $K_\perp$ and $K_\parallel$ are the kinetic energies perpendicular and parallel to the field, $q$ is the particle charge and $R_c$ is the radius of curvature of the magnetic field lines. In a purely toroidal geometry, the combination of these two drifts can lead to a vertical displacement of electrons and ions. To suppress the net effect of these drifts, a rotational transform, $\iota$ is introduced which causes streaming particles to move helically around the torus and sample both inboard and outboard regions [19].

When considering how to induce a rotational transform in a toroidal fusion device, two strategies arise which characterize the two most common reactor designs: tokamaks and stellarators. In tokamaks, the rotational transform is mainly generated

by an axial current which creates a poloidal field component via ampere's law:

$$\mu_0 J_z \hat{z} = \nabla \times \vec{B} = \frac{1}{r}\frac{\partial}{\partial r}(rB_\phi)\hat{z} - \frac{1}{r}\frac{\partial B_r}{\partial \phi}\hat{z} \tag{6}$$

This axial current is typically driven by ramping up current in a large solenoid located in the center of the torus.

In the case of modern stellarators, 3D shaping is used to elongate the plasma and rotate the flux surfaces poloidaly as one moves in the toroidal direction [20]. Additionally, there is the possibility to induce a rotational transform by allowing the magnetic axis to be non-planar as is the case for many modern optimized stellarators. More generally, the rotational transform can be described by the toroidal and poloidal fluxes via:

$$\iota = \frac{\iota}{2\pi} = \frac{1}{\mathbf{q}} = \frac{d\Psi}{d\Phi} \tag{7}$$

Here, $\mathbf{q}$ is the safety factor commonly used in the tokamak context (denoted with bold text to distinguish from the particle charge q).

One advantage of the stellarator compared to the tokamak is that since one does not need to ramp a current in a central solenoid to achieve a rotational transform, they can in principle operate in steady state. However historically, stellarators tend to have heightened transport compared to tokamaks due to a phenomenon known as neoclassical transport (described in more detail in section 2.2)[21]. Modern stellarators have found a solution to this issue through the optimization of the magnetic field shape which largely dictates the transport properties. Examples of optimized stellarators are HSX in Madison, Wisconsin, W7-X in Greifswald, Germany, and NCSX in Princeton, New Jersey.

The previous section described the importance of impurities in fusion plasmas. Since these impurities also respond to the confining fields, it is important to keep in mind that well confined plasmas risk the possibility of impurity build up. This concern is the main focus of this work which aims to characterize the transport of heavy impurities in plasmas at the W7-X stellarator.

## 1.3 Overview of Dissertation Work

This dissertation describes the methods used to determine impurity diffusion and convection profiles in W7-X plasmas for injected iron particles. Several experimental efforts have been made to understand impurity transport in stellarators already [22, 23, 24] however, not much attention has been given to accurately determining the impurity convection velocity or to the uncertainty in the inferences. The goal of this work is to address these issues via an integrated data analysis approach based on Bayesian inference techniques.

Chapter 2 will discuss the various mechanisms by which impurities may experience net radial fluxes. Within this chapter, section 2.1 describes the classical transport picture based on collisions that displace impurity ions by a distance comparable to their gyroradii. Section 2.2 explains the various "neoclassical" transport mechanisms that appear when one considers a 3D toroidal magnetic field. Finally Section 2.3 gives an overview of the relevant turbulent transport mechanisms due to instabilities in W7-X.

Next, Chapter 3 provides an overview of the experimental setup at W7-X. Sections 3.1, 3.2, and 3.3 give an introduction to the stellarator design and describe the characteristics of its magnetic geometry and scrape off layer (SOL) region. Section 3.4 discusses the various heating schemes used to generate plasma while section 3.5

introduces several diagnostics that are important for diagnosing the main plasma species as well as the impurity ions.

Chapter 4 summarizes one of the main deliverables of this dissertation work, the design and implementation of five dual channel spectrometers which were installed at W7-X to make charge exchange recombination spectroscopy (CXRS) measurements of impurity emissions. In sections 4.1 and 4.2, the line of sight setup and a detailed description of the spectrometer design is given. Next, sections 4.3 and 4.4 discuss various techniques necessary to calibrate the system and analyze data.

Chapter 5 discusses the collected CXRS data along with a description of the unique "high-n" Rydberg transitions which were chosen for further analysis. The analysis of such emissions for impurity transport studies has not been investigated significantly in the past and therefore this work provides description of the novel technique.

Chapter 6 gives a full description of the computational tools developed to model the impurity transport in python. First, section 6.1 gives a general introduction to Bayesian inference which is the main tool used to infer the impurity transport by comparing the synthetic signals to the measured data. Additionally, the aspects of the Bayesian statistical model which are specific to the model considered here. Then, section 6.2 describes the forward model that is used to simulate impurity charge exchange emission.

Chapter 7 describes the various results from the Bayesian inferences. First, an introduction to the experimental conditions is given along with a summary of the collected diagnostic signals in section 7.1. Then, in section 7.2 the inference of impurity transport profiles is presented along with a discussion of how the inclusion of multiple diagnostics via self consistent synthetic diagnostics affects the final uncertainties in the impurity transport.

Finally, chapter 8 gives a summary of the work highlighting the major conclusions,

open questions, and areas where future work can be conducted.

# 2 Impurity Transport in Stellarators

Cross field impurity transport in fusion devices can typically be characterized by three categories, classical, neoclassical, and anomalous. Classical transport theory describes the collisional transport of many gyrating particles in the presence of background gradients while neoclassical theory considers dynamics that arise when considering the effect of those particles as they traverse 3D shaped magnetic fields with curved field lines. Finally, transport mechanisms not described by classical or neoclassical contributions are considered to be anomalous and are typically attributed to plasma turbulence. The theory behind each of these types of transport will be discussed in the following pages.

## 2.1 Classical Transport

Particles with electric charge $q$, mass $m$, and a velocity perpendicular to the magnetic field, $v_\perp$ will experience a Lorenz force. For this reason, they are confined to gyrate around a given field line with strength $B$. As particles undergo collisions, they migrate according to a random walk for which the step size would be the Larmor radius, $\rho = mv_\perp/(|q|B)$. The corresponding diffusive particle flux can be expressed as $\Gamma_F$:

$$\Gamma_{cl} = -D_{cl}\nabla n. \tag{8}$$

Here, $n$ is the particle density and $D_{cl}$ is the diffusion coefficient where $D_{cl} \sim \rho^2\nu$ and $\nu$ is the collision frequency of the plasma species. The majority of collisional transport is via collisions between electrons and ions with an estimated frequency $\nu_{ei}$ of [5]:

$$\nu_{ei} = 2 \times 10^{-6} \frac{Z n_e ln\Lambda}{T_e^{3/2}} \quad s^{-1}. \tag{9}$$

Here, all quantities are in cgs units except for temperature which is in electron volts. $T_e$ and $n_e$ are the electron temperature and density, $Z$ is the ion charge, and $ln\Lambda$ is the Coulomb logarithm. Since typically the Larmor radius is small ($\sim$ few mm), $D_{cl}$ is small compared to other transport channels.

## 2.2 Neoclassical Transport

In simplest terms, neoclassical transport refers to the added dynamics brought on by considering a toroidal magnetic field geometry. Specifically, as particles traverse along field lines, a certain fraction can be trapped in so-called "banana orbits". Much like in the case of a magnetic mirror, particles with sufficiently low parallel velocity have the tendency to be reflected back along their field lines as they move into regions of higher field strength. In the case of tokamaks, this occurs as particles traverse from the outboard side to the inboard side of the torus. The path of these reflected particles will have some radial excursion determined by the particle drifts described in equations 4 and 5. In tokamaks, the total radial excursion averages out to zero over the entire trajectory of the reflecting particle and when projected onto a poloidal cross section, the path somewhat resembles a banana in shape (hence the name). In the case of stellarators however, particles have the additional possibility of being trapped inside helical magnetic wells and, in contrast to the tokamak case, the net radial drift does not necessarily average to zero. This leads to particles that drift out of the confined region after only several reflections and are characterized as "direct" losses. The goal of many optimized stellarators then is to engineer the magnetic geometry to retain the net zero radial drift condition known as omnigeneity[25].

Ultimately, radial neoclassical transport is dominated by collisions which kick particles into and out of trapped velocity space. Collisions will cause particles to

experience a random walk in *velocity* space with a diffusion coefficient,

$$D_v \sim (\Delta\Theta)^2 / t = (\Delta\Theta)^2 \nu, \tag{10}$$

where $\nabla\Theta$ represents a random walk change in the trapped particle pitch angle.

It is important to note that the collision frequency between electrons and ions defined in equation 9 is actually defined as the average rate for a particle to scatter 90 degrees in velocity space (i.e. $\Delta\Theta \sim \pi/2$). This is because the vast majority of collisions are grazing at small angles and therefore only their cumulative effect after many collisions is relevant. In the case of trapped particles however, for small angle collisions to significantly contribute to transport, the cumulative effect only needs to change in velocity space enough to become untrapped. This is a less strict condition than the case of 90 degree scattering and only requires a deviation in velocity space by $\Delta\Theta \sim (2\Delta B/B)^{1/2} \sim (2\epsilon)^{1/2}$ [26]. Here, $\Delta B/B$ is the magnetic well depth which, in tokamaks is proportional to the inverse aspect ratio, $\epsilon$. Therefore, the effective time to scatter out of trapped particle space is smaller than the 90 degree scattering. Considering equation 10, for the case of 90 degree scattering and detrapping scattering, one can solve for the effective collision frequency for detrapping[26]:

$$\nu_{eff} \sim \nu_{ie} \left( \frac{\pi/2}{(2\epsilon)^{1/2}} \right)^2 \sim \nu_{ie}/\epsilon. \tag{11}$$

Typically, neoclassical transport is split into three separate collisionality regimes. At low collisionality or the so-called "long mean free path" regime, trapped particles are capable of undergoing many reflections before detrapping. In the case of tokamaks and perfectly omnigenous stellarators, banana orbits are confined such that the radial drift velocities average to zero over a full bounce period. In this scenario, the diffusive

step size is determined by the banana width, $\delta_{ba} \sim \frac{\mathbf{q}\rho}{\sqrt{\epsilon}}$, which is much larger than the Larmor radius that characterizes classical diffusion (since $\epsilon << 1$). Here, $\mathbf{q}$ is the safety factor and $\rho$ is the Larmor radius. The diffusive time step is then the effective collision time $\tau_{eff} = 1/\nu_{eff}$. Additionally, one also needs to take into account the fraction of particles which are trapped since they govern the radial transport. This is characterized by an additional factor of $\langle f_{tr} \rangle \sim \sqrt{\epsilon}$ which indicates that the sub-population of particles which are trapped experience the diffusive flux. One can then estimate the diffusion in the so-called "banana" regime:

$$D_{ba} = \frac{\delta_{ba}^2}{2\tau_{eff}} \langle f_{tr} \rangle \sim \frac{\mathbf{q}^2 \rho^2}{\epsilon^{3/2}} \nu \tag{12}$$

In stellarators, where the trapped particle fraction is decoupled from the aspect ratio, the trapped particle fraction is instead characterized by the quantity $\epsilon_h$ which is the helical ripple (i.e. the local well depth along a field line). However, the quantity, $\epsilon_{eff}$ is used in general to describe the uniformity of the magnetic wells which trap particles and therefore their confinement quality [27] and can be used analogously to the inverse aspect ratio from the tokamak case. Since this work focuses on transport measurements in stellarators, the remaining neoclassical transport equations will use $\epsilon_{eff}$.

In most stellarators, some or all of the trapped particles *do* have net radial drifts over their bounce periods. In these cases the diffusive step size is instead determined by the radial distance these trapped particles drift before experiencing a de-trapping collision ($\delta_{1/\nu} \sim v_d \tau_{eff}$). This scenario is referred to as the $1/\nu$ regime due to its inverse dependence on the collision frequency. Considering the relevant diffusive step

size we can again estimate the diffusion:

$$D_{1/\nu} = \frac{\delta_{1/\nu}^2}{2\tau_{eff}} \langle f_{tr} \rangle \sim \frac{v_d^2 \epsilon_{eff}^{3/2}}{\nu} \propto \frac{\epsilon_{eff}^{3/2} T^{7/2}}{nB^2 R^2} \tag{13}$$

Where $T$ is the particle temperature, $n$ is its density, $B$ is the field strength, and $R$ is the major radius on axis. Because of the strong temperature scaling in the $1/\nu$ regime, it is expected that neoclassical transport contributions will dominate at low collisionality and high electron temperatures. This is indeed seen to be the case in previous W7-AS plasma experiments [28].

Note that even though modern optimized stellarators are close to perfectly symmetric, deviations from symmetry can lead to net radial drifts[29, 30]. For this reason, even a small fraction of particles with net radial drifts are sufficient to dominate the transport. Therefore, all modern, currently constructed, stellarators exhibit $1/\nu$ scaling in the long mean free path regime. Despite this, recent simulation work has found that there is the potential for future optimized stellarator configurations which deviate from perfect symmetry by field amplitudes comparable to the ambient geomagnetic field [31].

In the very collisional case, which is typically relevant for impurities, neither trapped nor passing particles can complete their full transits. Here, the radial excursion due to particle drifts is what determines the transport. We first consider the radial drift velocity, $v_{Dr} \approx mV_\parallel^2/eBR$ and the time it takes to complete a full passing orbit, $\tau_{pass} \sim L_{pass}/V_\parallel \sim Rq/2V_\parallel$. Here, $V_\parallel$ is the parallel velocity of the particle (typically taken to be the thermal velocity) and $R$ is the major radius of the torus. Combining these, we get an approximation for the maximum radial excursion: $\delta_{P.S.} \sim mV_\parallel q/eB = \rho q$. Additionally, we no longer care about the fraction of trapped particles so we revert to the usual collision time as the diffusive time step. In this

highly collisional case, known as the Pfirsch-Schlüter regime, the diffusion can then be estimated as:

$$D_{P.S.} = \frac{\delta_{P.S.}^2}{2\tau} \sim \nu\rho^2\mathbf{q}^2 \tag{14}$$

Between the long mean free path and the high collisionality regimes, there exists a regime where trapped particles cannot complete their orbits but passing particles can. This so-called plateau scenario bridges the low collisionality (either $1/\nu$ or banana) case and the fluid like Pfirsch-Schlüter regime. The diffusion in the plateau regime can be identified by considering the value of the diffusion at the boundary of the low and high collisionality regimes. The upper end of the banana regime occurs when the effective collision frequency is equal to the banana bounce frequency, $\omega_B$:

$$\nu^* = \frac{\nu_{eff}}{\omega_B} = \frac{\nu\mathbf{q}R}{V_\parallel\epsilon^{3/2}} = 1 \tag{15}$$

Here, $\nu^*$ is referred to as the collisionality and is the metric which is typically used to determine which collisional regime the plasma is in. Using this value for $\nu$ ($\nu_{eff}$) in equation 12 we get $D = \rho^2 V_\parallel q/R$. For Pfirsch-Schlüter diffusion, the lower bound occurs when the collision time is equal to the passing particle orbit time:

$$\frac{\nu}{\tau_{pass}^{-1}} \sim \frac{\nu R\mathbf{q}}{V_\parallel} = \nu^*\epsilon^{3/2} = 1 \tag{16}$$

Solving for $\nu$ and plugging into equation 14 then gives $D = \rho^2 V_\parallel \mathbf{q}/R$, the same as for the banana regime case. This then implies that the diffusion is constant for $1 < \nu^* < \epsilon^{-3/2}$. The plateau regime diffusion is then approximately:

$$D_{plateau} \sim \rho^2 V_\parallel \mathbf{q}/R \tag{17}$$

In reality, the boundaries between the different collisionality regimes are not well defined and contributions from each can contribute to total particle transport. For this reason, codes which solve the linearized drift kinetic equation (DKE) are applied to calculate the diffusion as a function of collisionality. The linearized DKE is[32]:

$$-\frac{dr}{dt}\left(\frac{1}{n}\frac{dn}{dr}-\frac{qE_r}{T}+\left(K-\frac{3}{2}\right)\frac{1}{T}\frac{dT}{dr}\right)f_M+pvB\frac{q\langle\mathbf{E}\cdot\mathbf{B}\rangle}{T\langle\mathbf{B^2}\rangle}f_M=\mathcal{V}\left(f_1\right)-v\mathcal{L}\left(f_1\right). \tag{18}$$

Here, $K$ is the normalized kinetic energy, $mv^2/2T$, $f_M$ is the Maxwellian particle distribution function, $f_1$ is a small deviation from $f_M$, $\mathcal{V}$ is the Vlasov operator, and $v\mathcal{L}$ is the Lorentz pitch-angle scattering operator.

An example of such a calculation done for the W7-X stellarator is given in Fig. 6 where the three collisionality regimes are designated via color. Here, one can see the characteristic $1/\nu$ regime depicted by the dark blue line in the shaded blue region. The plateau and Pfirsch-Schlüter regimes are then approximately in the orange and yellow shaded regions.

For stellarators, an additional effect needs to be considered in the long mean free path regime where fluxes are not necessarily ambi-polar. For example, at similar temperatures, ions have a much lower collision frequency compared to electrons due to their larger mass and equation 13 predicts that their diffusive flux will be much higher in the $1/\nu$ regime. To conserve quasineutrality, these fluxes must balance. This is accomplished by a radial electric field which develops and introduces a poloidal $\vec{E}\times\vec{B}$ rotation. Ions are then advected into regions with lower mirror ratios and become detrapped, therefore reducing the ion transport[27]. When solving the ambipolarity condition $\Gamma_e=\Gamma_i$, up to three solutions can be found for the electric field; one where $E_r<0$ known as "Electron root", one where $E_r>0$ known as "ion root", and a third solution which is unstable. The net effect of increasingly large $E_r$ on the diffusion

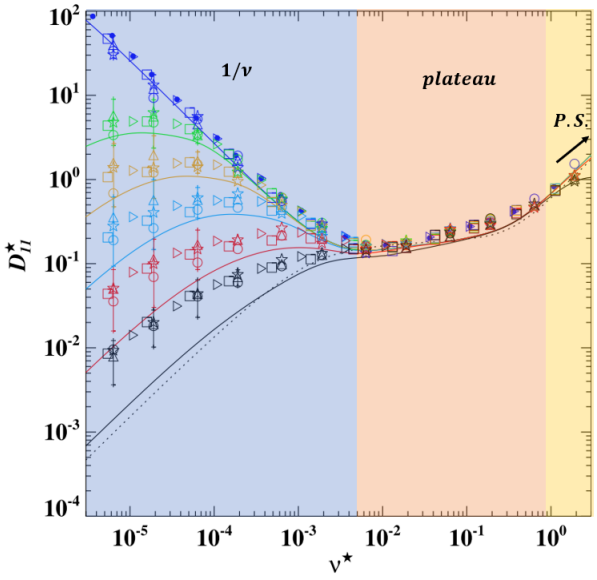


Figure 6: Calculated neoclassical diffusion coefficient for the W7-X stellarator. The effect of an increasingly large electric field can be seen in the $1/\nu$ regime where the dark blue data points correspond to $E_r = 0$ and black corresponds to the largest $E_r$. Additionally shown in the dashed gray line is the diffusion for an equivalent tokamak where the long mean free path regime follows the banana regime scaling. Figure adapted from reference [32]

.

coefficient can be seen in the $1/\nu$ regime shown in Fig. 6 where the ion transport is reduced to balance the electron transport.

The discussion of neoclassical transport up until this point has considered only diffusive contributions arising from "random walk" like collisions. However if one were to fully solve the DKE (equation 18), an additional convective term is present. Doing so allows one to solve for the so called neoclassical transport matrix and more generally, write down the neoclassical particle and heat flux:

$$\vec{\Gamma_{nc}} = -n \left\{ D_{11}\left(\frac{\nabla n}{n} - \frac{q\vec{E_r}}{T}\right) + D_{12}\frac{\nabla T}{T} \right\}, \tag{19}$$

$$\vec{q_{nc}} = -nT \left\{ D_{21}\left(\frac{\nabla n}{n} - \frac{q\vec{E_r}}{T}\right) + D_{22}\frac{\nabla T}{T} \right\}. \tag{20}$$

Here, $D_{11}$, $D_{12}$, $D_{21}$, and $D_{22}$ are elements of the neoclassical transport matrix. In the particle flux equation, one recovers the expected diffusive contribution which is proportional to the density gradient, however, two more terms appear which are proportional to the density. These are the so-called neoclassical convection terms the first of which is proportional to the radial electric field and the second of which depends on the temperature gradient (commonly referred to as thermo-diffusion). The overall particle flux considering both a diffusive and a convective term can then be rewritten as:

$$\Gamma = -D\nabla n + vn \; . \tag{21}$$

Considering particle conservation in the absence of particle sources and sinks,

$$\frac{\partial n}{\partial t} = -\nabla \cdot \Gamma, \tag{22}$$

equilibration along flux surfaces that are characterized by the radial coordinate $r$, and neglecting sources and sinks, one can turn equation 21 into an ordinary differential equation over the radial coordinate r:

$$\frac{\partial n}{\partial t} = \nabla \cdot (D\nabla n - vn) = \frac{1}{r}\frac{\partial}{\partial r} r(D\frac{\partial n}{\partial r} - vn) \; . \tag{23}$$

The transport equation of this form is general and relevant for scenarios (not necessarily just neoclassical transport) where there are both localized convective and diffusive contributions to the radial particle transport.

## 2.3 Turbulent Transport

In heat and particle transport contexts, any diffusive or convective flux that exceeds neoclassical predictions is considered to be anomalous. The most widely accepted

hypothesis is that the largest contribution to anomalous cross field particle transport is turbulence. Turbulence occurs in magnetized plasmas when an instability transfers energy into one or more spatial scales which is then nonlinearly transferred to many other spatial scales [33]. The sources of these instabilities can be either kinetic or magnetohydrodynamic (MHD) in nature. Notably, in toroidal magnetically confined plasma devices, core turbulence is usually driven by kinetic drift wave instabilities, in particular trapped electron modes (TEM), ion temperature gradient (ITG) modes, and electron temperature gradient (ETG) modes [34]. These modes are characterized by frequencies of 10s to 100s of kHz. While ITGs and TEMs generally occur on the ion gyroradius scale ($k_y\rho_i \lesssim 1$), ETGs occur on electron gyroradius scales ($k_y\rho_e \lesssim 1$). These instabilities are driven by radial pressure gradients.

The general picture of drift waves can be considered heuristically when one considers a slab like plasma with a pressure perturbation (in this case a sinusoidal like perturbation in the background density - see Fig. 7). Due to their fast response, electrons will then quickly equilibrate along field lines leading to a separation of charge and therefore the development of a radial electric field. The charge independent $\vec{E} \times \vec{B}$ drift that develops then advects particles to further propagate the pressure perturbation in the poloidal direction. In the adiabatic electron limit, these parallel moving electrons have no way to dissipate their momentum and the plasma potential instantaneously follows the density ($\tilde{n}/n \approx e\tilde{\phi}/kT_e$) leading to propagation of the wave without any growth. However, if for instance, the parallel electron motion can be slowed by interaction with the background plasma, a phase difference is introduced between the density and potential perturbations ($\tilde{n}/n \approx (1 - i\delta)e\tilde{\phi}/kT_e$). The displacement of this potential fluctuation and subsequently the direction of the $\vec{E} \times \vec{B}$ drift which develops can then, in addition to propagating the drift wave, lead to amplitude growth or damping (see Fig. 7).

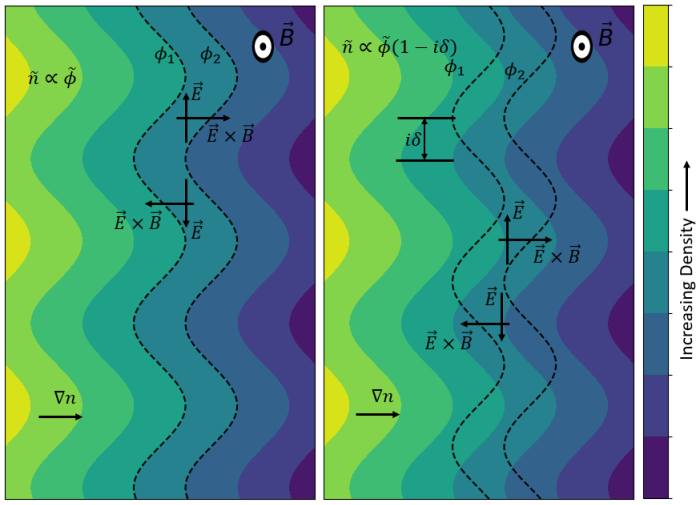


Figure 7: Heuristic picture of a drift wave mode. Here the magnetic field is shown out of the page. Shown in the left panel is a case with adiabatic electron response which leads to propagation of the drift wave at constant amplitude. On the right, a phase difference in the electron response is present due to interaction between parallel moving electrons and the background plasma. In this case, the phase difference leads to reinforcement of the original density perturbation.

For a particular mode, characterized by a fluctuation frequency $\omega$ and wavenumber $k$, an initial perturbation is characterized by a growth rate, $\gamma$. If $\gamma$ is negative, the mode reduces in magnitude over time and is said to be stable. In the case of a positive $\gamma$, the mode is unstable and the perturbation will grow in magnitude over time. In reality, plasma fluctuations are characterized by an entire spectrum of modes with different values of $k$, $\omega$, and $\gamma$ which can couple to one another exchanging energy. Eventually, as unstable modes increase in magnitude, the dissipation of energy via transfer into stable modes will outweigh the growth of the unstable modes. In this case, the mode is said to be "saturated" and the final balance of mode amplitudes is what sets the level of transport seen at the macroscopic scale. It should also be noted that in addition to coupling to stable modes, instabilities can be stabilized by large flows that can shear apart turbulent eddies [35], or by coupling to modes at very small spatial scales which lead to viscous dissipation.

The first of the relevant drift wave modes, TEMs [36], occur when the regions with a large number of trapped electrons line up with regions of bad curvature (convex with respect to the pressure gradient). In this situation, the bounce averaged drift velocity of the trapped electrons aligns with the drift wave direction and can feed energy into the instability. These modes will become unstable in the same regime one expects $1/\nu$ neoclassical transport, that is when $\nu_e^* < 1$ and trapped electrons can complete more than one orbit [37]. Parameters which are closely tied with anomalous transport due to TEMs are strong electron density or temperature gradients, low collisionality, as well as $\epsilon_h$ which describes the trapped particle fraction.

In addition, ITG modes tend to dominate in situations where the density is flat and the pressure gradient is due almost entirely to the ion temperature gradient. In this case, energy transfer can occur between the drift wave and ion acoustic waves [38]. One common metric which is tied to the instability of ITGs is the gradient length ratio which, above a certain critical value (which is unique to the particular experimental setup), is an indicator of unstable growth of ITGs. The gradient length ratio is defined as [37]:

$$\eta = \left(\frac{L_n}{L_{T_i}}\right) = \frac{4L_n}{3R}\left(1 + \frac{T_i}{T_e}\right)(1 + k_y^2\rho_i^2) \tag{24}$$

Here, $L_n = -n/\nabla n$ and $L_{T_i} = -T_i/\nabla T_i$ are the gradient lengths for the density and ion temperature respectively.

Finally, ETG modes are characterized by electron scale fluctuations with radially elongated streamers [39] and are, as the name suggests, driven unstable by sufficiently large electron temperature gradients. While ETGs tend to cause relatively negligible particle transport, they can contribute significantly to the overall heat transport via the electron channel [40]. Since the aim of this thesis is to characterize impurity

particle transport, little attention is given to ETG driven instabilities.

Due to the stabilization of TEM turbulence over a range of conditions [41], W7-X is fairly unique in terms of stellarators in the fact that it exhibits a "Valley of stability" in temperature and density gradient space. In this region, both TEM and ITG turbulence is reduced and transport becomes again dominated by neoclassical processes [42]. This stability region becomes even more pronounced in certain W7-X configurations such as high iota (see section 3.2) and reduced turbulence scenarios have recently been demonstrated experimentally [43]. A 2D mapping of growth rates for the most unstable modes is shown in Fig. 8 for two configurations as a function of the temperature and density gradient lengths.

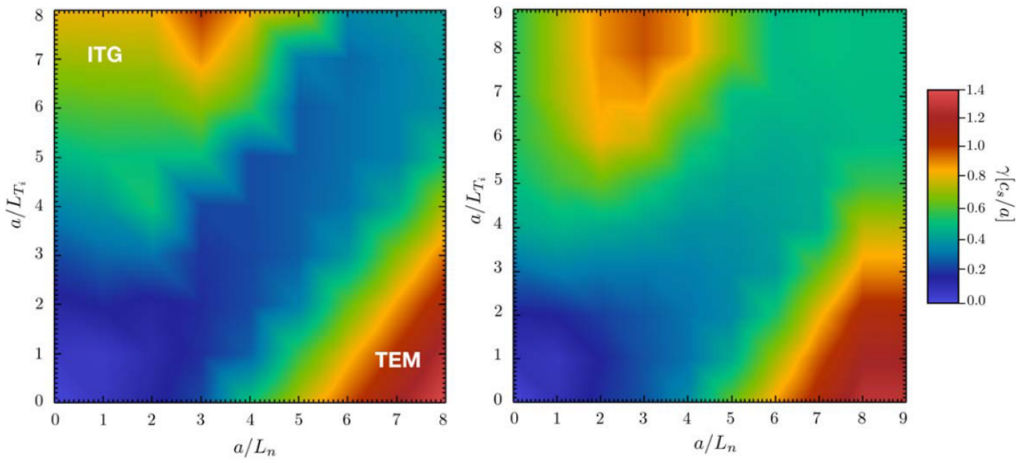


Figure 8: Growth rates of the most unstable modes as a function of the temperature and density gradient lengths. Shown on the left is the stability map for the high iota W7-X configuration and on the right is that for the standard W7-X configuration. The upper left region corresponds to parameter space where ITG turbulence is expected to dominate while in the bottom right, TEM turbulence dominates. Figure credit: [42]

One of the most common ways in which turbulent transport is modeled in magnetized plasmas is through the use of gyrokinetic simulations. Commonly used for stellarator experiments is the GENE code which computes Larmor radius scale turbu-

lent fluctuations by solving a simplified version of the Fokker Planck equation which can be derived by taking an average over the gyro-orbits [44]. The Fokker Planck equation can be written as:

$$\frac{dF_s}{dt} = \frac{\partial F_s}{\partial t} + \vec{v} \cdot \nabla F_s + \frac{Z_s e}{m_s} \left( \tilde{\vec{E}} + \frac{\vec{v}}{c} \times \tilde{\vec{B}} \right) \cdot \frac{\partial F_s}{\partial \vec{v}} = C\left[F_s\right] + S_s \tag{25}$$

Here, $F_s = F_s(\vec{x}, \vec{v})$ is the particle distribution function for species $s$, $Z_s$ and $m_s$ are the species charge and mass respectively, $\vec{v}$ is the particle velocity, $\tilde{\vec{E}}$ and $\tilde{\vec{B}}$ are the electric and magnetic fields with both the background and fluctuating quantity, $C\left[f_s\right]$ is the Landau collision operator, and $S_s$ is an additional source term. The process of gyro-motion averaging is not described here but is given in detail in reference[44].

Doing such an averaging changes the problem from considering charged particles with six degrees of freedom, that is three spatial coordinates and three velocity values, to that of considering rings of charge streaming along field lines. Therefore, the distribution function now has five degrees of freedom: three spatial coordinates, a parallel velocity, and a magnetic moment (i.e. $F_s = F_s(\vec{x}, v_\parallel, \mu)$). In this case, the governing equation for the distribution function of charged rings can be written as:

$$\begin{aligned} &\frac{\partial F_s}{\partial t} + \left( v_\parallel \vec{b_0} + \frac{B_0}{B^*_{0\parallel}} (\vec{v}_{E\times B} + \vec{v}_{\nabla B_0} + \vec{v}_c) \right) \\ &\quad \cdot \left( \vec{\nabla} F_s + \frac{1}{m_s v_\parallel} \left( q_s \vec{\bar{E}}_1 - \mu \vec{\nabla} (B_0 + \bar{B}_{1\parallel}) \right) \frac{\partial F_s}{\partial v_\parallel} \right) = \langle C_s(F) \rangle. \end{aligned} \tag{26}$$

Again, here $F_s$ is the distribution function for the rings of charge for a given species, $s$, $\vec{b_0}$ is the unit vector aligned with the background magnetic field and $B^*_{0\parallel} = \vec{b}_0 \cdot (\vec{\nabla} \times (\vec{A}_0 + \frac{m_s c}{q_s} v_\parallel \vec{b}_0))$ with $\vec{A}_0$ being the background magnetic vector potential. $\vec{v}_{E\times B}$, $\vec{v}_{\nabla B_0}$, and $\vec{v}_c$ are the $E \times B$, $\nabla B$ and curvature drifts respectively, $\vec{\bar{E}}_1$ and $\bar{B}_{1\parallel}$

are the perturbed electric field and parallel magnetic field where the bar notation indicates a gyro-average, and $\langle C_s(F)\rangle$ is the gyro-averaged collision operator.

The strategy used to reduce computational expense is then to consider the splitting of the distribution function $F_s$ into a background component $F_{0s}$ and a perturbation $f_{0s}$. $F_s = F_{0s} + f_{0s}$ is then substituted into equation 26. A natural ordering arises during this step where the background distribution function is of order one while the perturbed distribution is of order $\epsilon = \rho_{ref}/L_{ref}$, or rather the ratio of the Larmor radius to the characteristic length scale. Terms can be collected based on their ordering in $\epsilon$ and after a suitable choice for the background distribution function $F_{0s}$, expansion of vector products, and normalization of all parameters such that they become dimensionless, the perturbed distribution function can finally be summarized as:

$$\frac{\partial g}{\partial t} = \mathcal{Z} + \mathcal{L}[g] + \mathcal{N}[g] \tag{27}$$

where, $g$ represents the combined distribution function for a given species, $\mathcal{Z}$ is a constant term that depends only on the background distribution, $\mathcal{L}$ is the linear term that scales with $\epsilon$, and $\mathcal{N}$ is a nonlinear term that scales with $\epsilon^2$. The nonlinear term arises from the definition of $\vec{v}_{E\times B}$ which is the only one of the three considered drifts that depends strongly on the perturbed fields (see [45]). The full forms of $\mathcal{Z}$, $\mathcal{L}$ are lengthy and not discussed here, one can find them in [45]. One can represent the nonlinear term as such:

$$\mathcal{N}[g] = \sum_{\vec{k}'_\perp} (k'_x k_y - k_x k'_y)\chi(\vec{k}'_\perp) g_s(\vec{k}_\perp - \vec{k}'_\perp). \tag{28}$$

Here, the nonlinearity has been transformed from $\vec{x}$ space to $\vec{k}$ space. $k_x$ and $k_y$ are the radial and binormal wavenumbers and $\vec{k}_\perp = k_x\hat{x} + k_y\hat{y}$. $\chi$ is the potential like

function described for species $s$ as $\chi_s = \bar{\phi} - \frac{1}{c} v_\parallel \bar{A}_{1\parallel} + \frac{1}{q_s} \mu \bar{B}_{1\parallel}$. In this context, $k$ and $k'$ represent two adjacent components of the wavenumber spectrum. Equation 28 implies then that the nonlinearity introduces interaction between fluctuations with differing wavenumbers, enabling the mechanism described above for nonlinear coupling of mode energies.

In simulations, one can choose to solve the linear problem by neglecting the operator, $\mathcal{N}$. This assumption greatly reduces computational demand and can be used to calculate the linear growth rates of various spatial modes. This strategy can be useful in determining likely candidates for turbulent modes which may be dominating heat and particle transport. As mentioned previously, in real turbulent situations, unstable modes will eventually cascade their energy into stable modes or to length scales which experience viscous dissipation. This is an inherently nonlinear process and if one wishes to retrieve an estimate for the magnitude of the resultant heat and particle fluxes, the nonlinear problem must be solved. Additionally, it has been shown that in some scenarios, the magnitudes of calculated linear growth rates may not qualitatively describe the full nonlinear heat fluxes [46].

Gyrokinetic simulations can be used to estimate turbulent impurity fluxes at W7-X. In fact, this has been done using the STELLA code for the standard magnetic configuration [47] at the $\sqrt{s} = \sqrt{\Phi/\Phi_{LCFS}} = 0.49$ flux surface. Results from this study are shown in Fig. 9 where pure ITG and pure TEM conditions are considered. Here, $a/L_{T_i} = 4$ in the case of ITG and $a/L_{n_e} = 4$ in the case of TEM where all other gradients are set to zero. To isolate the contributions from the diffusion, thermo-diffusion, and convection coefficients, the non-linear simulations are run multiple times with either the impurity temperature or density gradients set to zero. This allows one to define transport coefficients to use in the impurity heat and particle flux equations analogous to those in equation 19. It was found that for both ITGs and

TEMs a negative thermodiffusion coefficient ($D_{12}$ in equation 19) is present while the $D_{11}$ diffusion coefficient is predicted to be stronger for the ITG case. Additionally, there is a convective term that is not related to the temperature and density gradients which is positive in the case of ITG and negative in the case of TEM. In the end, the measured convection velocity then would be a combination of the thermodiffusion and convection term (all terms not multiplied by the density gradient in equation 19). Note that in order to experimentally resolve these differences, a precision of $\sim 1$ m/s and $\sim 1$ m$^2$/s would be necessary. Moreover, under steady state conditions ($\Gamma = 0$), equation 21 can be rearranged to the form $v/D = \nabla n/n$. Therefore, the density gradient (and therefore the degree of density peaking) will be directly tied to the ratio $v/D$.

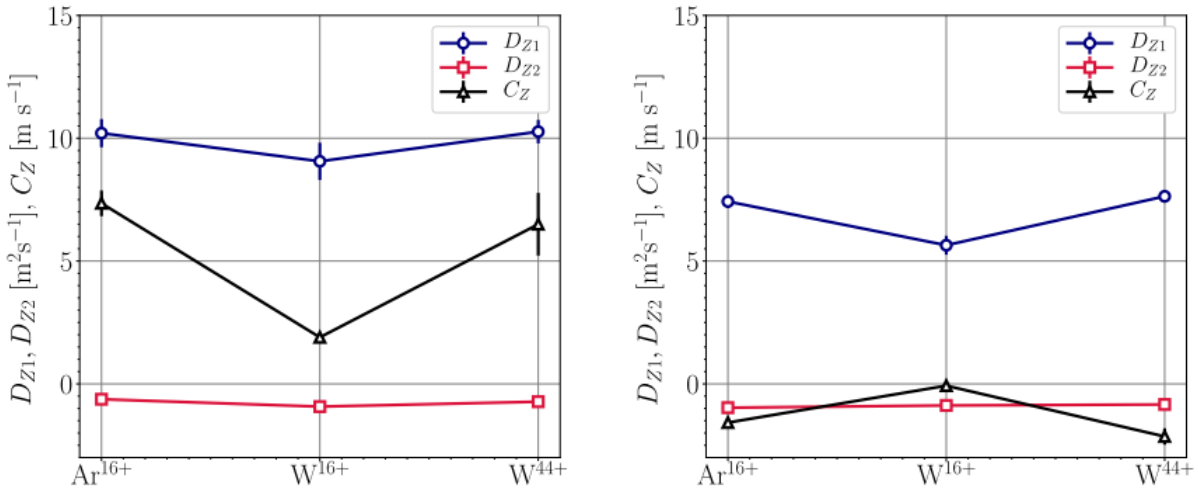


Figure 9: Nonlinear gyrokinetic results from the STELLA code for three different impurities in pure ITG (left) and TEM (right) conditions. Densities of $n_e = 10^{19}$ m$^{-3}$ and temperatures of $T_i = T_Z = 1$ keV. Normal diffusion is shown in blue with open circles, thermodiffusion in red with open squares, and convection in the absence of gradients is shown in black with open triangles. Figure credit: [47]

Finally, previous experiments have been conducted to study the turbulent transport of impurity ions in real W7-X plasmas. Results indicate that neoclassical dif-

fusion and convection are much too small to explain observed impurity decay times [23]. Additionally, follow-up studies investigated the effect of the ion-electron temperature ratio which affects the stability of ITG turbulence through equation 24. It was observed that for increased ion to electron temperature ratios, the decay times of impurities increased, suggesting reduced transport due to partially suppressed ITG turbulence [24]. These studies provided strong evidence for impurity transport dominated by turbulence however, since the analysis utilized line-integrated measurements of impurity radiation, uncertainties in the impurity density profile shapes made it difficult to determine the impurity convection velocities. In order to thoroughly compare experimental results to gyrokinetic simulations and to characterize the impurity peaking characteristics, the capability to measure the convection velocity is developed in this thesis.

# 3 Experimental Setup

## 3.1 Description of the W7X Stellarator

W7X is the largest stellarator experiment to date with a major radius of 5.5 m and a minor radius of $\sim$ 53 cm. Superconducting coils are utilized to generate a $\sim$ 2.5 T on-axis magnetic field necessary for confinement. W7X is an example of an quasi-omnigeneous configuration stellarator. The onmigeneity condition implies that the mean guiding center magnetic drift has zero radial components such that in the case of no collisions, ions and electrons are confined to flux surfaces. This was accomplished by designing the magnetic geometry to be quasi-isodynamic, a subset of the omigeneity condition where trapped particles precess poloidally [48]. It was later discovered that this design choice not only led to reduced neoclassical transport and bootstrap current, but also led to the alignment of particle trapping regions with good curvature causing stabilization of TEM turbulence [41].

The design criteria for W7-X were chosen to meet the initial goals for the experiment [49]: **1.** Achieve steady state operation at reactor relevant temperatures and densities. **2.** Achieve stable plasma equilibria with $\langle\beta\rangle = 5\%$. **3.** Sufficiently long plasma confinement to allow for extrapolation to reactor parameters. **4.** Having the ability to sufficiently control the density and impurity content. **5.** Operate a magnetic field in steady state using superconducting coils. As of now, W7-X has achieved plasmas in steady-state operation with core temperatures of $\sim$ 5 keV, densities of $\sim 10^{20}$ m$^{-3}$ and normalized plasma betas around 1-2%.

## 3.2 Magnetic configurations in W7-X

W7-X is designed with a magnet system consisting of 50 non-planar and 20 planar superconducting coils arranged with five fold symmetry around the torus (see Fig. 10). The modular coil design of W7-X allows for adjustments in the individual coil currents in order to affect the 3D geometry of the magnetic field in fusion experiments. Doing so allows for exploration of regimes with different transport mechanisms and degrees of optimization.

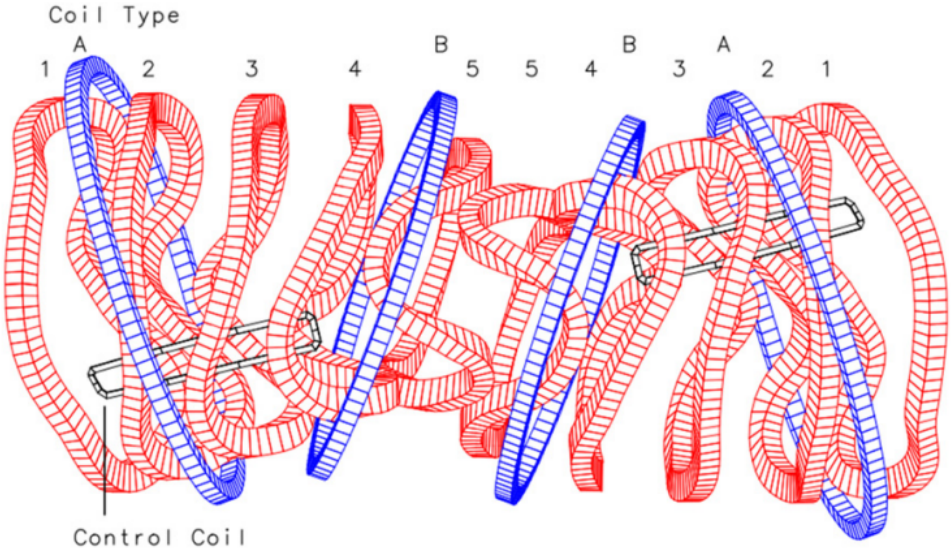


Figure 10: Coil orientations for one of the five W7-X Modules. Planar coils are shown in blue while non-planar coils are shown in red. Figure credit: [50]

The magnetic field structure of W7-X can be described using a Fourier decomposition:

$$|\vec{B}| = B_0(r)\left[\sum_{m,n=0} \epsilon_{m,n}(r) cos(m\theta - nN_p\xi)\right]. \tag{29}$$

Here, $\xi$ and $\theta$ are toroidal and poloidal like coordinates defined for the so-called Boozer Coordinate system [51], $\epsilon_{m,n}$ is the relative strength of the various Fourier modes, and $N_p$ is the total number of symmetric field periods in the toroidal direction. The $m = 0$,

$n = 1$ component is referred to as the mirror term and is commonly scaled up and down in various W7-X experiments leading to the so-called “high mirror” and “low mirror” configurations. Additionally, in this document, the ”high iota” configuration is referenced. For this case, coil currents have been adjusted to increase the rotational transform by $\sim 25\%$ at the edge relative to the standard W7-X configuration [50]. Profiles of the rotational transforms for these configurations are shown in figure 11.

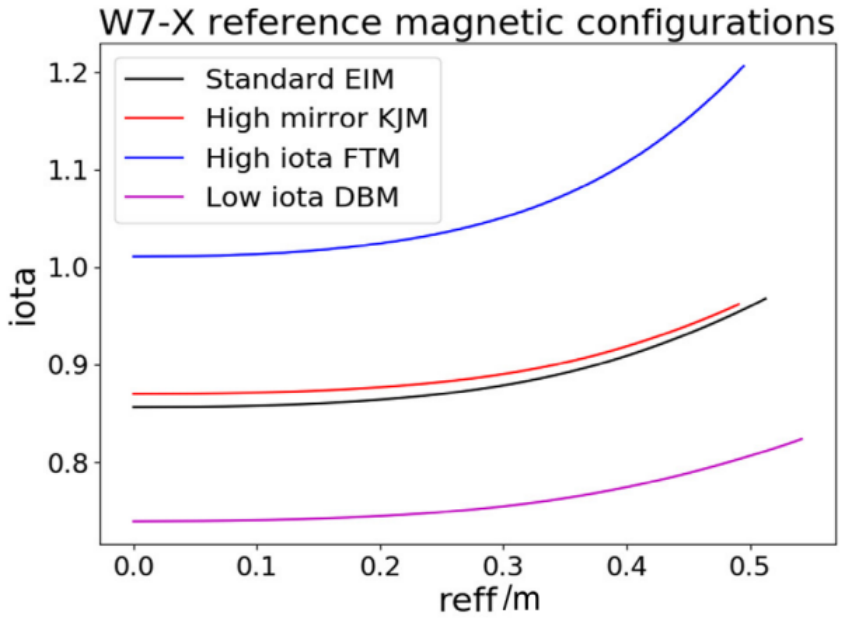


Figure 11: Rotational transforms of various magnetic configurations at W7-X as a function of effective minor radius (in meters) Figure credit: [52]

## 3.3 The Scrape Off Layer and the Island Divertor

Toroidally nested flux surfaces are not guaranteed in general. In stellarators and tokamaks, outside a certain radial position, the magnetic field topology transitions from closed surfaces to open field lines which eventually intersect the first wall. The domain outside of the last closed flux surface (LCFS) is referred to as the scrape off layer (SOL). Charged particles in the SOL will stream along the field lines and will

hit plasma facing components.

In most stellarator and tokamak scenarios, the heat and particle fluxes in the SOL are directed towards wall components known as divertors. These are put in locations far away from the plasma and are typically made of materials which are capable of withstanding extremely high heat loads, at least for the duration of the plasma discharge. Inevitably, the bombardment of the divertor surface will lead to physical sputtering of material which can migrate back into the confined region. These surfaces therefore act as one of the main sources of impurities expected in reactor relevant scenarios.

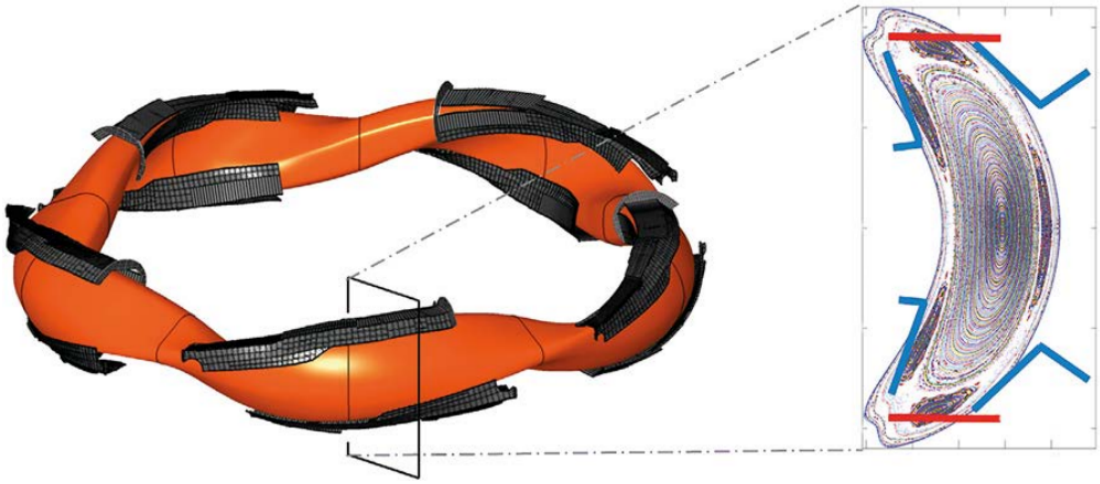

Figure 12: Depiction of the island divertor setup at W7-X. The 10 divertor modules interface with the $\iota = 5/5$ island chain. One can see the overlap between the island divertor and the magnetic islands in the Poincare plot shown on the right figures adapted from: [53]

Within the SOL, so-called magnetic islands can form when the rotational transform, $\iota = n/m$ locally reaches a rational value. In the W7-X "island" divertor, the rotational transform has been curated such that the $\iota = 5/5$ rational surface is in the edge region. The resulting island chain intersects divertor tiles positioned on 10 modules dispersed around the torus to allow for efficient heat and particle exhaust.

A depiction of the $\iota = 5/5$ island chain along with its intersection with the divertor tiles is given in figure 12

## 3.4 Auxiliary Heating

### 3.4.1 Electron Cyclotron Resonance Heating

Electron cyclotron resonance heating (ECRH) is a method for heating magnetized plasmas in which injected microwave radiation resonates with the cyclotron frequency of the electrons. The injection frequency is typically chosen to interface with a resonance layer of constant field strength that passes through the magnetic axis of the device. Note that ECRH radiation is not able to penetrate through overly dense plasmas with densities larger than the cutoff densities. For the 2nd harmonic O-mode and X-mode heating used at W7-X, these densities are approximately $1.2 \times 10^{20}$ $m^{-3}$ and $0.8 \times 10^{20}$ $m^{-3}$ respectively. Here O-mode and X-mode refer to two possible solutions for the cold plasma dispersion relation and are waves which are polarized parallel and perpendicular to the magnetic field respectively. The ECRH heating occurs at a frequency of 140 GHz and is rated for 1 MW of heating power per gyrotron. However in reality, typically only 700 kW of power is delivered to the plasma resulting in a total maximum heating power of 7 MW (2nd harmonic resonance at 2.5 T) [54].

ECRH is the main heating method used at W7-X. Microwaves are generated by the ten gyrotrons and directed via several mirrors to ECRH launchers. This beam path is depicted for one module of W7-X in figure 13. These launchers couple radiation at the lab side of the beam path (at atmosphere) to the vacuum vessel and allow for steering of the beams in the vertical and toroidal direction. Aiming the ECRH beam away from the magnetic axis via the launchers allows for off axis heating experiments. Additionally, toroidal current can be induced by launching microwaves in the toroidal

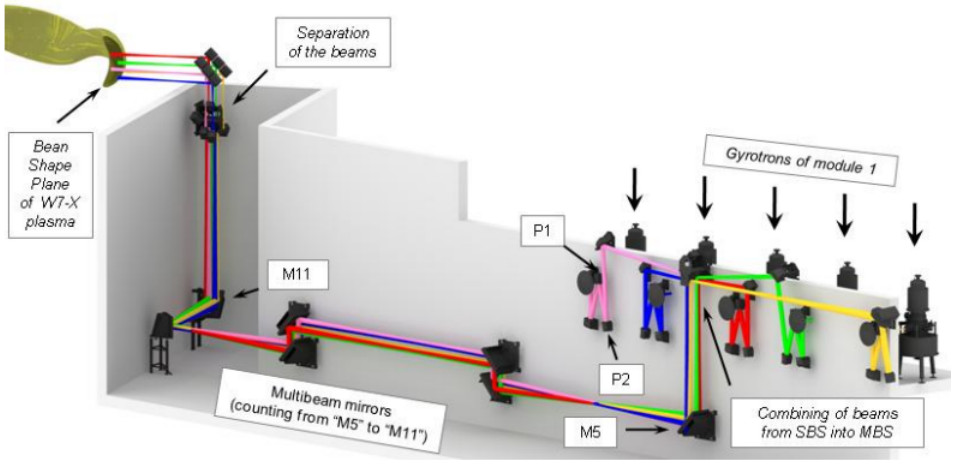


Figure 13: Transmission line setup of the ECRH beams in W7-X. Figure Credit: [55]

direction. This allows for the local modification of the rotational transform profile.

### 3.4.2 Neutral Beam Injection

Neutral beam injection (NBI) at W7-X, in contrast to ECRH, can provide heating of both plasma ions and electrons. Additionally it serves as a source of fast ions enabling studies of their confinement properties [56, 57]. Such studies are necessary to evaluate confinement characteristics of fusion born alphas in reactor scale operations. Specifically, W7-X is equipped with two NBI boxes containing four sources each. However, for the work presented in this thesis only two beam sources are considered mainly for diagnostic purposes. These sources are numbered 7 and 8, of which source 8 is oriented more tangential to the magnetic axis [58]. A depiction of the NBI box is given in Fig. 14.

Both available sources are characterized by an extracted ion current of 90 A made up of a mix of $H_1^+$, $H_2^+$, and $H_3^+$ ions with relative particle fractions of $\sim 31\%$, $\sim 42\%$, and $\sim 27\%$ respectively (as of OP 2.1). These ions are accelerated by a voltage of 55 kV and are subsequently neutralized via electron capture. Due to their masses, the

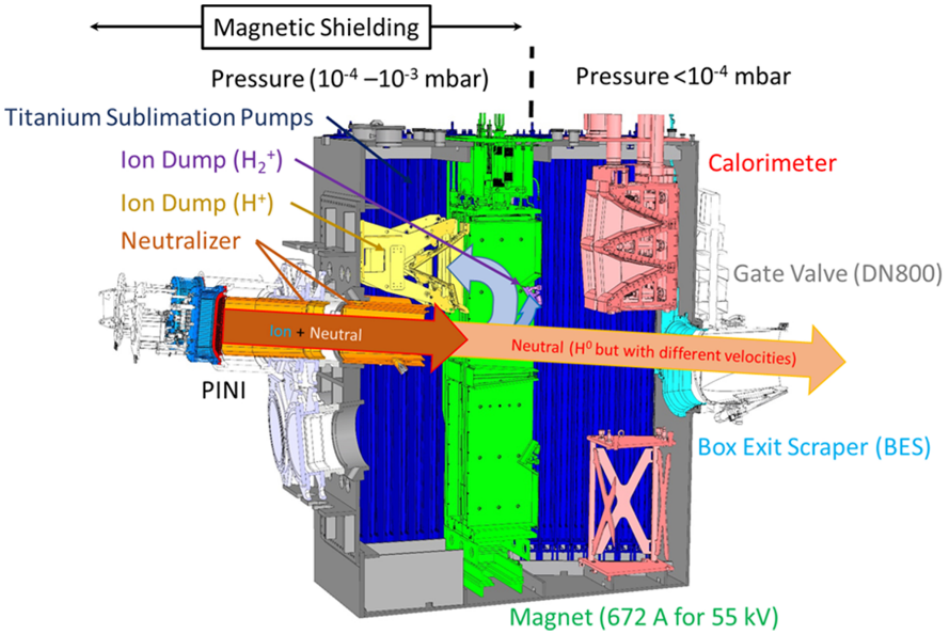


Figure 14: Illustration of the main components of the neutral beam injection system. Figure credit: [58]

ions experience different accelerations and are subsequently said to be the full, half, and third energy components of the beam for $H_1^+$, $H_2^+$, and $H_3^+$ respectively. The total estimated coupled power from NBI with both beams on is $\sim 3.4$ MW.

In addition to providing heating capabilities and a source of fast ions, the NBI system also acts as a source of donor neutrals for charge exchange reactions. Due to the high neutral density compared to the background plasma, radiation following charge exchange events is localized to the vicinity of the beam. When a diagnostic line of sight intersects the neutral beam, spatially localized measurements of, for instance, impurity radiation can be obtained[59].

## 3.5 Diagnostic Capabilities

W7X is equipped with over 100 diagnostics of which, the most relevant for this thesis are described here. First, Thomson scattering is introduced which provides spatially

resolved temperature and density measurements. Next, the laser blow off (LBO) system for controlled impurity injection is introduced. Finally, several diagnostics which measure radiation originating from impurities are discussed. These include a soft X-ray/VUV sensitive spectrometer known as HEXOS, a metal foil bolometer system, and a charge exchange spectroscopy diagnostic known as the ITER like spectrometer (ILS).

### 3.5.1 Thomson Scattering

Thomson scattering is a process in which a photon is scattered off of a charged particle in the plasma. This occurs when an ion or electron is accelerated by the electric field of an incoming light wave, and emits electromagnetic dipole radiation. In Thomson scattering applications, the source of these incident light waves is a high powered laser which allows for localization of the measured scattered light. For a measured Thomson scattering spectrum, the absolute intensity is used to determine the electron density while the spectral shape gives information on the electron temperature.

At W7-X, up to five Nd:YAG lasers (1064 nm) are utilized as the laser source where each can operate at a repetition rate of 10 Hz. These lasers are designed to be able to fire simultaneously for high intensity or staggered to increase the time resolution of the measurement [60]. Scattered light is observed using two separate sets of collection optics, each with several lines o f sight to provide profile information. The two optical ports provide profile information on either the inboard or outboard sides of the plasma. The numerical aperture for the fibers on both optics is designed to be 0.37 with focal lengths of 172 mm and an image de-magnification between 7 and 11 [60]. The light collected by the fiber bundles is then directed to a set of polychromators which analyze the spectral characteristics. Additionally, the entire Thomson scattering system is structurally isolated from the vacuum vessel and cryostat for

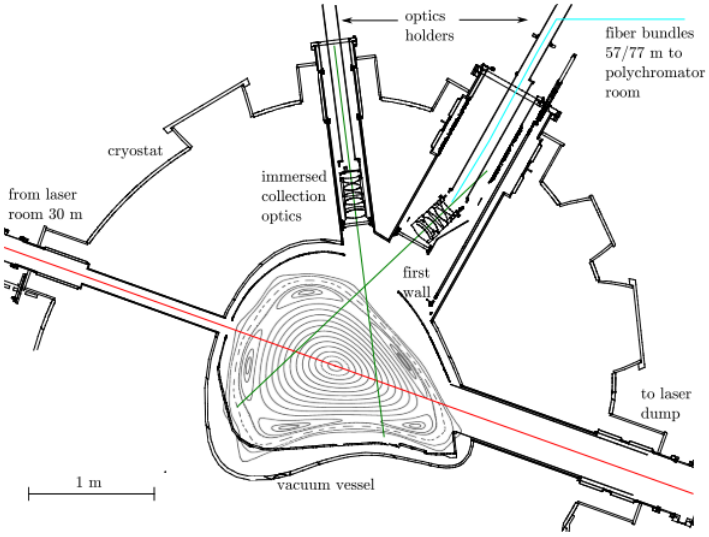


Figure 15: Description of the Thomson scattering setup for W7-X. The laser light path is shown in red and the collected scattered light is shown in green. Figure credit: [60]

optical stability purposes. A depiction of the laser and optical setup is given in Fig. 15

### 3.5.2 Laser Blow Off for Impurity Injection

W7X is equipped with a laser blow off (LBO) impurity injection system for dedicated impurity transport studies [61, 62]. The LBO system consists of a high powered Nd:YAG laser, optical components for directing the beam, and a glass target mount which is movable via a manipulator arm. A schematic of the LBO system installed at W7-X is given in Fig. 16.

When an impurity injection is required, the Nd:YAG laser fires a 1 J, 6 ns long pulse along the optical path towards the glass slide. By controlling the position of a diverging lens, the beam can be resized between 0.1 and 4 mm in diameter allowing for variation in the number of injected particles. A piezo motor can be used to control a movable mirror which deflects the beam towards the coated slides.

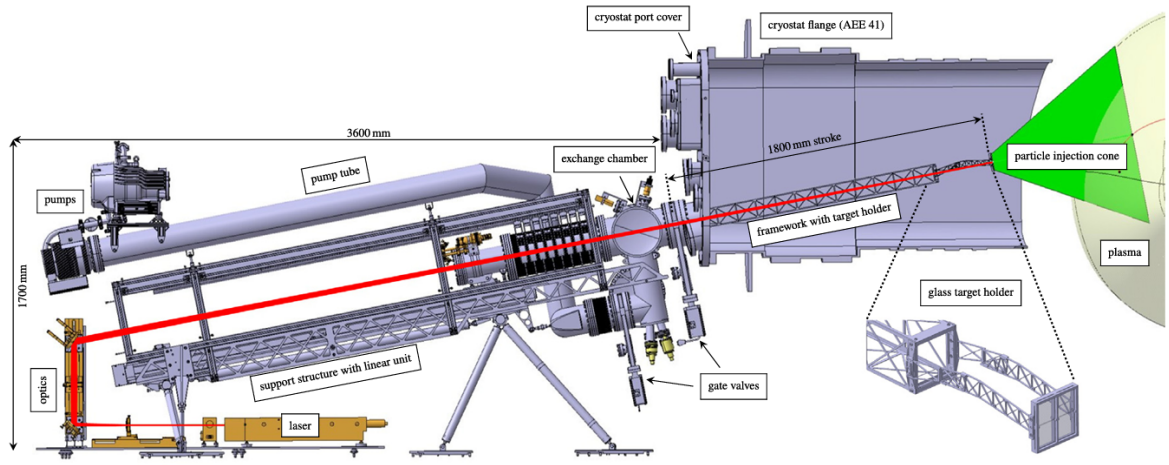


Figure 16: Schematic of the LBO system at W7-X. The laser path is depicted as a red line which falls on a glass target holder capable of holding four different LBO targets. The laser position on the targets can be adjusted via the moveable mirror. Figure credit: [62]

This can be done quickly enough to allow for each pulse to hit a fresh, non-ablated, region of the glass slide even when using a 20 Hz repetition rate. Finally, the beam illuminates glass slides which are coated in a 2 to 5 μm thick coating of impurity material. After the beam strikes the back side of the sample slides, the coating is ablated and thermal expansion drives the cloud of impurities towards the plasma. A cartoon depiction of this process is given in Fig. 17. It is important to note that when LBO is used to inject impurities into a stellarator, only neutral atoms and unionized clusters can reach the confinement region since ionized impurities will stream along field lines in the SOL into the divertor. For the work described in this document, LBO of Iron impurities injected into W7-X plasmas is considered. The kinetic energy of these injected impurities is approximately 20 eV inferred based on fast camera time of flight measurements [3] and a total of $\sim 2 \times 10^{18}$ neutral particles are injected into the edge. These ablated species then traverse one of the $\iota = 5/5$ islands before reaching the LCFS. The subsequent radiation from these impurities is

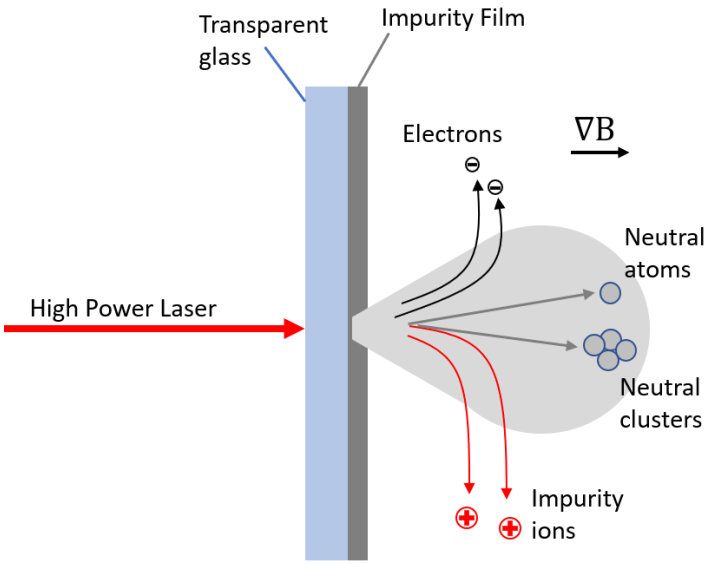


Figure 17: Illustration of the laser ablation injection of an impurity.

then observed using various spectrometers including the HEXOS and CXRS system. Note that the introduction of impurities carries with it the possibility of impacting the overall power balance in the plasma and can temporarily change the background temperatures and densities. In general, LBO studies are designed to inject only a small amount of particles such that this change is small, however it is important to monitor the plasma to observe any possible changes. Such changes in the temperature can potentially have an effect on the underlying transport mechanisms by for example altering the strength of the thermodiffusion term in equation 20 or the temperature ratio in equation 24. Additionally, significant impurity content can lead to radiative collapse and is seen to occur in experiments when the total radiated power exceeds $\sim 40\%$ of the total injected power [15].

### 3.5.3 HEXOS

The High Efficiency Extreme Ultraviolet Overview Spectroscopy system (HEXOS) is available for detecting vacuum ultraviolet (VUV) and soft x-ray (SXR) radiation

coming from highly ionized impurities in the core region [63]. This system is designed to provide a broadband measurement of emissions along a single line of sight. With a wavelength range of 2.5 nm to 160 nm, it can operate at a frame rate of 1 kHz. The large wavelength range is obtained using four separate SPRED style [64] spectrometers with some wavelength overlap. The detectors used in this system consist of a multichannel plate (MCP) detector that converts the VUV/x-ray light to the visible spectrum where it is then amplified and collected by a photodiode array. Light incident from an entrance slit is directed onto holographic diffraction gratings on toroidal substrates. The diffracted light is then measured in a flat field setup allowing for focused imaging of a wide spectral range. A depiction of the line of sight setup is given in Fig. 18. Since these measurements are line integrated, they are generally not spatially localized. Additionally, during the OP 2.1 campaign, for which we perform our analysis, a spectral radiance calibration was unavailable such that only the time dynamics of the observed line emissions can be analyzed.

### 3.5.4 Metal Foil Bolometer System

A bolometry system is available which measures the total radiated power along a variety of lines of sight [65]. The detectors for this system consist of a 5 μm thick gold absorbing layer which sits atop a ceramic substrate. To improve the absorption of visible wavelength radiation ($> 400$ nm), a 50 nm thick carbon layer is sputtered on top of the gold which reduces the visible light reflectivity by more than a factor of 5 [65, 66]. The absorber and substrate sit atop a Pt sensor that is one leg of a Wheatstone bridge. The measured resistance along the sensor can then be used to determine its temperature and therefore, the total absorbed radiation. The radiated

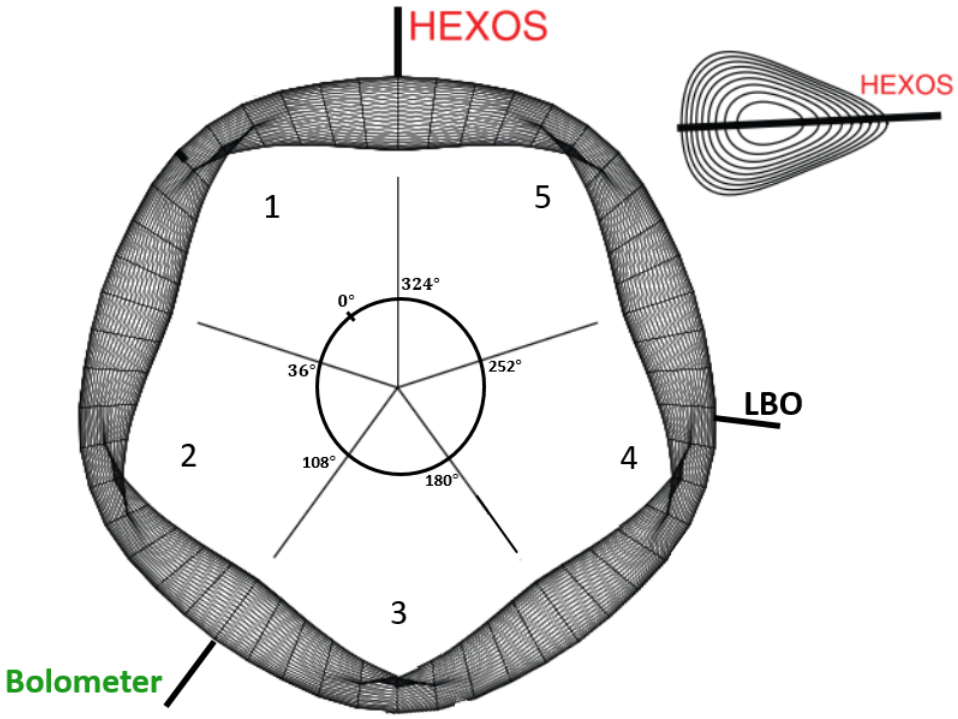


Figure 18: Depicted is of the line of sight geometry for the HEXOS system as well as the location with respect to the LBO injection [23].

power incident on the detector can be determined using the following equation:

$$P = \frac{1}{f_t \times S}\left[\tau \frac{du_d}{dt} + f_c \times u_d\right]. \tag{30}$$

Here, $f_t$ is the optical transmission factor of the microwave shielding, $S$ is the detector sensitivity in amperes, $\tau$ is the cooling time constant ($\sim 0.1$ s). $u_d$ is the voltage signal measured by the Wheatstone bridge, and $f_c$ is a correction factor due to resistance in the 40 m long cables that read out the signal. The value of these paremeters can be determined via a routine calibration using an *in situ* heating process [67].

The lines of sight are grouped such that they are measured by two detector arrays named the horizontal bolometer camera (HBC) and the vertical bolometer camera

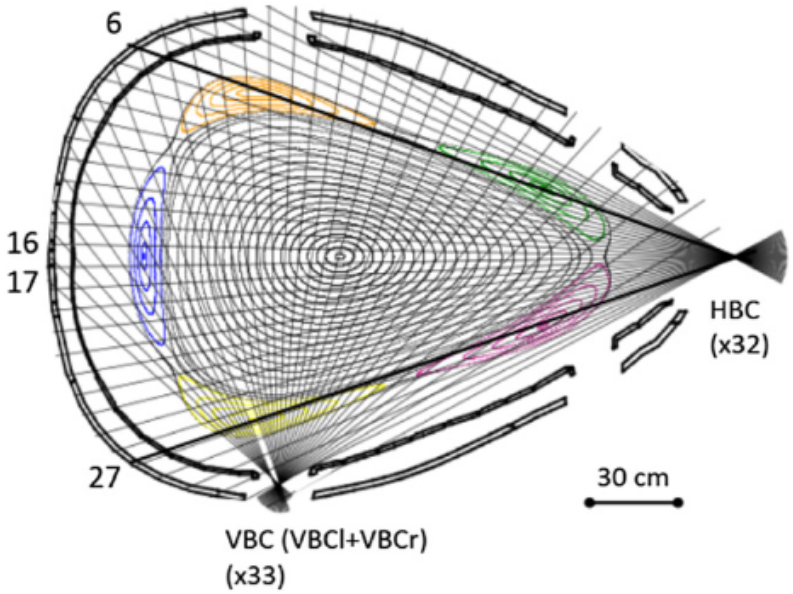


Figure 19: Distribution of the lines of sight used in the tomographic inversion which measures the 2D radiated power distribution. Figure credit: [65]

(VBC) with 32 and 48 total channels respectively. These arrays illuminate each detector via a pinhole style camera aperture and define the line of sight distribution. Using a tomographic inversion algorithm, the 2D radiation distribution can be determined by considering radiation along all of the HBC lines of sight and 33 of the VBC lines of sight. These sight-lines are depicted in figure 19.

### 3.5.5 ITER-Like Spectrometer (ILS)

Charge exchange recombination spectroscopy (CXRS) is utilized to measure impurity radiation from a specific location. In this case, the CX radiation of interest originates from the charge exchange between an ion species of interest and the neutral beam. The main CXRS spectrometer is referred to as the ITER like spectrometer (ILS) as it was originally designed as a prototype system which will be used for the ITER fusion project [68]. The system is designed to simultaneously measure helium, beam

emission from the heating neutral beam (BES), and impurity radiation, each of which lie in distinct wavelength ranges. To enable this feature, the incident light is split into three different beam paths via achromatic mirrors (the so-called Red, Green, and Blue signals). The red, green, and blue channels observe wavelength ranges of 648-666 nm, 518-534 nm, and 461 - 474 nm designed to view BES, impurity radiation, and Helium II light respectively. The ray tracing depiction of this setup is given in Fig. 20.

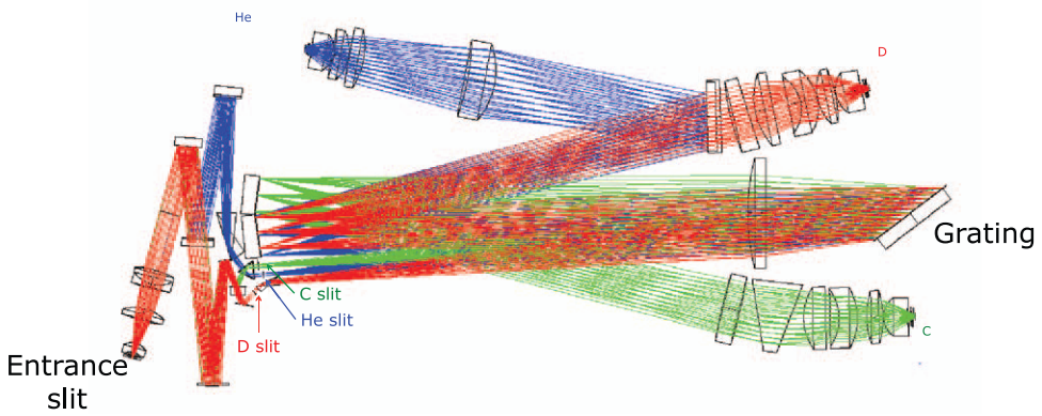


Figure 20: Ray tracing depiction of the light splitting in the ILS spectrometer. The helium, carbon, and hydrogen channels are shown as blue, green, and red lines respectively. Figure credit: [68]

For use with the ILS, several lines of sight are available which view neutral beam lines 7 and 8 via collection optics located at three different ports. The first two of these collection optics, labeled as "A" and "M" respectively view along the toroidal direction and 45° off the toroidal direction for detection of poloidal flow [68]. Both the A and M optical systems additionally feature two line of sight arrays perpendicular to the main line of sight arrays. These allow for measurement of the neutral beam width and divergence. The final observation port designated with a T, provides additional measurements with reduced spatial resolution. Figure 21 shows the line of sight setup with respect to the two NBI sources designated as "S7" and "S8" (also referred to as

"Q7" and "Q8" in other locations in this document).

One of the main purposes of the ILS system is to provide spatially localized measurements of the intrinsic carbon temperature. Since impurities are typically highly collisional with the main ion species, it is then assumed that the carbon temperature is representative of the main ion temperature. In order to determine the carbon ion temperature, line radiation from the CVI emission line at 529 nm is measured following charge exchange with the neutral beam. These lines are then Doppler broadened by a factor that is proportional to $\sqrt{T_i}$. However, such measurements can be complicated by the presence of passive radiation that originates from the edge region where background neutrals exist. This edge emission will contribute to the total measured signal and must be accounted for in order to determine reliable localized temperature values. Correction for the passive signal can be accomplished by either allowing for the additional fitting of a secondary passive emission line or by injecting short beam "blips" where the emission before and after the injection can be subtracted from the signal.

Additionally, the ILS system has been used to determine carbon impurity density profiles by analyzing the intensity of the CVI emission [59]. This method has proven to be useful for measurement of steady state impurity density profiles; however, its temporal resolution of $\sim$ 60 Hz prevents it from being used to measure transient impurity behavior following LBO. Specifically, for turbulent transport measurements on W7-X, a time resolution of $\sim$ 1 kHz is necessary to resolve the rise and fall times of the impurity emissions [23, 69].

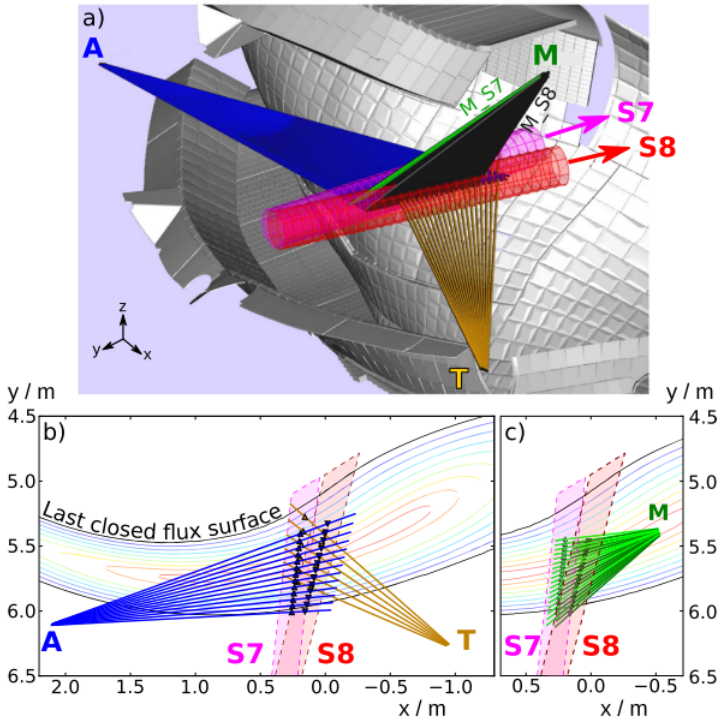


Figure 21: Graphical depiction of the available lines of sight for the ILS spectrometer at W7-X. Two NBI sources are available for viewing and are labeled as "S7" and "S8" here. Collection optics are located at the three ports labeled as A, T, and M. Figure credit: [68]

# 4 Development of a High Speed Charge Exchange Spectroscopy Diagnostic at W7-X

## 4.1 Line of Sight Setup

For the OP2.1 experimental campaign at W7-X, a new charge exchange diagnostic has been installed that views both neutral beam source 7 and 8 using the optics at the M port, which is shared with the ILS system (see figure 21). 18 new 600 µm diameter optical fibers have been installed at the existing optical head and allow for measurement along neutral beams 7 and 8. A photo of the optical head arrangement prior to the inclusion of the new lines of sight is given in figure 22 and the placement

of the new fibers is shown in figure 23.

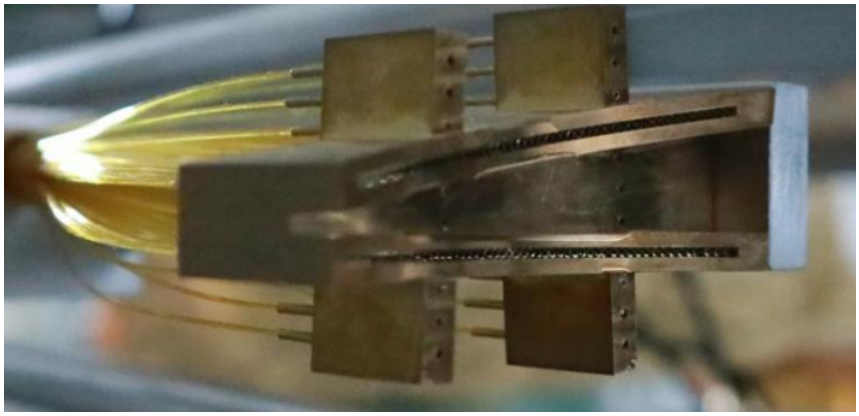

Figure 22: A photo depicting the optical head used at the M-port which collects radiation from NBI sources 7 and 8.

Additionally, for the analysis presented here, one preexisting 400 μm fiber is included which views near the mid-radius on the inboard side (labeled LOS #10 in figure 24). The approximate locations where the lines of sight intersect NBI 7 are shown projected on a poloidal cross-section of the W7-X magnetic field in figure 24a. Here the beam density is simulated using the Monte-Carlo code pyFIDASIM [3] which will be described in section 6.2.2. In this simulation, the total hydrogen beam density is a sum of the contributions from the full, half, and third beam components, as well as thermal ions that have been neutralized via charge exchange with the beam or other thermal neutrals (known as the "halo" component). Considered in the pyFIDASIM calculation is the ground state, n=1, up to the n=6 excited state. Kinetic profiles used in the calculation are given in a later section in figure 49. The beam attenuation along the direction of the major radius for each energy component and the first two energy levels is given in figure 24b. To determine the spatial resolution of the diagnostic, beam neutrals predicted by pyFIDASIM along a given line of sight are binned according to their location on a predefined 1D radial grid. The curves are then normalized such that their maximum is 1 for easy comparison. These so-called

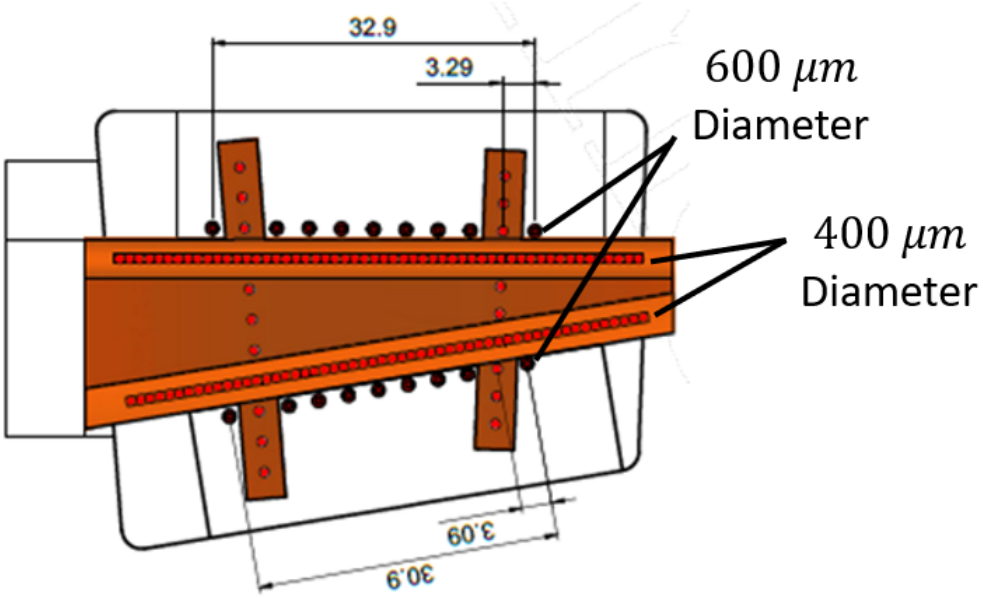


Figure 23: Illustration of the M-port optical head showing the pre-existing 400 μm fibers and the new 600 μm fibers.

localization functions, $\Gamma(r/a)$, are shown in figure 25 and indicate good spatial resolution ($\sim 1.5-4.5$ cm) for the outer lines of sight while there is a notable degradation in the radial localization for the most inboard three lines of sight (resolution $> 8.5$ cm).

## 4.2 Spectrometer Design

The five new spectrometers have been designed to allow for high speed measurements of charge exchange radiation originating from injected iron impurities [1]. A top down view of one of the spectrometers is given in Fig. 26. The cost has been minimized through the use of off-the-shelf components and custom 3D printed optical component holders. In traditional spectrometer setups, a knife-edge entrance slit is used to cut off the light at the entrance to the system and guarantee good line-shape however, this approach only allows a fraction of the total collected light into the spectrometer.

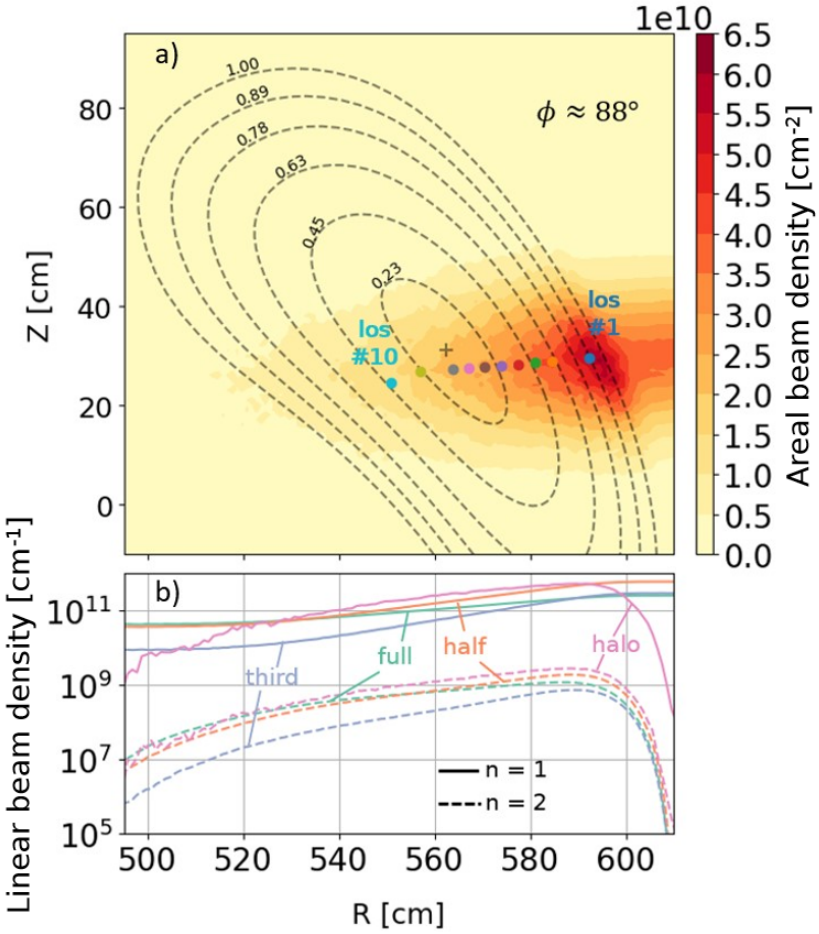


Figure 24: a) Approximate locations of intersection between ten of the new CXRS diagnostic lines of sight and the 50 keV neutral beam. Shown in color-scale is the beam density integrated over the toroidal direction. b) Attenuation of the various beam components for energy levels n = 1 and n = 2. Plotted densities are integrated over both the toroidal and Z directions.

In the new system, round to linear fiber bundles (600 $\mu$m fiber bundle diameter at the round end) are utilized in place of a conventional slit in order to retain any light that would typically be lost at the entrance. This fiber bundle consists of 30 individual 100 $\mu$m fibers, each with a cladding thickness of 12.5 $\mu$m and a numerical aperture of 0.22. At the round end, the cladding is removed and the individual fibers are fused together to minimize packing losses. At the linear end of the bundle, this translates to a slit height of 3.75 mm which is coupled directly to a Nikkor lens (180 mm focal

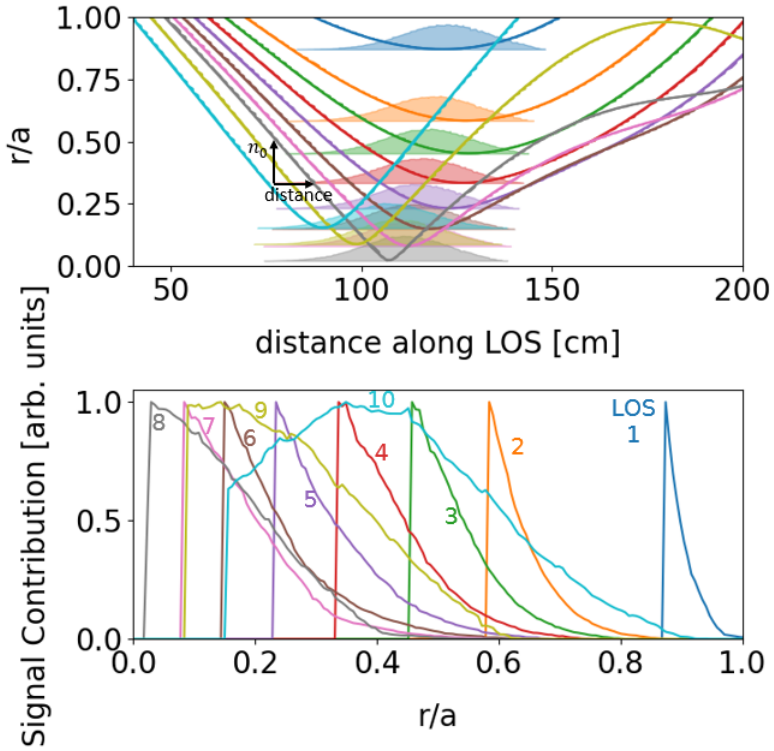


Figure 25: **Top:** Radial position as a function of distance along the selected lines of sight. Additionally, the local beam density (which is directly proportional to the CX intensity) is depicted as a function of distance along the LOS. **Bottom:** Radial localization of charge exchange signals coming from the selected lines of sight.

length, f/2.8). This connection is made via a custom 3D printed fiber holder that fastens to a Nikkor F-mount to C-mount adapter. The input light is then collimated and projected onto two co-planar 50 mm (2400 lines/mm) gratings. Here, the two 50 mm off the shelf gratings are chosen to reduce costs associated with a custom grating size. The two gratings are secured to a Standa high precision rotational stage ($\sim$ 0.23 arcsecond per step) via adjustable grating holders and another custom 3D printed height block. The grating holders provide 3-axis adjustment of the grating orientation via micrometer screws such that the two gratings can be made coplanar and perpendicular to the optical plane. The diffracted light is then directed to an output Nikkor lens (135 mm focal length, f/2) arranged at an opening angle of 27

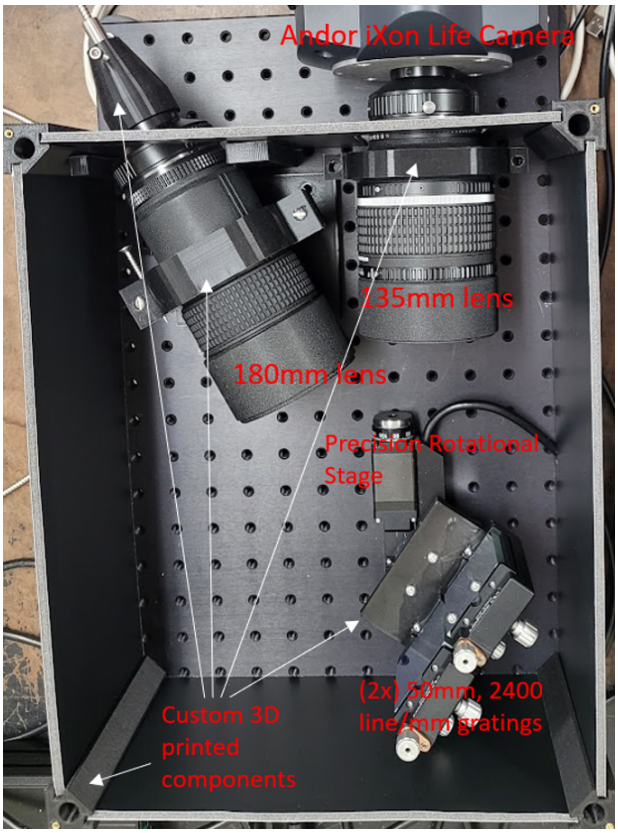


Figure 26: Top down view of Assembled Czerny-Turner spectrometer.

degrees. The chosen opening angle is enforced by two form fitting 3D printed lens holders. Finally, the light fed into the output lens falls onto an ultra-low readout noise EM-CCD camera. Specifically here, we utilize the Andor iXon Life 897 CCD camera which is characterized by an array of 512x512 16$\mu$m pixels. Given the chosen lenses, the image that arrives at the detector is de-magnified by a factor of (135 mm /180 mm) = 0.75 such that the image height at the detector is $\sim$ 2.81 mm.

The geometry of the spectrometers has been designed such that two fiber bundles can stack vertically allowing for dual channel readout of ten lines of sight. By using two channels per spectrometer, the Gaussian instrument function width (i.e. the minimum observable line width) for individual channels can be slightly broadened due to the imaged fiber bundles appearing tilted on the CCD chip. This is an imaging

effect due to the vertical angle of the light incident on the spectrometer gratings (also known as the parabola effect) and can be partially corrected by rotating the fiber bundles by a few degrees leading to a slight horizontal offset between the two channels. Despite this feature, the Gaussian instrumental function widths on each channel are between 0.06 nm and 0.13 nm (see figure 29) which is sufficient to resolve all peaks of interest in this work. The Andor EMCCD camera operates in a frame-transfer mode where three regions of interest (ROI) are defined and their collected light vertically binned. Two of these ROIs are used for imaging the two stacked fiber bundles while the third (middle) ROI is used for CCD smearing effect detection and correction (see Fig. 27). The smearing effect is described in more detail in section 4.4

Finally, an absolute spectral radiance calibration has been performed for the new CXRS system via the use of an in-vessel calibration sphere. This allows for the comparison of spectral radiance, and therefore localized impurity densities between CXRS channels. Later on in the analysis, this calibration allows for the detailed comparison of relative intensities seen by the different lines of sight.

## 4.3 Grating alignment and wavelength calibration

To ensure that observed signals remain centered on the detector as the gratings are turned to observe different wavelength ranges, 3-axis adjustable grating holders are used to orient the gratings perpendicular with the optical plane. Since the vertical position of a given image depends on both the rotation of the grating about its normal vector as well as its "tilt" forwards and backwards (see Fig. 28), these two positions

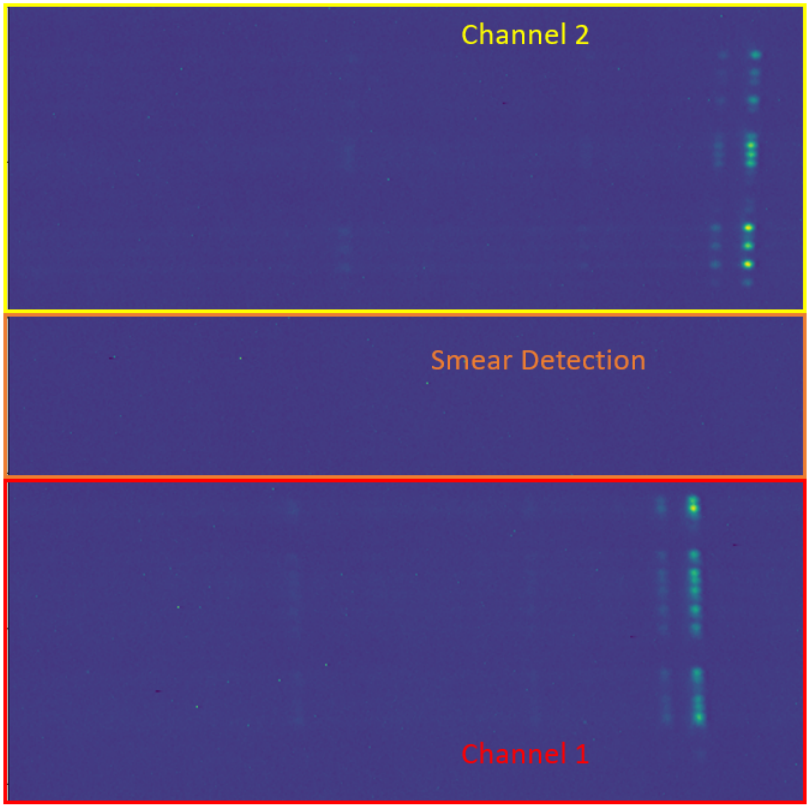


Figure 27: Region of interest allocation on one of the CCD detector areas. The two channels collect light from two different lines of sight with the central channel used to detect and correct smearing related features.

must be adjusted accordingly. This effect is described by the following equation:

$$Z = Z_0 + \phi_1 \sqrt{1 - \left(\frac{\lambda}{c}\right)^2} + \phi_2 \frac{\lambda}{c} \tag{31}$$

where,

$$c = 2cos\left(\frac{\theta}{2}\right) d. \tag{32}$$

Here, $Z$ is the total vertical displacement of the image on the detector (in pixels), $Z_0$ is the vertical displacement when the grating is perfectly aligned, $\phi_1$ and $\phi_2$ are the grating tilt and rotation (see figure 28), $\lambda$ is the wavelength of the observed line emission, $\theta$ is the spectrometer opening angle, and $d$ is the groove spacing.

To utilize this method, the spectrometer is illuminated with a calibration lamp and the vertical pixel positions of several calibration lines at various wavelengths are recorded for different grating positions set by the rotational stage. The forward model is then utilized in an optimization loop to infer the current grating orientation relative to the optical plane. With the unaligned orientation of the grating holder known, adjustments can be made via the micrometer screws to ensure alignment. Finally, once both gratings are aligned perpendicular to the optical plane, their horizontal angle can be adjusted such that the diffracted lines from each grating perfectly overlap.

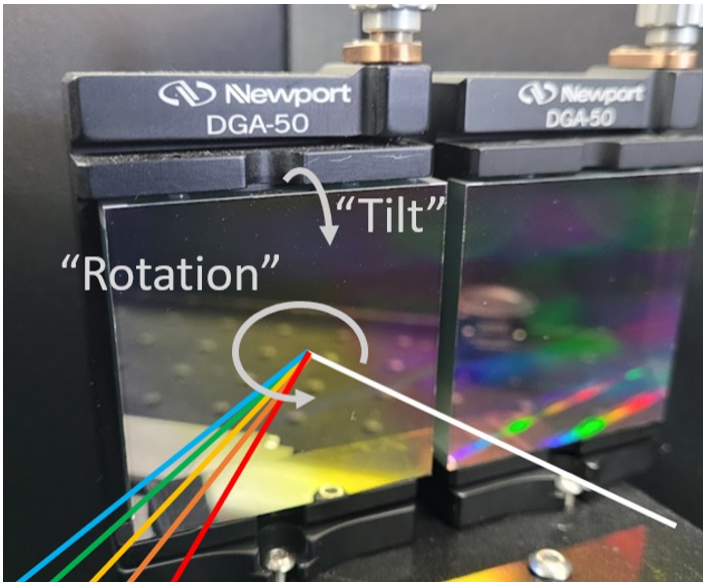


Figure 28: Degrees of freedom when aligning grating orientation. Both the "tilt" and "rotation" affect the vertical displacement of diffracted lines on the detector surface.

For wavelength calibration of the designed spectrometer a neon calibration lamp is utilized. A representative, vertically binned spectrum can be seen in Fig. 29. A synthetic spectrum is forward modeled based on the grating equation giving the expected wavelength along the chip at each pixel position. This is done by considering the grating equation:

$$d(sin\phi - sin\theta) = m\lambda \tag{33}$$

Here, the light is incident at an angle of $\theta$ with respect to the grating surface normal and are diffracted at an angle of $\phi$. The grating order is $m$ and $\lambda$ is the observed wavelength. Since differing wavelengths of light are diffracted at different angles, the final lens then images them to a different horizontal position on the detector.

With this model, one can perform the wavelength calibration by comparing collected spectra to those expected when considering the NIST database [70, 71]. Here, we consider intense neon lines in the range of 530 nm - 545 nm of which there are four. In this calibration, the relevant geometric parameters for the spectrometer are inferred by using a least squares algorithm. These inferred parameters include the spectrometer opening angle and the grating angle (the two of which can be used to determine $\phi$ and $\theta$ in equation 33) as well as the final lens focal length. This determines the wavelength as a function of horizontal position along the detector. The individual lines are then fit to a super Gaussian function of the form:

$$f(x) = A \exp\left(-\left(\frac{\lambda - \lambda_0)^2}{2\sigma^2}\right)^P\right) \tag{34}$$

Here, the free parameters are $A$, $\sigma$, and $P$ which represent the line intensity, width, and super-Gaussian order respectively. Therefore, there is a total of six free parameters in the wavelength calibration routine.

As can be seen in Fig. 29 the spectral fit indicates excellent line shapes and well characterized relative intensities and wavelengths.

## 4.4 Smearing Effect and Correction Procedure

The employed EMCCD camera operates in the frame-transfer mode during which the whole image acquired is shifted to a covered region which is of similar size. In this region, the image is read out line by line by the register. Since the vertical shifting

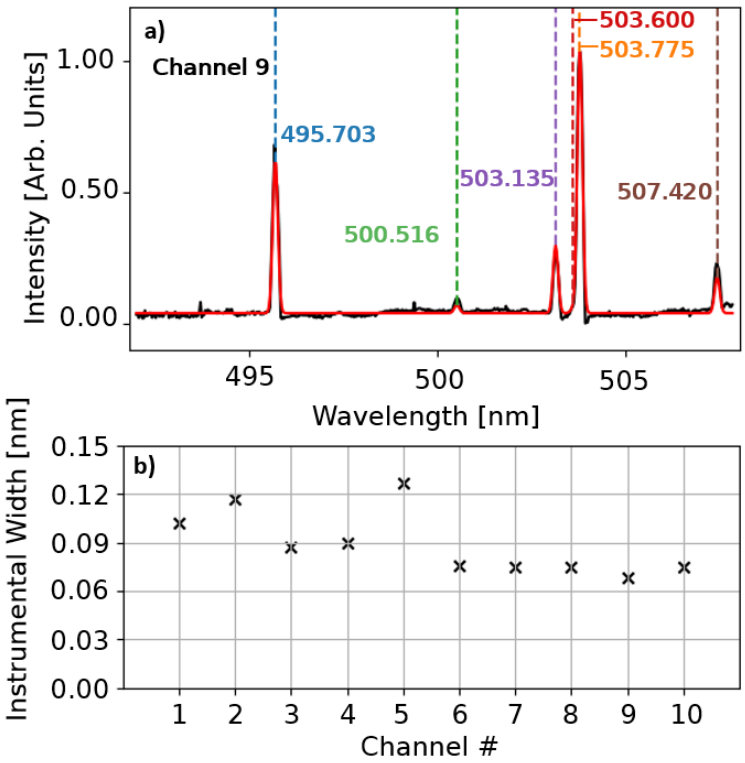


Figure 29: a) Recorded (black) and fitted (red) spectra from a neon calibration lamp for one representative spectrometer channel. b) The width of the fitted Gaussian instrument function for each spectrometer channel.

speed takes $\sim$ µs per row, photons are continuously collected during this process. For slower frame-rates, the time it takes to read out a signal is negligible compared to the exposure time. However, when the frame rate starts to become comparable to the readout time, the extra photo-electrons collected during the readout period can cause an effect known as smearing. For the dual channel spectrometers described here, this causes a certain fraction of the radiation from either fiber bundle to appear on the opposite channel. By comparing features that appear both on the central smear detection channel and one of the signal channels, the smear contribution per vertical pixel can be determined and subtracted. An example of the application of this procedure for one spectrum collected following LBO of iron is given in figure 30

which is collected at a frame rate of 1 kHz with a vertical shift speed of 1.7µs. Here, we can approximate the smear contribution channel A has present in channel B by subtracting a scaled down version of channel A from channel B. The scaling factor can be determined by comparing the channel A with the central "smear channel". The most intense peak is identified on channel A and is normalized by the number of vertically binned pixels in that ROI. Then the effect that peak has on the remainder of the CCD is determined by comparing with its observed intensity on the smear channel divided by the number of vertically binned pixels in the smear channel.

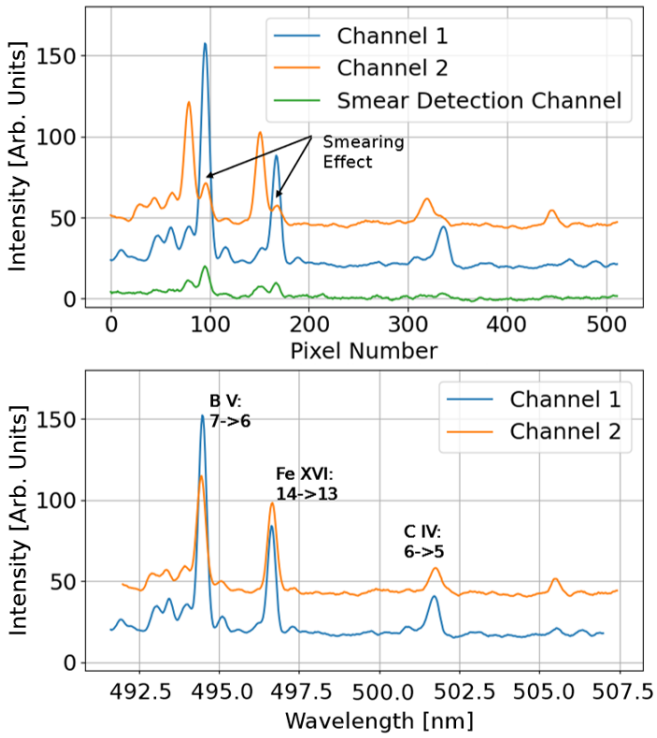


Figure 30: Top: Example spectrum of two channels on a single spectrometer in which smearing effects are observed when operating at 1 kHz. Bottom: Smear corrected spectra plotted vs. wavelength. The data shown is taken from a snapshot of an iron LBO injection.

For example, if one were to evaluate the smear correction on channel 1 (labeled $I_1$) due to channel 2 (labeled $I_2$) and considering the smear channel (labeled $I_{sm}$), the

smear correction would be:

$$I_{1,corrected} = I_1 - n_{px,1}\left(\frac{I_{sm}\left(x_{max}\right)}{n_{px,sm}}\right)\frac{n_{px,2}}{I_2\left(x_{max}\right)}I_2 \tag{35}$$

Here, $I_{sm}\left(x_{max}\right)$ and $I_2\left(x_{max}\right)$ indicate the measured intensity of the smear channel and channel 2 at the pixel location where $I_2$ is at its maximum. A more succinct description is that the *per pixel* effect of the signal from channel 2 is evaluated and multiplied by the number of pixels channel 1 contains. This contribution is then subtracted from the recorded spectrum seen by channel 1. An example of the smear correction performed on a raw spectrum following LBO injection of iron is given in figure 30. As can be seen, the smear effect is up to 10% of the total signal and can be corrected.

# 5 Measurement of High-n Rydberg Emissions

One of the main results of this thesis work is the exploration and successful use of high-n Rydberg emissions for impurity studies. In the following sections, this method is explored. First, a theoretical description is given of the high-n Rydberg emissions along with the benefits of the diagnostic concept. Next, the collected data is presented and briefly discussed.

## 5.1 Theoretical Description

Line emissions originate from electronic transitions of bound electrons. Due to their quantum nature, the angular momentum of these electrons must be an integer multiple of the reduced Planck constant, $\hbar$. This gives rise to discrete energy levels which can be occupied by a finite number of electrons according to the valence shell model. To fully define an energy level for a specific atomic system, one must specify the electrons so-called quantum numbers. These include the principle quantum number $n$, the orbital angular momentum quantum number $\ell$, the magnetic quantum number $m_\ell$, and the spin quantum number $m_s$. In the absence of electric or magnetic fields, the energy of a bound electron is only determined by $n$ leading to the potential for degeneracy between several electrons in the same energy level. With the introduction of electric or magnetic fields however, these electrons can either increase or decrease their energy breaking, this degeneracy. This phenomena is known as the Stark effect and the Zeeman effect for the breaking of energy level degeneracy in electric and magnetic fields respectively.

Before an impurity-ion bound electron can transition to a lower energy level and emit line radiation, it first must be excited into that state. This can occur due to a variety of processes such as impact excitation, 3-body recombination, dielectric

recombination, radiative recombination, or charge exchange recombination. Typically however, the dominant excitation process is from impacts between the impurity ion and electrons. This process readily populates the first few excited states and can be modeled using collisional-radiative codes such as ADAS [16] or ColRadPy [72]. These models work by considering all of the populating and depopulating processes for each of the excited states of a particular ion species in a background plasma. This couples the various ionization stages and excited states to one another via the relevant collisional and radiative processes allowing one to determine the relative populations of each energy level. An example of the steady state energy level balance for an $Fe^{23+}$ ion population has been calculated using ColRadPy when considering only impact excitation and spontaneous emission. Here the excited state populations are calculated as a function of electron temperature and at an electron density of $1 \times 10^{13}$ $cm^{-3}$ and are depicted in figure 31. The expected emission intensity from an excited state can then be determined by multiplying its calculated number density by the so-called "Einstein-A" coefficient which can be determined by solving the Schrödinger equation.

When the electron relaxes down to a lower level, energy must be conserved by the emission of a photon. The wavelength of this photon is then inversely proportional to the energy of the transition:

$$E_1 - E_2 = \Delta E = \frac{hc}{\lambda}. \tag{36}$$

In the case of hydrogen-like atoms (that is atoms with a single electron) in the absence of electric or magnetic fields, the wavelength of these transitions can be predicted with the so-called Rydberg equation:

$$\frac{1}{\lambda} = RZ^2 \left( \frac{1}{n_1^2} - \frac{1}{n_2^2} \right). \tag{37}$$

Here $R$ is the Rydberg constant for the element, $Z$ is the charge of the nucleus, and $n_1$ and $n_2$ represent the lower and upper energy levels. While this formula provides accurate predictions of transition wavelengths for hydrogen-like elements, it is generally a poor predictor of wavelengths for elements with multiple electrons. This is because the charge seen by an excited electron due to the nucleus is screened by inner shell electrons. This screening is imperfect and difficult to describe with a simple model. In these cases, the so-called "quantum defect" can be calculated and included as a correction factor in equation 37.

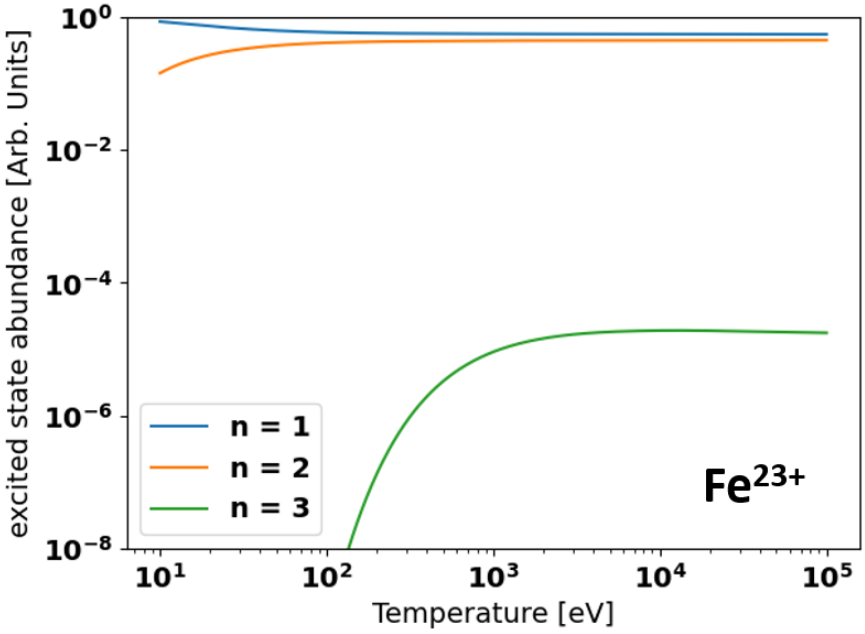


Figure 31: ColRadPy calculated fractional abundances of the first 3 energy levels of an $Fe^{23+}$ ion population in a background plasma with an electron density of $1 \times 10^{13}$ $cm^{-3}$.

Due to the complications that arise from the quantum defect, the Rydberg equation is typically applied and accurate for hydrogen or ions with only a single electron.

However, when one considers sufficiently excited states such that the bound electrons are far from the nucleus, the effective nuclear charge is seen as almost "point-like". Therefore, the Rydberg equation is once again a good approximation [73]. As energy levels of these so-called Rydberg states increase, they become closer and closer together and converge towards the ionization energy. For highly ionized, heavy elements (e.g. iron, tungsten, etc.), the ionization energies can be in the range of several keV which can start to be comparable to the rest mass of the electron, $\sim 511keV$. To more accurately describe the transition wavelengths of these systems, a relativistic correction to the Rydberg formula was recently derived [74, 75]:

$$\frac{1}{n_{air}\lambda_{air}} = \frac{m_e c}{h}\left(\frac{1}{\sqrt{1-(q+1)^2\alpha^2/n_2^2}} - \frac{1}{\sqrt{1-(q+1)^2\alpha^2/n_1^2}}\right) \tag{38}$$

Here $n_{air}$ is the index of refraction in air, $\lambda_{air}$ is the wavelength observed in air, $m_e$ is the mass of the electron, $c$ is the speed of light, $h$ is the Planck constant, $q$ is the net charge of the ion, and $\alpha$ is the fine structure constant.

The analysis of high-n transitions provides several benefits when compared to other spectroscopy methods. First, since the energy levels populated by the charge exchange process are so high [76] ( n $\gtrsim q^{3/4}$), they are excessively unlikely to be reached by electron impact excitation processes, the usual source of passive radiation inside the confined region. This is illustrated by figure 31, where one can see that only the first few energy levels are substantially populated by electron impact excitation. For this reason, as long as the background neutral density is sufficiently low, observed high-n Rydberg emissions are free of passive contributions, greatly simplifying their analysis. The second advantage of the high-n Rydberg method is that equation 1 only depends on the energy levels and the ion effective charge. Hence, the diagnostic method is agnostic to the particular impurity species and a single survey spectrometer

| $\lambda$ [nm] | q | $n_1$ | $\lambda$ [nm] | q | $n_1$ | $\lambda$ [nm] | q | $n_1$ | $\lambda$ [nm] | q | $n_1$ |
|---|---|---|---|---|---|---|---|---|---|---|---|
| 400.22 | 45 | 26 | 467.38 | 49 | 29 | 542.26 | 32 | 23 | 622.31 | 38 | 27 |
| 401.01 | 28 | 19 | 467.40 | 44 | 27 | 544.22 | 43 | 28 | 625.06 | 49 | 32 |
| 407.79 | 30 | 20 | 470.49 | 30 | 21 | 544.34 | 22 | 18 | 626.79 | 40 | 28 |
| 408.08 | 42 | 25 | 471.60 | 39 | 25 | 546.29 | 34 | 24 | 627.06 | 24 | 20 |
| 408.93 | 37 | 23 | 475.90 | 32 | 22 | 551.20 | 36 | 25 | 631.98 | 42 | 29 |
| 410.79 | 47 | 27 | 476.95 | 46 | 28 | 552.22 | 45 | 29 | 637.57 | 22 | 19 |
| 415.18 | 32 | 21 | 480.11 | 41 | 26 | 552.60 | 20 | 17 | 637.77 | 44 | 30 |
| 418.21 | 44 | 26 | 482.05 | 34 | 23 | 556.83 | 38 | 26 | 644.07 | 46 | 31 |
| 418.23 | 39 | 24 | 486.66 | 48 | 29 | 560.52 | 47 | 30 | 650.83 | 48 | 32 |
| 421.42 | 49 | 28 | 488.82 | 36 | 24 | 563.07 | 40 | 27 | 652.77 | 33 | 25 |
| 421.93 | 21 | 16 | 488.89 | 43 | 27 | 569.09 | 49 | 31 | 652.97 | 20 | 18 |
| 423.05 | 34 | 22 | 496.10 | 38 | 25 | 569.83 | 42 | 28 | 653.51 | 35 | 26 |
| 423.07 | 23 | 17 | 497.92 | 45 | 28 | 575.85 | 29 | 22 | 653.54 | 31 | 24 |
| 425.95 | 25 | 18 | 498.91 | 25 | 19 | 576.69 | 31 | 23 | 655.50 | 37 | 27 |
| 427.75 | 41 | 25 | 499.87 | 27 | 20 | 576.72 | 27 | 21 | 656.16 | 29 | 23 |
| 428.46 | 46 | 27 | 499.91 | 23 | 18 | 577.04 | 44 | 29 | 658.53 | 39 | 28 |
| 430.17 | 27 | 19 | 502.38 | 29 | 21 | 578.91 | 33 | 24 | 661.07 | 27 | 22 |
| 431.34 | 36 | 23 | 503.50 | 21 | 17 | 579.75 | 25 | 20 | 662.44 | 41 | 29 |
| 435.44 | 29 | 20 | 503.82 | 40 | 26 | 582.25 | 35 | 25 | 667.09 | 43 | 30 |
| 437.44 | 43 | 26 | 506.11 | 31 | 22 | 584.63 | 46 | 30 | 668.87 | 25 | 21 |
| 438.80 | 48 | 28 | 507.15 | 47 | 29 | 585.54 | 23 | 19 | 672.39 | 45 | 31 |
| 439.96 | 38 | 24 | 510.83 | 33 | 23 | 586.52 | 37 | 26 | 678.24 | 47 | 32 |
| 441.53 | 31 | 21 | 511.90 | 42 | 27 | 591.58 | 39 | 27 | 680.41 | 23 | 20 |
| 447.30 | 45 | 27 | 516.36 | 35 | 24 | 592.56 | 48 | 31 | 684.57 | 49 | 33 |
| 448.31 | 33 | 22 | 516.57 | 49 | 30 | 594.95 | 21 | 18 | 691.40 | 34 | 26 |
| 448.87 | 40 | 25 | 520.30 | 44 | 28 | 597.30 | 41 | 28 | 691.42 | 36 | 27 |
| 455.64 | 35 | 23 | 522.56 | 37 | 25 | 603.57 | 43 | 29 | 692.74 | 38 | 28 |
| 457.28 | 47 | 28 | 528.97 | 46 | 29 | 610.33 | 45 | 30 | 692.94 | 32 | 25 |
| 458.03 | 42 | 26 | 529.33 | 39 | 26 | 614.50 | 30 | 23 | 695.15 | 40 | 29 |
| 460.66 | 22 | 17 | 536.57 | 41 | 27 | 614.53 | 32 | 24 | 696.39 | 30 | 24 |
| 460.72 | 24 | 18 | 537.59 | 26 | 20 | 616.00 | 34 | 25 | 696.85 | 21 | 19 |
| 462.63 | 26 | 19 | 537.63 | 28 | 21 | 616.26 | 28 | 22 | 698.48 | 42 | 30 |
| 463.08 | 20 | 16 | 537.87 | 48 | 30 | 617.51 | 47 | 31 | | | |
| 463.43 | 37 | 24 | 539.29 | 30 | 22 | 618.66 | 36 | 26 | | | |
| 465.99 | 28 | 20 | 539.62 | 24 | 19 | 620.24 | 26 | 21 | | | |

Table 1: Line transitions with calculated wavelengths in the range of 492 nm - 508 nm. Wavelengths are calculated with equation 37.

can perform impurity injection studies for a variety of elements. The final benefit of this analysis method is that of the relative engineering simplicity of utilizing CXRS. Since observed emissions are in the visible range, standard lens and optical fiber setups can be utilized, something that is not possible when observing VUV or soft x-ray emissions. Therefore, high-n Rydberg spectroscopy is particularly powerful when performing impurity transport studies based on dedicated impurity injections.

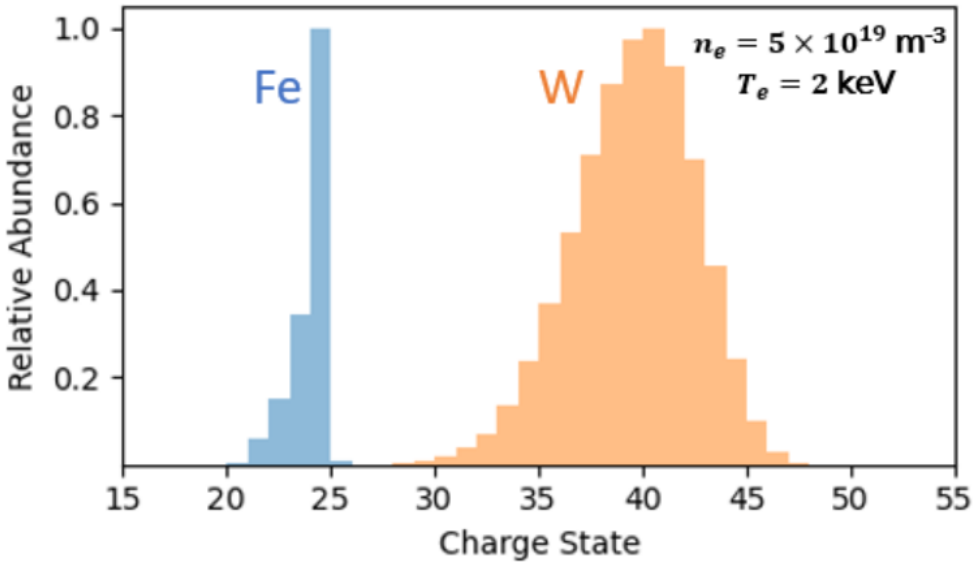


Figure 32: Histogram of the relative abundance of various charge states in a coronal equilibrium for a plasma with $n_e = 5 \times 10^{19}$ m-3 and $T_e = 2$ keV. ADAS files used for this calculation: *"acd89_fe.dat", "scd89_fe.dat", "acd01_w.dat", and "scd01_w.dat"*

While the experiments presented in this manuscript focus on high-n Rydberg emissions in the spectral range of 490 - 510 nm, equation 1 can be used to predict high-n transitions throughout the visible spectrum. In fact, iterating through possible values of $q$, $n_1$, and $n_2$, indicates the possibility of several hundred line transitions between 350 nm and 750 nm. Table 1 shows the expected wavelengths following all possible $\Delta n = 1$ transitions and charge states between Z=20 and Z=50. Whether these charge states are observable depends on the ionization balance of the impurity species being analyzed. For example, impurities such as iron have a limited number

of electrons so only charge states up to Z=26 exist. For very heavy impurities such as tungsten many charge states could potentially exist throughout the plasma volume and the charge balance strongly depends on the temperature range. Figure 32 shows a histogram describing the coronal charge state equilibrium of both iron and tungsten at a temperature of 2 keV and a density of $5 \times 10^{19}$ m$^{-3}$. As can be seen, Fe would primarily cause Z=23+ and Z=24+ radiation, while W would have a broader distribution centered around Z=40.

In addition, the strength of the various line emissions depends on whether the upper energy level for a particular transition will be likely to be populated following charge exchange. Typically, cross-sections for CX into particular energy levels peak 2-5 energy levels above the estimate of $n_{upper} \sim q^{3/4}$ [74]. The higher the beam energy, the more slowly these cross-sections fall off as one goes towards higher n therefore allowing for appreciable population of even higher energy levels [76]. For a fairly standard NBI injection energy of 50 - 100 keV, energy levels for which visible wavelength transitions occur are readily populated.

## 5.2 CXRS Experimental Data

Figure 33 shows representative data recorded by channel 4 on the new CXRS system for discharge #20230314.26. In this figure, the top panel shows the observed wavelength on the x-axis, the time on the y-axis, and the measured signal intensity in the color scale. The time at which the LBO injection occurs is depicted by the horizontal red dashed line. Here one can identify three lines originating from the high-n transitions originating from Fe XV, Fe XXII, and Fe XXIV. Several additional active and passive lines can be seen which are present due to the intrinsic carbon and boron content.

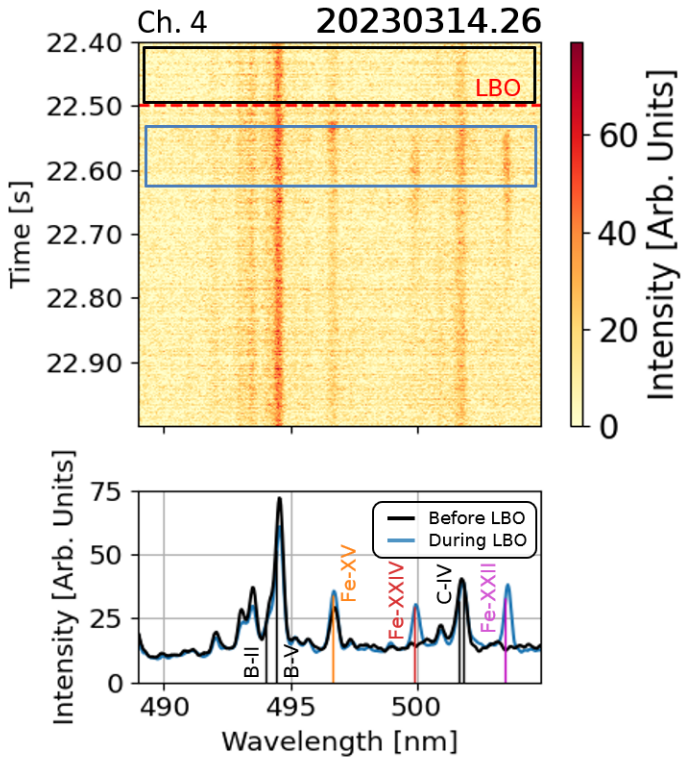


Figure 33: CXRS data originating from the WISC spectrometers (channel 4) for discharge 20230314.26 where iron is injected into a plasma with continuous NBI heating. The top plot shows the intensity in the color scale versus time and wavelength. The time at which the impurity injection is indicated by a dashed red line. The bottom plot shows the averaged spectra over the time windows depicted by the boxes in the top plot.

To illustrate that the line identification via equation 38 is agnostic to the particular impurity species considered, data from experiment #20230315.30 is given in figure 34. In this discharge, the tracer-encapsulated solid pellet (TESPEL) injection system is utilized which allows for deposition of impurity species directly into the core of W7-X [77]. Although tungsten injections were performed during this experiment, only short NBI "blips" were used to measure the main ion temperature. Here, the W XXIV is seen in the same location as the Fe XXIV lines with the addition of several new lines coming from charge states that do not exist for iron.

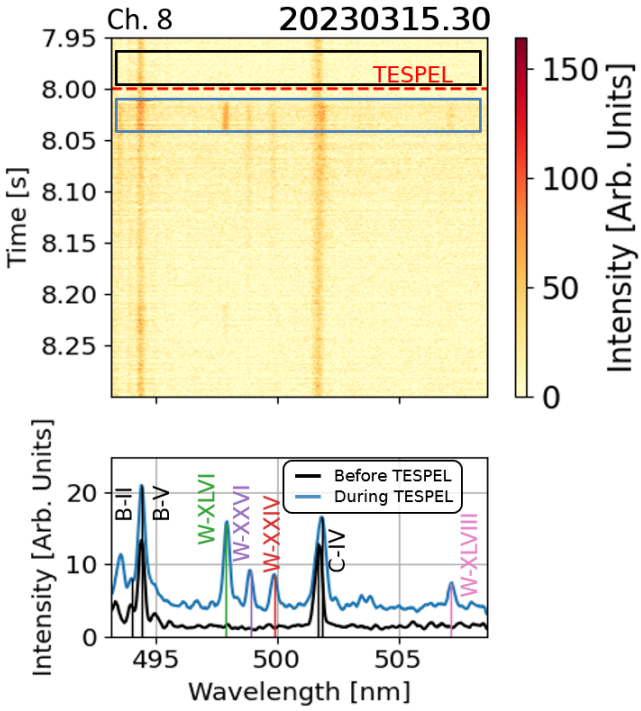


Figure 34: Figure analogous to those shown in figure 33 shown here from channel 8 during a TESPEL injection in experiment #20230315.30.

It is important to note that several W-emission lines are present even in the absence of the neutral beam. This can be explained via the coronal equilibrium model which provides the steady state impurity charge state distributions in the absence of transport and considering the limit where recombination processes are dominated by electron capture reactions. The necessary ionization and recombination rates are tabulated and available through the Open ADAS database. [16, 78]

As can be seen in figure 35, similar charge states (e.g. $Fe^{24+}$ and $W^{24+}$) dominate at very different temperature ranges. While $Fe^{24+}$ may only be present in the core, $W^{24+}$ would likely be present closer to the plasma edge where background neutrals are present that can lead to charge exchange and therefore passive radiation.

In contrast, passive radiation is not seen for emission from higher charge states such as $Fe^{24+}$. This feature can be seen in figure 36. In this experiment, LBO is

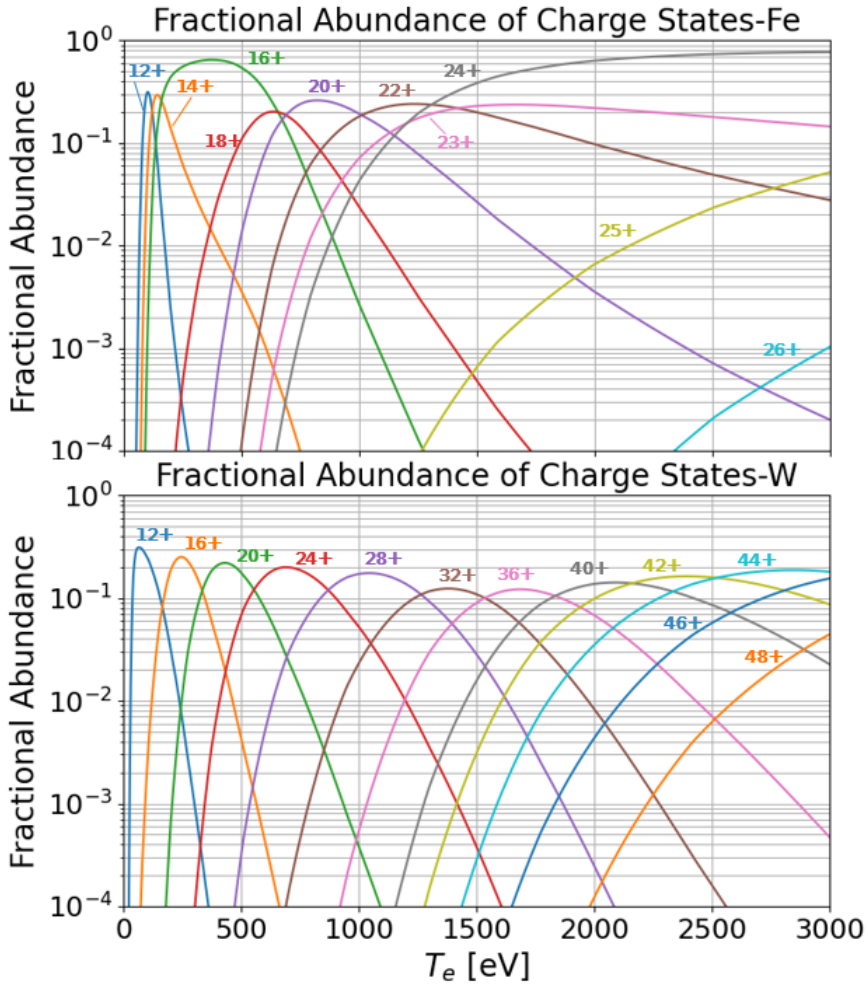


Figure 35: Corona equilibrium charge state distributions for Fe (top) and W (bottom) as a function of temperature and at a density of $5 \times 10^{19}$ $m^{-3}$. For interpretability, not all charge states are shown.

injected into a plasma which has NBI blips fired at 10 Hz. The LBO is synchronized such that injection occurs during one of the "on" phases of the NBI. One can observe the rise in intensity of the various charge states during the first NBI period followed by an abrupt drop to zero during the period without NBI in the Fe XXII and XXIV signals. Once the beam is turned back on, one can clearly see the Fe XXII and Fe XXIV signals return during which they are in their decay phase. This indicates that measurement of Fe XXII and Fe XXIV radiation will provide excellent spatial

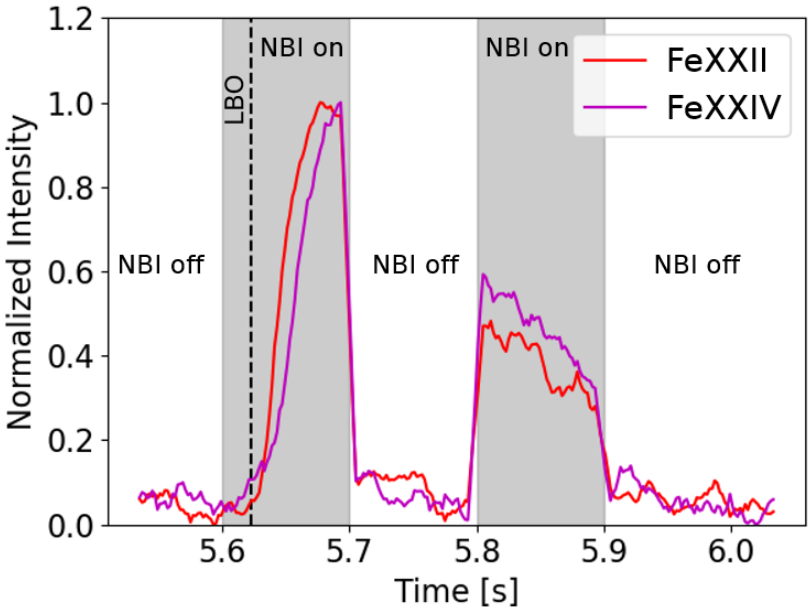


Figure 36: Recorded line intensities for Fe XXII and Fe XXIV following LBO injection into a plasma with NBI switched on and off at a rate of 10 Hz (shot # 20221201.38).

resolution for use in impurity transport studies since all emission will be localized along the neutral beam.

Since NBI heating is a method widely utilized on tokamak and stellarator experiments where plasma temperatures are several keV, the observation of Rydberg states provides an easily implemented strategy for the measurement of impurity emissions. Additionally, by demonstrating that the transition wavelengths are agnostic to the injected impurity species, we have shown that this method can provide a flexible tool that can be used for many different injection experiments.

# 6 Computational Tools for Impurity Inference

The following section describes the computational models and methods used in this work which are necessary to determine the impurity transport coefficients by comparing synthetic diagnostics signals to experimental ones. First, an introduction to Bayesian inference methods is given along with a detailed description of the specific Bayesian statistical model used to infer impurity transport profiles. Following this, we discuss the various codes and techniques used to model the observed impurity emissions.

## 6.1 Bayesian Inference for Plasma Diagnostics

Bayesian inference is a technique that has become increasingly common in physics applications in recent years and is often used in place of or in addition to least squares optimizer approaches. Often, Bayesian inference is used in contexts where datasets are incomplete or a given system is under constrained and provides the user with reasonable error-bars that take into account the information that is or is not available. Bayesian inference is a technique well suited to impurity transport analysis since the 1D modeling has many potential sources of error and it is non-trivial to tie the expected transport of impurity ions to the observed spectroscopy signals. In the following subsection, we will first discuss the underlying concept of Bayesian inference, Bayes theorem. Next the Bayesian inference scheme known as Markov Chain Monte Carlo (MCMC) will be introduced. Finally, a description is given of how the model input uncertainties are propagated to the inferred impurity transport profiles using the Bayesian approach.

### 6.1.1 Bayes' Theorem

Bayesian probability theory is characterized by the determination of the probability of a hypothesis being true when considering both observed data as well as any relevant background knowledge. This is different from the more common "frequentist" approach which considers the probability of observing data given a certain hypothesis. Bayesian approaches have numerous benefits such as greater flexibility to integrate non-identical ensembles of data (i.e. differing metrics and methods) and greater ease in interpretation of model conclusions. The main pillar of any Bayesian framework is Bayes' theorem:

$$p(H|D,I) = p(H|I)p(D|H,I)/p(D|I) \tag{39}$$

Where, in this notation $H$ is considered the "hypothesis" such as a given guess for the question of interest or a specific forward model, $D$ is the information contained within the measured data, and $I$ is the culmination of any previous knowledge (e.g. boundary conditions). Here, the notation $p(A|B)$ indicates the probability of $A$ being true given the assumption that $B$ is true. In Bayes' theorem, $p(H|D,I)$ is known as the posterior, which is the probability of a chosen hypothesis being true given the observed data and prior information. $p(H|I)$ is then what is called the prior, the probability that the hypothesis is true subject only to some already known background information. $p(D|H,I)$, referred to as the likelihood, is the probability of observing the data set of interest under the assumption that the hypothesis and the background information are true. Finally, $p(D|I)$ is called the marginal probability or the evidence. The evidence is a normalization factor such that when the posterior is integrated over all $H$ is equal to 1 (i.e. $p(D|I) = \int p(H|I)p(D|H,I)dH$). Typically evaluation of the evidence is computationally expensive, so in problems such as parameter inference where only the shape of the posterior space is of interest, the evidence is set to 1.

For Bayesian parameter inference, the strategy is typically to first define a prior distribution for the parameters. In practice, the prior distributions can function similarly to bounds one might set in a least squares approximation method. However, by defining a custom probability distribution, one is able to employ a wide variety of constraints that may be difficult to encapsulate via simple bounds on inference parameters. For example, one may set an increasingly severe penalty for moving outside of a given parameter bound rather than setting a hard constraint that the parameter should never exceed the bound. When defining the priors, it is common in Bayesian analysis to solely consider physics based priors such as the knowledge that a given parameter should be of a certain order of magnitude or should not exceed some known physical quantity. After defining the prior probability, a suitable forward model is employed that provides synthetic measurements which can be directly compared with experimental data via the calculation of the likelihood function. The synthetic diagnostics described in section 6.2 act as our forward model in this case. Since the marginal likelihood can be ignored in inference contexts, the posterior is fully defined by specifying the prior and likelihood probabilities. In the case of parameter inference, the next step is to generate a large number of parameter samples that span the posterior distribution space with sufficient resolution. Note that the evidence becomes important when one desires to compare two competing models. These models could be described by completely different sets of parameters which typically makes it difficult to determine which model is better suited for the given problem. For example, competing models could be different ways to parameterize the impurity diffusion profile or alternative ways to handle the model behavior in the SOL region. The evidence provides a measure for how well the model captures the observed data while providing a penalty for "over-fitting" with unnecessarily complex models. Comparing evidences allows one to select the most appropriate model and

can be done by calculating Bayes' factor:

$$B.F. = p_1(D|I)/p_2(D|I) \tag{40}$$

Here $p_1$ and $p_2$ represent evidences calculated for two competing models labeled 1 and 2 respectively. If this factor is larger than 1 it indicates model 1 better explains the measured data.

### 6.1.2 Markov Chain Monte Carlo

As described in the previous section, Bayesian inference is based on the generation of a posterior distribution which can infer the set of parameters by maximizing the posterior probability. Additionally, this method can quantify the uncertainty in the inference. However, so far we have not described how the parameter space itself is sampled to build up the underlying posterior distribution. If a simple Monte Carlo approach is utilized, the time it takes to sample all of the parameter space tends to increase exponentially with the number of parameters being inferred. A more sophisticated method to sample parameter space is known as Markov Chain Monte Carlo (MCMC) which is characterized by taking into account the previously chosen sample. This key feature allows for the sample distribution to be biased towards regions of higher probability while not necessarily disqualifying regions of low probability from being sampled. Several sampling algorithms exist which fall under the category of Markov Chain Monte Carlo [79, 80, 81]. Here we specifically utilize a modified version of the common "Metropolis - Hastings" (MH) algorithm known as the "stretch move". This, along with many additional tools for analysis of MCMC results are easily available in the python module "emcee" [82].

In the MH algorithm, samples are selected using a proposal distribution method

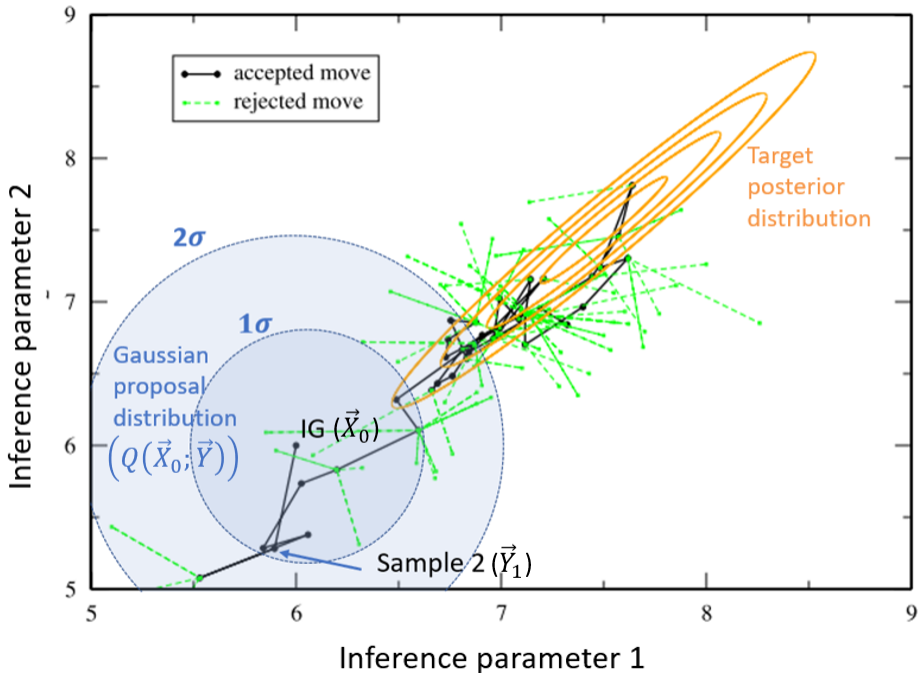


Figure 37: A typical MCMC walk for a Markov Chain sampler. An example bivariate transition distribution is shown in blue surrounding the initial guess. Accepted moves are plotted in black while proposed moves that get rejected are plotted in green. The target posterior distribution is shown as a multivariate normal distribution shown in orange. Figure adapted from: [79]

where the next sample, $\vec{Y_{i+1}}$ is proposed by considering a transition distribution centered around the current sample, $\vec{X}_i$. With $\vec{Y_{i+1}}$ in hand, it is determined whether to accept the sample by generating a random number between 0 and 1 and comparing it to the quantity:

$$min\left(1, \frac{p(\vec{Y_{i+1}}|D,I)Q(\vec{X}_i;\vec{Y_{i+1}})}{p(\vec{X}_i|D,I)Q(\vec{Y_{i+1}};\vec{X_i})}\right) \tag{41}$$

Here, $Q$ represents a transition distribution which bounds the region of possible new samples and is typically selected to be easy to sample. A common choice for such a transition distribution is a multivariate Gaussian centered around $\vec{X}_i$, the previous sample. As sampling progresses, the covariance matrix for this multivariate Gaussian is tuned to optimize performance [82]. If the selected random number is less than

the evaluation of eq. 41, the sample is "accepted" and added to the chain (i.e. $\vec{X_{i+1}} = \vec{Y_{i+1}}$) otherwise a new sample is proposed and the process is repeated. In this scheme, new samples with posterior probabilities greater than the previous sample are always accepted, and those with lower probabilities are potentially accepted with some non-zero probability. An example of the path taken by a MCMC sampler is given in Fig. 37. Here, a proposal distribution shown in blue is drawn around an initial guess (marked "IG"). A second sample is then drawn from this proposal distribution and the resulting posterior probability is compared between the two and it is accepted by evaluating equation 41 and comparing to a random number draw. This process repeats with accepted sample steps shown in black and rejected ones shown in green. As the sampling scheme continues, one can see that it begins to reflect the structure of the target posterior distribution.

The actual sampling algorithm used in emcee, known as the "stretch move" follows a similar scheme to the basic MH algorithm. The motivation for this is the desire to have a so-called "affine invariant" sampler where the performance is independent of the target posterior distribution aspect ratio (e.g. the highly elongated distribution shown in figure 37) [83]. In this method, the proposal of new samples for a given Markov chain is based instead on the current positions of several other Markov chains which are simultaneously generated. These coupled chains are referred to as "walkers" in the emcee documentation. The specifics of this stretch move scheme are not described here but can be found in the original publication of the algorithm [83].

The metric which is typically used to determine convergence in MCMC schemes is referred to as the auto correlation time. This value is calculated by the algorithm at each step and is an estimate of the number of steps required such that the walkers are drawing independent samples from the target distribution. The method used to calculate this quantity in emcee is described in the following reference: [82].

### 6.1.3 Parametrization of Diffusion & Peaking Ratio Profile

The impurity diffusion and convection profiles are the main quantities of interest for this Bayesian inference problem. These profiles are defined as functions or $r/a$ and are input to pySTRAHL (via equation 23) for the purpose of calculating the impurity densities and emissions. Here, we choose to apply a single set of diffusion and convection profiles which govern each of the impurity charge states equally. This choice greatly simplifies the inference problem and is motivated by the expectation of turbulent like transport that does not depend on impurity charge. Additionally, since the quantity that governs the equilibrium impurity profile shape is the peaking ratio $rV/D$ (here $r$ is the minor radius), it is fitted rather than the convection velocity specifically. The choice of fitting the peaking ratio also implicitly ties the diffusion and convection to one another since plasma instabilities at a particular location will inevitably affect both the $D$ and $V$ values. To parametrize $D$ and $rV/D$ we choose to utilize so-called piece-wise cubic-Hermite interpolating polynomial (PCHIP) spline functions which avoid overshooting between knot points [84]. The $D$ and $rV/D$ splines are then defined by three knot points which can vary in magnitude. The location of the middle knot point is additionally allowed to vary independently for both $D$ and $rV/D$ with the two outer knot points fixed. Additionally, an ad-hoc $D$ and $rV/D$ in the SOL of 0.5 $m^2/s$ and 0 respectively are chosen to reduce model complexity. This choice is deemed acceptable since the transport in the SOL is described by several closely tied parameters (diffusion, convection, SOL loss rate, number of injected impurities) which in the end determine the total number of impurities which reach the LCFS. By fitting the loss-rate, the model has sufficient variability to explain the experimental data. Additionally, the $rV/D$ ratio is set to zero at $r/a = 0$ to avoid non-physical singularities which could appear in equation 23. An example of such a $D$ and $rV/D$

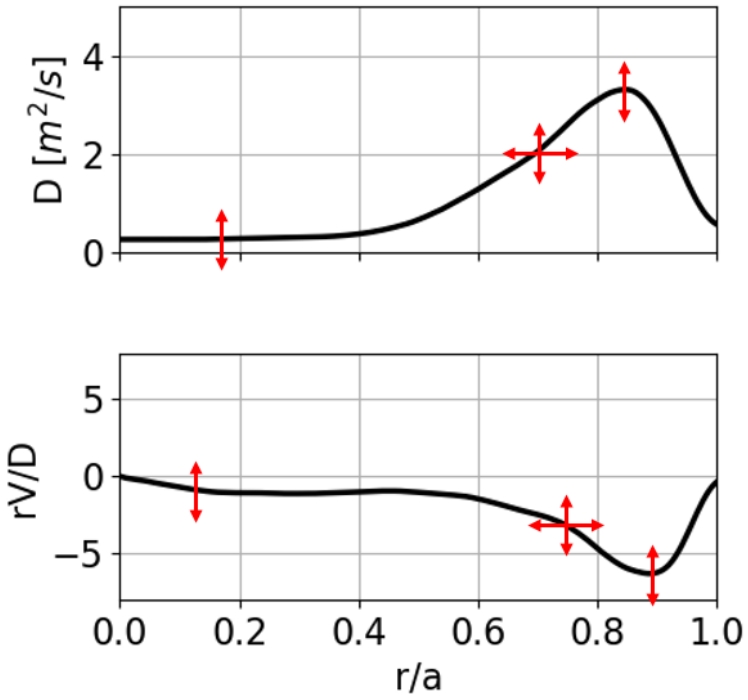


Figure 38: An example diffusion and peaking ratio profile which are parametrized using the PCHIP spline function with three knot points that vary in magnitude and one that additionally varies in position.

profile is given in figure 38. In total, the transport profiles are defined by eight free parameters: three which set the magnitudes for $D$, three which set the magnitudes for $rV/D$, and two which define the central knot point locations. Additionally fitted is the loss rate in the edge as well as the "nuisance parameters" described in section 6.1.5 which characterize the model uncertainty.

### 6.1.4 Choice of Priors

One of the most important aspects of Bayesian inference is the way in which the user defines the prior probability distributions. If one chooses a particularly restrictive prior, the posterior distribution and therefore the resulting inference can be significantly biased towards a given result. In some cases, this can be an advantage as one

should expect the result to follow known physical laws. In other cases, care needs to be taken as biased results could rule out plausible inferences. In this work, we choose to keep the priors fairly non-restrictive only introducing physics motivated bounds. This allows the MCMC scheme to explore many possible explanations for the observed impurity signals.

The first prior choice is known as Jefferys prior and is assigned for any fitting parameter that can vary over many orders of magnitude. This is the case for the diffusion magnitude and the loss rate in the edge. In this case, the inference parameter is the log of the parameter of interest such that all orders of magnitude are equally likely. Next, a so-called "uniform" prior is defined for each inference parameter, including those that are additionally bounded by Jefferys prior. The uniform prior functionally has the form of a step function. In this sense, the user-defined prior function returns a probability of 1 if the parameter finds itself inside a set of bounds and 0 if it is outside. For the diffusion, these bounds are set as 0.01 $m^2/s$ and 100 $m^2/s$ which correspond to the approximate magnitudes for classical and Bohm diffusion, two extreme scenarios for low transport and high transport respectively. The classical diffusion level can be calculated as $D_{cl} = \rho^2\nu$ where $\rho$ is the Larmor radius and $\nu$ is the electron ion collision frequency. Bohm diffusion can then be calculated as $D_{Bohm} = k_B T/16eB$. The peaking ratio in turn, can vary between the nonrestrictive bounds of $-100$ to 100 which would correspond to unphysical extremely peaked or hollow impurity density profiles. Next, the two central knot points which partly define the $D$ and $rV/D$ profile shapes are bounded between $r/a = 0.2$ and $r/a = 0.75$ preventing them from getting too close to the static core and edge knot points. The parallel loss rates in the edge are then allowed to scale up and down by a factor in the range of $10^{-10} - 10^{10}$. Finally, the remaining uniform prior bounds are chosen to allow the uncertainties in the atomic and rate data to vary according

to the description given in section 6.1.5.

### 6.1.5 Handling of Uncertainties in Model Inputs

Bayesian frameworks allow for robust accounting of experimental and inference uncertainties. In practice, this can be accomplished by allowing the relevant inputs to the forward model to vary according to their levels of uncertainty and including them as so-called "nuisance" parameters in the inference [79]. For the analysis presented here, the largest sources of model uncertainty will be the kinetic profiles and the atomic data used when modeling the ionization balance and emission intensities.

First, the background electron temperature has a strong effect on the impurity ionization/recombination rates which will determine the forward modeled charge state balance. Therefore the uncertainty in the $T_e$ profile must be accounted for by allowing it to vary within the experimental uncertainty depicted in figure 49. Moreover, MCMC inferences may require upwards of one million evaluations of the forward model to converge. For this reason, interpolating the tabulated rates onto the randomly sampled temperature profile at each step would greatly increase the computation time. To address this, 1000 temperature profiles spanning the uncertainty bounds are selected prior to the inference for which the rates are calculated and stored in an array. At each step of the inference, a "nuisance" fit parameter selects which of these rate entries to use for the calculation.

Additionally, the beam attenuation, and therefore the density of neutrals along the sight-lines depends strongly on the electron density profile. To include the effect of the uncertainty in $n_e$, the beam attenuation is evaluated using pyFIDASIM for the case of an $n_e$ profile scaled either up or down based on the error bars shown in figure 49. This gives two bounds for the possible beam attenuation. Another nuisance parameter then chooses a sample beam attenuation profile which is linearly

interpolated between these two bounds.

Finally, once a set of kinetic profiles is sampled and the ADAS rate coefficients for ionization, recombination, and radiated power are determined, an additional uncertainty of 15% in the rates themselves is considered based on previously reported estimates of their expected error [85]. The uncertainty in the rate coefficients is assumed to be independent for each process (i.e. ACD, SCD, CCD, PLT, PRB, and PRC coefficients). Finally, the inference parameters are sampled using the markov chain monte carlo method to determine the structure of the posterior distribution[82].

### 6.1.6 Calculation of Uncertainty in Fitted D and rV/D

One of the more important outputs of a MCMC inference scheme is the fitting uncertainty on both the fitted parameters as well as the forward modeled signals. Following an inference, the user is given a large array of parameter samples which, in n-dimensional space (here n being the number of fit parameters), will have the highest density near the location where the posterior probability is maximized. Characterizing the uncertainty is then a matter of evaluating how spread out the population is from that maximum point. If one wishes only to know the uncertainty of a particular fit parameter, they can take each sample for that parameter, sort them, and then calculate the percentiles. Assuming the parameter samples are distributed according to a normal distribution, the $-2\sigma$, $-1\sigma$, $+1\sigma$, and $+2\sigma$ standard deviations correspond approximately to percentiles of 2.1%, 13.6%, 84.4%, and 97.9%. While not all of our samples will be normally distributed around a central value, we will still use the standard deviation nomenclature to describe the uncertainty. An example of a distribution of potential diffusion values from section 7.2 is given in figure 39. Here, the percentile borders are given by vertical lines which can then be used to assign error bars.

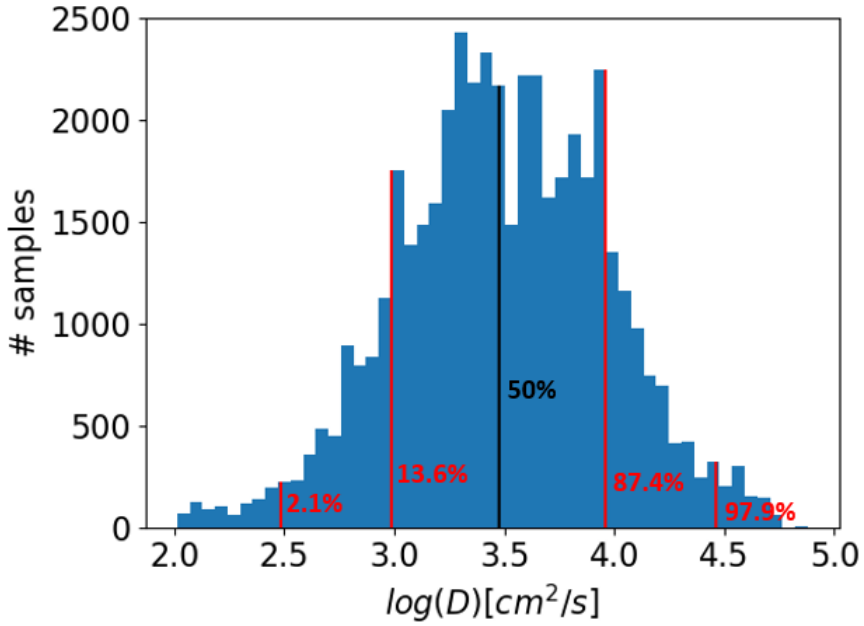


Figure 39: Histogram of an inference parameter sample population following a MCMC inference. The $\pm 1\sigma$ and $\pm 2\sigma$ confidence intervals are indicated by vertical lines.

Typically, if one wishes to propagate the uncertainty in the individual parameters to quantities of interest, they may use standard uncertainty propagation formulas. However, these are only of use when the operations to go from the fitted parameter to the quantity of interest are relatively simple (e.g. are captured by analytic formulas). Since we would like to evaluate the uncertainties of the $D$ and $rV/D$ profiles (and the fitted signals themselves) which are not simply described by basic mathematical operations, we choose to propagate our uncertainties using a Monte Carlo-like approach. Starting from our inference output of $\sim 50,000-100,000$ samples, a subset of 500 samples is selected at random which will have the same underlying distribution as the full population. Next, the corresponding $D$, $rV/D$, and synthetic signals can be calculated for each of these samples. We now have a new sample population of $D$ and $rV/D$ profiles as well as synthetic signals. Finally, the percentiles corresponding to $\pm 1\sigma$ and $\pm 2\sigma$ can be evaluated at each radial or temporal point for the transport

profiles and synthetic signals respectively. Throughout the text, when fitted transport profiles are shown, these uncertainty bands are shown along with the median profile samples. Note, we choose to show the median sample rather than the best fit sample since a single excellent sample should not outweigh the possibility of many very good samples. In most cases however, the median and best samples are similar to one another. When showing fits to the measured data however, we instead choose to depict the best fit sample (the one with the highest posterior probability) since this is a useful metric for how well the model can explain the data.

## 6.2 Forward Modeling of Experimental Signals

### 6.2.1 pySTRAHL

The STRAHL code, originally written in 1980, has been a useful tool for the simulation of impurity transport in toroidal plasma devices [86]. More recently, we have translated the main routine into python, allowing for increased functionality and compatibility with other simulations [2].

When modeling impurity transport, the particle conservation equation from Eq. 22 needs to be modified to account for the ionization and recombination of impurity ions which will act as source or sink terms:

$$\frac{\partial n}{\partial t} = -\nabla \cdot \Gamma + Q_{I,z}. \tag{42}$$

Here $Q_{I,Z}$ describes all of the source and sink terms due to the ionization and recombination:

$$Q_{I,z} = -(n_e S_{I,z} + n_e \alpha_{I,z} + n_H \alpha^{CX}_{I,z}) n_{I,z} + n_e S_{I,z-1} n_{I,z-1} + (n_e \alpha_{I,z+1} + n_H \alpha^{CX}_{I,z+1}) n_{I,z+1}. \quad (43)$$

Here, $n_e$, $n_H$, and $n_{I,z}$ correspond to the densities for the electrons, neutral hydrogen, and the impurity ions of charge state $z$. $S_{I,z}$ and $\alpha_{I,z}$ correspond to rate coefficients for the ionization and recombination (due to capture of an electron) of impurity ions of charge state $z$. $\alpha^{CX}_{I,z}$ represents the rate coefficient for recombination due to charge exchange with hydrogen neutrals. Due to these source and sink terms, the dynamics of a given impurity charge state population is not only governed by the radial transport but is also coupled to the adjacent charge states via interaction with the background plasma and neutrals.

Most often, the transport of impurities is assumed to be 1D in nature with particle fluxes primarily considered in the direction perpendicular to the flux surfaces. This is motivated by the same argument that is used to justify the main ion parameters as so-called "flux functions". Since the parallel streaming velocity is so large compared to perpendicular transport processes, the densities of the impurities have time to equilibrate along the magnetic surfaces. One phenomena which can potentially complicate this assumption is the finite ionization time of the impurities which can potentially be shorter than the toroidal transit time. In the case of localized sources such as purposeful injection, impurities may undergo several ionization events before they have time to equilibrate across the flux surface such that the 1D approximation might be violated. It is therefore important to evaluate the ratio of the ionization time to the parallel streaming time: $S_{I,Z}/RV_{\|}$. Here $S_{I,Z}$ is the ionization rate for an impurity species, $I$ in ionization state, $Z$. $R$ is the major radius of the device

and $V_{\|}$ is the parallel ion velocity (again, usually taken to be the thermal speed), the product of which gives an order of magnitude estimate for the time it takes to spread out across a flux surface. If this ratio is greater than 1, which is typically the case for highly ionized impurities, the one dimensional model is appropriate.

To model impurity transport in pySTRAHL, equation 42 is converted to a vector equation such that each component of the vector corresponds to a different charge state (for now neglecting neutral sourcing and edge losses):

$$\frac{\partial \vec{n}}{\partial t} = \frac{1}{r}\frac{\partial}{\partial r} r[\hat{D}(r)\frac{\partial \vec{n}}{\partial r} - \hat{v}(r)\vec{n}] - \hat{S}\vec{n} - \hat{R}\vec{n} \tag{44}$$

Here, $\hat{D}$ and $\hat{v}$ are diagonal matrices with the convective and diffusive transport coefficients for each charge state. $\hat{S}$ and $\hat{R}$ are the rate coefficients for ionization and recombination respectively with $\hat{R}$ accounting for both electron recombination as well as charge exchange recombination. As an input, the code takes radial profiles for the electron temperature, electron density, neutral hydrogen density, $\hat{D}$, and $\hat{v}$. The kinetic profiles are then used to determine ionization, recombination, and charge exchange rates via tabulated rate coefficients from the ADAS database [16].

#### 6.2.1.1 Neutral Sourcing

One should note that equation 44 is lacking a source term for the first ionization state directly from the neutral impurity atoms. This requires a different treatment since the neutral impurities will not follow field lines and therefore should not be described by the 1D simplification in the transport equation. The way this is modeled in pystrahl is by considering the neutral impurity ionization rate along the LBO injection path.

In addition to its dependence on the edge kinetic profiles, the source function

depends on the exact orientation of the injection path relative to the 3D field. Hence, neutral impurities will penetrate a certain distance into the confined region depending on the 3D geometry. In order to estimate the neutral impurity deposition profile, the flux coordinate $s$ is calculated along the LBO line of sight with the aid of a 3D grid generated by an extended VMEC equilibrium[1][87]. The in-fluxing neutral population is then attenuated at each grid point subject to exponential decay set by the competing local ionization and recombination rates. An exponential attenuation factor for the neutral species is defined at each radial grid point (index designated by $i$):

$$n_{dep,i} = \frac{n_{I,edge} r_{edge}}{r_i} e^{-\lambda_i} \tag{45}$$

Here, $r_{edge}/r_i$ represents the ratio of the effective radius of the LCFS to that of the radial grid point (and therefore the ratio of their circumferences) and accounts for the spreading out of the flux surfaces. The attenuation factor, $\lambda_i$, which relates the ionization rate to the impurity velocity is defined at each grid point:

$$\lambda_i = \lambda_{i+1} + \frac{1}{2v_0}(dr_{i+1} S_{i+1} + dr_i S_i) \tag{46}$$

Here, $d_r$ is the spacing between flux surfaces in real space coordinates, $v_0$ is the in-fluxing speed of the injected impurities, and $S$ is the ionization rate of the neutral impurities which can be determined from the local temperature and density values. The impurity injection velocity is calculated by considering an injection energy of 20 eV (based on previous measurements via a fast camera [23]). For impurity injections, the source term also has a time varying component, $\gamma(t)$, which represents the duration of the injection impulse. In the simulations performed here, $\gamma(t)$ is set to a 2

[1]The extended VMEC equilibrium can be generated by redefining the total magnetic flux at the LCFS when running VMEC

ms wide Gaussian. Therefore, the full impurity source term is $d(r,t) = n_{dep,i}(r)\gamma(t)$ The impurity sourcing can then be included in the impurity transport equation as an additional term, $\vec{d}$ which is zero for all charge states except the first ionization stage which has the value of $d$.

#### 6.2.1.2 Edge Loss Rate

When treating the edge region outside of $r/a = 1$, one must additionally consider the parallel loss of impurities as they stream to the divertor. Those ions still experience transport due to diffusion and convection in this region but are depleted according to a characteristic loss time. Mathematically, this is represented by the addition of a term, $-\vec{n}/\tau_{\|}$ on the right hand side of equation 44. Here, the parallel loss time, $\tau_{\|}$ is calculated as the ratio of the divertor connection length to the parallel flow velocity (which is assumed to be the impurity ion thermal velocity). Inside the LCFS, the connection length is infinite and therefore the loss rate is zero. The main effect of the loss rate is that it balances with the transport in the edge to set the number of impurities that penetrate into the confined region. As mentioned previously, since in our simulations we choose an ansatz for the edge transport, the edge loss rate is allowed to vary in the inference by a multiplicative factor which therefore sets the number of impurities which reach the confined region from the SOL. Finally, considering both the impurity sourcing term and the parallel loss, the full 1D impurity transport equation solved by pySTRAHL can be written as:

$$\frac{\partial \vec{n}}{\partial t} = \frac{1}{r}\frac{\partial}{\partial r} r[\hat{D}(r)\frac{\partial \vec{n}}{\partial r} - \hat{v}(r)\vec{n}] - \hat{S}\vec{n} - \hat{R}\vec{n} - \frac{\vec{n}}{\tau_{\|}} + \vec{d} \tag{47}$$

Evolving this equation in an iterative manner allows the user to calculate the impurity charge state densities as a function of time and position.

#### 6.2.1.3 3D Effects

The 1D calculation described previously assumes a circular plasma cross section. In order to improve the applicability of pySTRAHL to stellarator geometries, the 3D shape of the field is considered. Each flux surface can be assigned an effective radius defined relative to its enclosed volume:

$$r_{eff} = \sqrt{\frac{V}{2\pi^2 R}} \tag{48}$$

Here, V is the volume contained within a given flux surface and R is the major radius. These volumes can be calculated using 3D VMEC equilibria [87]. This transformation allows for radial profiles to be mapped onto their relevant flux surfaces.

Since equation 47 is a 1D model, care must be taken to account for the 3D effects that enter into the terms which are defined in the edge region. In the SOL, the temperatures and densities can vary along field lines, making it difficult to assign meaningful ionization and recombination rates for $r/a > 1$. To handle this problem, we assume a level of uncertainty with which the rates can vary when inferring the impurity diffusion and convection (see section 6.1.5). Of particular importance when considering the SOL, is the location of the injection with respect to the island divertor. For OP 2.1, the LBO system is incident on the 5/5 island chain in the scrape off layer. To characterize the edge plasma, a multi-purpose manipulator (MPM) system is available which allows for measurement of plasma temperature and density in the edge by plunging a probe system into the SOL[88]. While this MPM system is

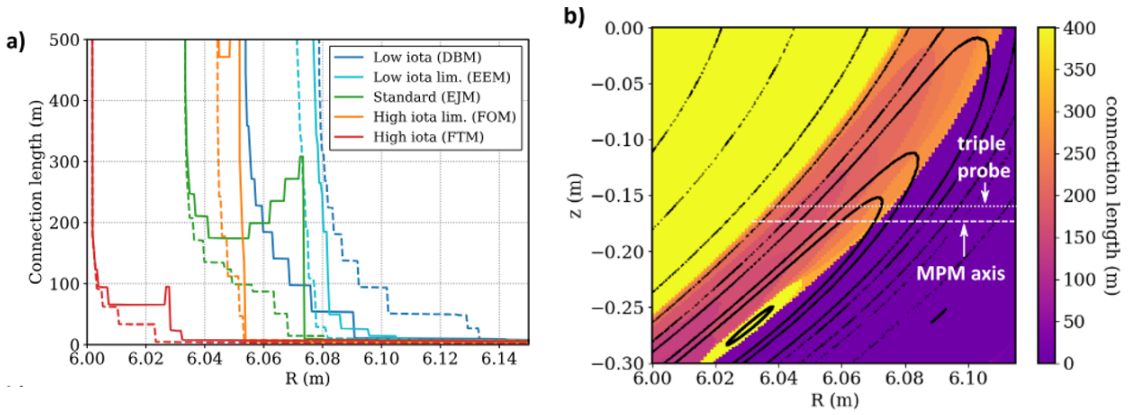


Figure 40: a) Connection lengths along the MPM axis for a variety of magnetic configurations. Forward direction (aligned with **B** ) is given by the solid lines with reverse direction (anti-aligned with **B** ) given by dashed lines. b) Standard configuration connection lengths (forward direction) to the island divertor tiles with the MPM axis given by the white dashed line. A Poincare plot of the field structure is overlaid. Figure credit: [88].

toroidaly separated from the LBO location by $\sim 22°$, it measures the same island structure such that its measurements can be considered representative of the LBO injection path. Figure 40, shows the connection lengths along the path of the MPM axis as well as the poloidal plane where the MPM path intersects the island. In figure 40a, forward direction (in the direction of the field) connection lengths for the standard configuration are given by the green lines which are in the range of 200-300 m in the SOL and drop to near zero around $R = 6.075$ m. This is because in this region, the field lines are directly in the shadow of the island divertor meaning that any particle streaming along the field will meet a tile in less than one full toroidal transit. At $R = 6.035$ m, the connection length blows up to infinity, indicating the LCFS boundary.

The effect of the divertor shadow can be seen experimentally by probes attached to the MPM[88]. Figure 41 shows the measured electron temperatures and densities for a variety of plasma conditions. Here, it can be seen that in the divertor shadow

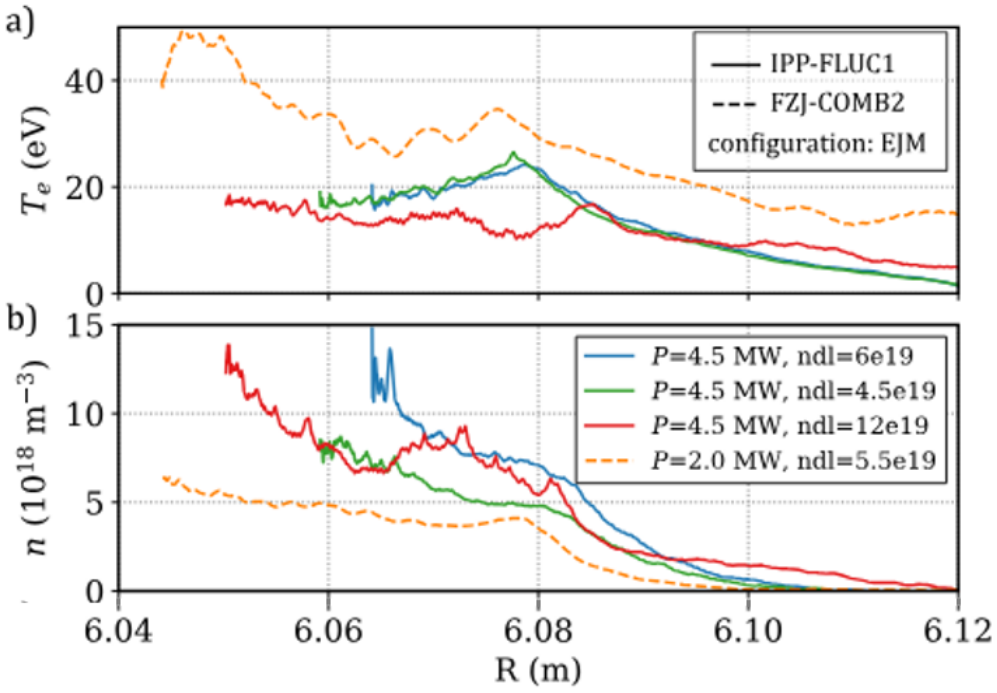


Figure 41: Measured electron temperature and density along the MPM path during a variety of experiments in the standard magnetic configuration. The solid and dashed lines depict data collected using two different probe heads. Figure adapted from: [88].

region, the densities and temperatures decay quickly as the probe moves further into the shadow. Consideration of these local edge temperatures have an important effect on the local ionization rate for $Fe^0+$ and therefore the impurity source rate.

To represent the trend seen in figure 41, the $T_e$ and $n_e$ profiles in the edge are chosen to be flat with a value equal to the Thomson measurement at the LCFS and then decay exponentially in the divertor shadow region with a decay length of 2 cm. Based on figure 40, the divertor shadow region is set to be 4 cm outside of the LCFS. Example kinetic profiles in the SOL region are shown in figure 42 for the conditions considered in discharge #20230314.26.

The extremely short connection lengths present in the shadow of the divertor will also have an effect on the loss rate in the edge, calculated as $V_f/L_c$, the flow velocity

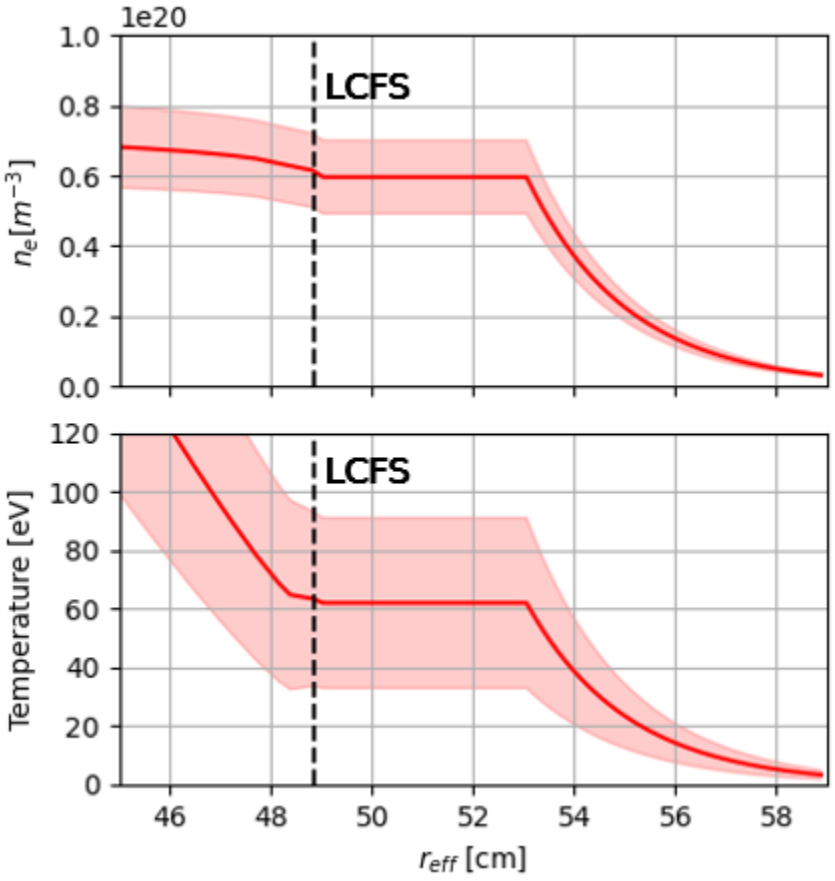


Figure 42: Edge profiles used in pySTRAHL to simulate the background plasma in discharge #20230314.26. $1\sigma$ uncertainty bands are shown in shaded red.

(which is assumed to be the thermal velocity) divided by the connection length. The main effect of the loss rate is that it balances with the transport in the edge to set the number of impurities that penetrate into the confined region. To simplify the model, a constant connection length of 250 m is considered up to the divertor shadow where it drops to near zero.

#### 6.2.1.4 Numerical Algorithm

The expanded form of equation 47 is:

$$\frac{\partial \vec{n}}{\partial t} = \hat{D}\frac{\partial^2 \vec{n}}{\partial r^2} + \left(\frac{\hat{D}}{r} + \frac{d\hat{D}}{dr} - \hat{v}\right)\frac{\partial \vec{n}}{\partial r} - \left(\frac{\hat{v}}{r} + \frac{d\hat{v}}{dr}\right)\vec{n} - \hat{S}\vec{n} - \hat{R}\vec{n} - \frac{\vec{n}}{\tau_{\|}} + \vec{d} \tag{49}$$

In pySTRAHL, the equation is discretized using the Crank-Nicolson scheme [86, 89]. In this approach, the density is evolved over a time step of $\Delta t = t_{l+1} - t_l$ by calculating the average value of the densities and spatial derivatives of the $l$ and $l+1$ time indices:

$$\vec{n}^{l+1/2} = \frac{\vec{n}^{l} + \vec{n}^{l+1}}{2} \tag{50}$$

With this definition, we can rewrite equation 49 in the Crank-Nicolson form:

$$\frac{\vec{n}^{l+1} - \vec{n}^{l}}{\Delta t} = \hat{D}\frac{\partial^2 \vec{n}^{l+1/2}}{\partial r^2} + \left(\frac{\hat{D}}{r} + \frac{d\hat{D}}{dr} - \hat{v}\right)\frac{\partial \vec{n}^{l+1/2}}{\partial r} - \left(\frac{\hat{v}}{r} + \frac{d\hat{v}}{dr}\right)\vec{n}^{l+1/2} - \hat{S}\vec{n}^{l+1/2} - \hat{R}\vec{n}^{l+1/2} - \frac{\vec{n}^{l+1/2}}{\tau_{\|}} + \vec{d} \tag{51}$$

The radial grid is then discretized into $N$ equidistant radial grid points spaced by a distance of $\Delta r$. The partial spatial derivatives in equation 51 are then written out for a particular radial grid point $k$:

$$\left[\frac{\partial f}{\partial r}\right]_k = \frac{f_{k+1} - f_{k-1}}{2\Delta r} + \frac{\Delta r^2}{6}\left[\frac{\partial^3 f}{\partial r^3}\right] + O\left(\Delta r^4\right) \tag{52}$$

$$\left[\frac{\partial^2 f}{\partial r^2}\right]_k = \frac{f_{k+1} - 2f_k + f_{k-1}}{\Delta r^2} + \frac{\Delta r^2}{12}\left[\frac{\partial^4 f}{\partial r^4}\right]_k + O\left(\Delta r^4\right) \tag{53}$$

with an error due to the discretization of order $\Delta r^4$. With the temporal and spatial discretization included, the calculation now has a linear system of $N \times Z$ equations. This system of equations is then solved using a two step iterative method which which first solves the equations for ascending $Z$ followed by a second set of solutions for descending $Z$. This scheme has been described previously in [90].

### 6.2.2 pyFIDASIM

pyFIDASIM is a python based implementation of the FIDASIM code and is a Monte Carlo algorithm for simulating neutral species in a background plasma [91, 3, 92]. For the presented work, pyFIDASIM is used for the simulation of both beam injected neutrals as well as those present in the background plasma.

For the injection of beam neutrals, a sourcing position and direction is defined which determines their trajectory in a 3D simulation grid. The impinging neutrals are then modeled by "markers" where each marker represents a flux of neutrals, $\Gamma$ that penetrates into the plasma. For this population of neutrals, tabulated effective rates are used to determine the excitation and ionization due to collisions with the background plasma at each spatial grid point. More specifically, each marker is characterized by a flux of neutrals with principal quantum numbers between $n = 1$ and $n = 6$ for which collisions are modeled by a coupled set of differential equations [3]:

$$\begin{pmatrix} d\Gamma_1/dt \\ d\Gamma_2/dt \\ \vdots \\ d\Gamma_6/dt \end{pmatrix} = \begin{pmatrix} a_{11} & a_{12} & \dots & a_{16} \\ a_{21} & a_{22} & \dots & a_{26} \\ \vdots & \vdots & \ddots & \vdots \\ a_{61} & a_{62} & \dots & a_{66} \end{pmatrix} \begin{pmatrix} \Gamma_1 \\ \Gamma_2 \\ \vdots \\ \Gamma_6 \end{pmatrix} \tag{54}$$

Here, the 6x6 matrix represents the rates at which the neutrals at a given energy

level are sourced or lost. The off diagonal elements represent transitions from one energy level to another while the diagonal elements represent loss mechanisms such as charge exchange, impact ionization, and excitation into energy levels with $n > 6$. These rates are then assigned as a function of the neutral's energy per atomic mass and the background ion temperature. An example of a neutral beam simulation for a W7-X plasma was given in Fig. 24.

In addition to simulating beam neutrals, pyFIDASIM calculates the 3D distribution of background neutrals. For this calculation, a neutral sourcing term is defined based on EMC3-EIRENE simulations. This gives vital sourcing information related to the geometry of the vacuum vessel and other plasma facing components (e.g. the divertor, limiter, etc.). Neutrals are then injected using the Monte Carlo scheme and a charge exchange random walk is considered. This provides a spatial distribution of the background neutrals. Finally, it should be noted that the distribution of background neutrals calculated by pyFIDASIM are only resolved qualitatively. That is, the actual magnitude of the neutral density is not solved and the user must scale the distribution by either inferring the neutral magnitude as an additional fitting parameter in optimization problems, or by comparing with measurements. However, previous sensitivity studies on W7-X LBO experiments have indicated that the resulting impurity transport profiles have very little dependence on the order of magnitude of the background neutral density[69].

### 6.2.3 Synthetic Diagnostic For CXRS Measurements

To model the CX emission, the impurity densities calculated with pySTRAHL are combined with the neutral beam densities calculated with pyFIDASIM. The equation for the charge exchange emission seen along a given sight-line is:

$$\epsilon_{LOS} = \int n_z(\vec{x}, t) \sum_k \sum_E n_{k,E}(\vec{x}) \varepsilon_{k,E}(T_i(\vec{x}), n_e(\vec{x}))\ dl \tag{55}$$

Here $n_z$ is the impurity density for charge state $z$ and the sum over $k$ and $E$ represents the sum over the neutral excited states and beam energy components respectively. $n_{k,E}$ is the neutral density of excited state $k$ and energy component $E$ which comprises of the full, half, and third components as well as the NBI halo. The impurity densities and neutral densities are calculated using the pySTRAHL and pyFIDASIM codes respectively. Finally, $\varepsilon_{k,E}$ represents the effective emission coefficient for a given energy component and neutral excited state and describes the number of photons emitted for a particular transition per impurity density per neutral density.

Effective emission coefficients for many low to medium Z impurities are tabulated in atomic data repositories, however, for heavier impurities, few datasets are available. In this work, we are studying emission from injected iron which also does not have emission data. Additionally, the CX cross sectional data (and therefore the emission coefficient data) is typically the same or very similar for like charge states (i.e. the same for Fe 16+ and Ar 16+). Therefore, to simplify equation 55, one can make notes of trends from the heaviest dataset available, argon [93]. For a set of representative argon datasets (these differ by the method used to calculate the CX cross sections), the effective emission coefficients are given as a function of beam energy in Figure 43a. Considering the two datasets shown (labeled UAM and ORNL), the relative contributions to the observed CX signal for Ar XVI n = 15–14 is shown in Figure 43b.

In particular, one can note that for a 50 keV/amu beam, the third energy component ($E = 3$) and beam halo with $k = 1$ contribute at most a few percent to the total signal. The emission coefficient for the $k = 2$ excited state can potentially be

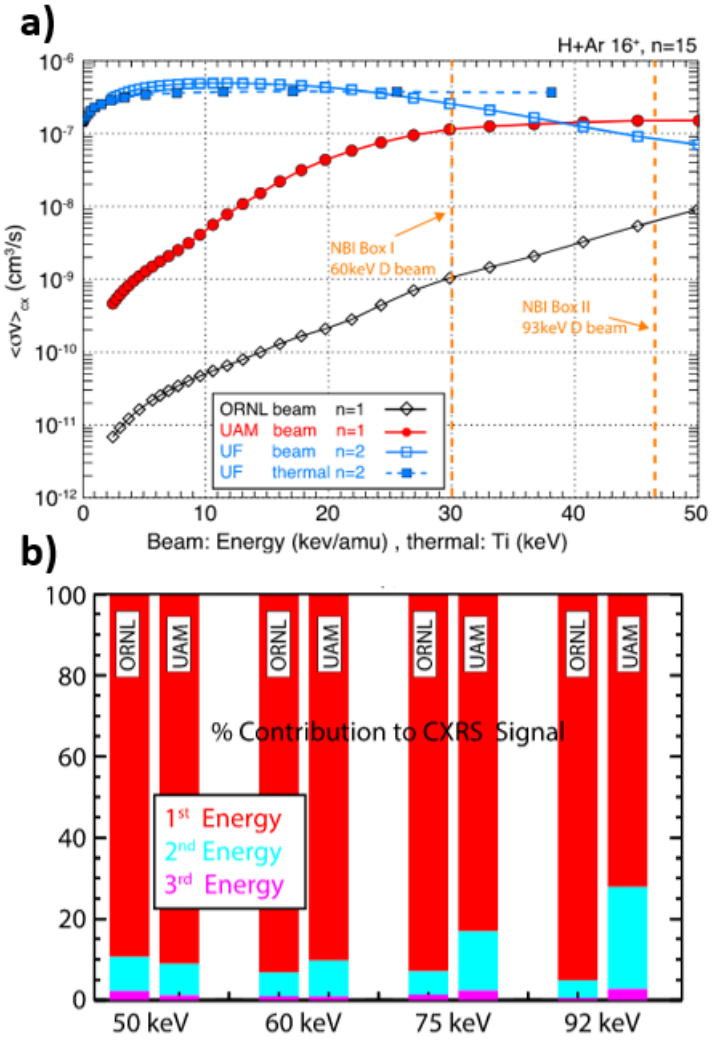


Figure 43: **a**) Effective charge exchange emission coefficients for Ar XVI n = 15–14 as a function of beam energy for several datasets and principle quantum numbers. **b**) Percent contribution to the total emission strength for two datasets at different beam energies.

comparable or even slightly larger than the emission coefficient of the n=1 first energy component however, in the simulations performed in this work, the neutral densities of the $k = 2$ excited states were found to be nearly four orders of magnitude smaller than the corresponding $k = 1$ populations. This is shown in figure 24 which depicts the relative densities of the various beam energy components and excitation states

integrated over the toroidal and poloidal directions. Neglecting the halo component and third energy component as well as the excited states where n > 1, equation 55 simplifies to the following form:

$$\epsilon_{LOS} \approx \int n_z(\vec{x},t)\left(n_{k=1,full}(\vec{x})\varepsilon_{k=1,full}(T_i(\vec{x}),n_e(\vec{x})) + n_{k=1,half}\varepsilon_{k=1,half}(T_i(\vec{x}),n_e(\vec{x}))\right)dl \tag{56}$$

The process used to calculate the effective emission coefficients typically involves an integration over the relative collision velocities between beam neutrals and the impurities. Here, we note that the beam velocity is much larger than the thermal velocity of the ions such that we can treat the distribution as a delta function centered at the beam velocity. This allows one to pull the emission coefficients outside of the integral since it approximately does not depend on the local plasma parameters:

$$\epsilon_{LOS} \approx \varepsilon_{k=1,full}\int n_z(\vec{x},t)n_{k=1,full}(\vec{x})dl + \varepsilon_{k=1,half}\int n_z(\vec{x},t)n_{k=1,half}(\vec{x})dl \tag{57}$$

Simplifying the model in this way allows one to go from considering a total of 6 emission coefficients at each point along the line of sight down to just 2 emission coefficients which can be assumed constant along the line of sight.

#### 6.2.3.1 Calculation of Effective Emission Coefficients for Fe Ions

To accurately model the radiation intensities in equation 57, the effective emission coefficients must be known for the iron species studied in this work. The number of photons emitted per unit volume per second (which is proportional to the effective emission coefficient) for a given energy level transition $i \rightarrow j$ is $N_i A_{i\rightarrow j}$. Here $N_i$ is the number density of the sub-population of impurity ions in excited state $i$ and $A_{i\rightarrow j}$ is

the Einstein "A" coefficient for the transition. To determine the emission coefficients for the transitions relevant to our measurements of iron, a strategy similar to that described in reference [94] is utilized. Assuming that the energy level balance for a particular impurity ion is in local equilibrium, the balance between its populating and depopulating mechanisms can be written as:

$$\frac{dN_{z,k}}{dt} = 0 \approx -N_{z,k} \sum_{i<k} A_{k\to i} + \sum_{i>k} N_{z,i} A_{i\to k} + N_{z+1} \langle \sigma_{z+1,gr\to k} v_{rel} \rangle N_0 \qquad (58)$$

Here, $k$ denotes an energy level of interest, $A$ represents the Einstein coefficients for transition between one energy level and another, and $N_{z,x}$ represents the number density of an ion with charge $z$ in energy level $x$. $\sigma_{z+1,cx\to k}$ is the cross-section for charge exchange electron capture between an ion with charge $z+1$ and a neutral which leaves the recombined ion in energy level $k$. $v_{rel}$ is the relative velocity of the impurity ion and the neutral and the angle brackets represent an integration over the velocity distribution. Finally, $N_0$ is the number density of the ground state neutral density for the main plasma species. The terms on the right-hand side of equation 58 correspond to (from left to right) depopulation via spontaneous decay to lower energy levels, population via spontaneous decay from higher energy levels, and population via charge exchange between a ground state impurity ion and a fuel neutral. Note that we neglect several terms in this energy level balance including collisional excitation and de-excitation as well as three body recombination which are very small for populating high-n states (see section 5.1 and figure 31). We also drop terms that would include contributions from radiative and dielectric recombination which are small for the electron temperatures considered here. Additionally, collisional ionization is not considered as it takes place on time scales much longer than those considered here for highly ionized impurities.

To solve equation 58, first one must determine the n-resolved cross sections for charge exchange into the various energy levels considered in equation 58. These can be determined from a universal cross-section scaling similar to what is performed in reference [94]. The universal scaling law assumes that the total cross sections are only a function of beam energy (the density and temperature dependence in these datasets is seen to be very weak), and can be scaled by a factor that depends on the impurity charge.

$$\sigma^*_{tot} = \sigma_{tot} \times z^{\alpha} \tag{59}$$

$$E^* = E \times z^{\beta} \tag{60}$$

Here, we collect a database of previously calculated CX cross sectional datasets which are plotted in figure 44. Previous studies have found that values of $\alpha = 1.05$ and $\beta = 0.3$ group the ADAS cross sections in a way that is well described by the following functional form [94]:

$$\sigma^*_{tot} = \frac{A log_{10}\left(\frac{B}{E^*}\right)}{1 + CE^* + DE^{*2} + FE^{*3} + GE^{*4}} \tag{61}$$

Where $A$, $B$, $C$, $D$, $F$ and $G$ are tunable parameters. The re-scaled cross sections as a function of the re-scaled energy are shown in figure 44 with the fitted functional form shown with a solid black line. The fitted values for the various parameters are $A = 3.43 \times 10^{-16}$, $B = 6.46 \times 10^{2}$, $C = 10^{-10}$, $D = 4.14 \times 10^{-5}$, $F = 1.10 \times 10^{-5}$, and $G = 10^{-20}$.

With the total cross section universal scaling validated, a beam energy of interest can be considered for the desired impurity. For example, to calculate the cross sections for an impurity ion with $z = 22$ and a beam energy of E = $50keV/amu$, we would determine $E^* = 50 \times 22^{-0.3} = 126.39$ keV/amu. Figure 44 only depicts the total

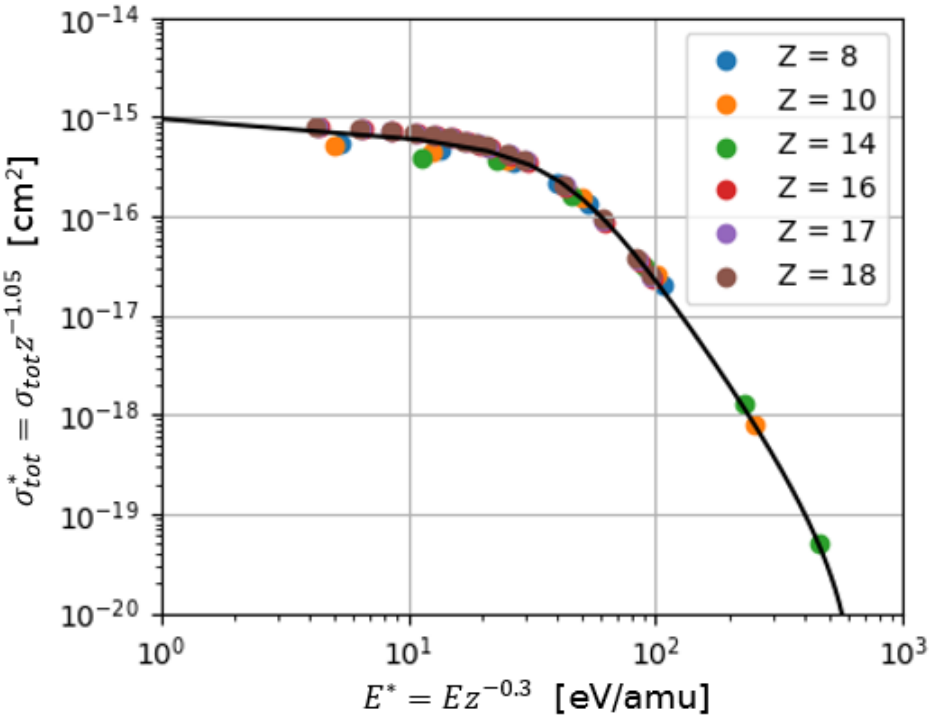


Figure 44: Re-scaled total charge exchange cross sections as a function of re-scaled beam energies.

cross section into all possible excited states. To determine the partial cross sections into the exact $n$ level of interest, a similar universal scaling approach is applied. The database of n-resolved CX cross-sectional datasets from ADAS are evaluated for a rescaled energy of interest. The cross sections and final $n$-states are then scaled by a factor that depends on z:

$$\sigma_n^* = \sigma_n \times z^{\delta} \tag{62}$$

$$n^* = n \times z^{\gamma} \tag{63}$$

To parametrize the universal scaling curve here, a piecewise cubic Hermite polynomial spline function is utilized where the knot locations and values are allowed to vary in the optimization procedure. For this step, the Markov Chain Monte Carlo approach is utilized which allows for determination of fitting uncertainties in the final cross

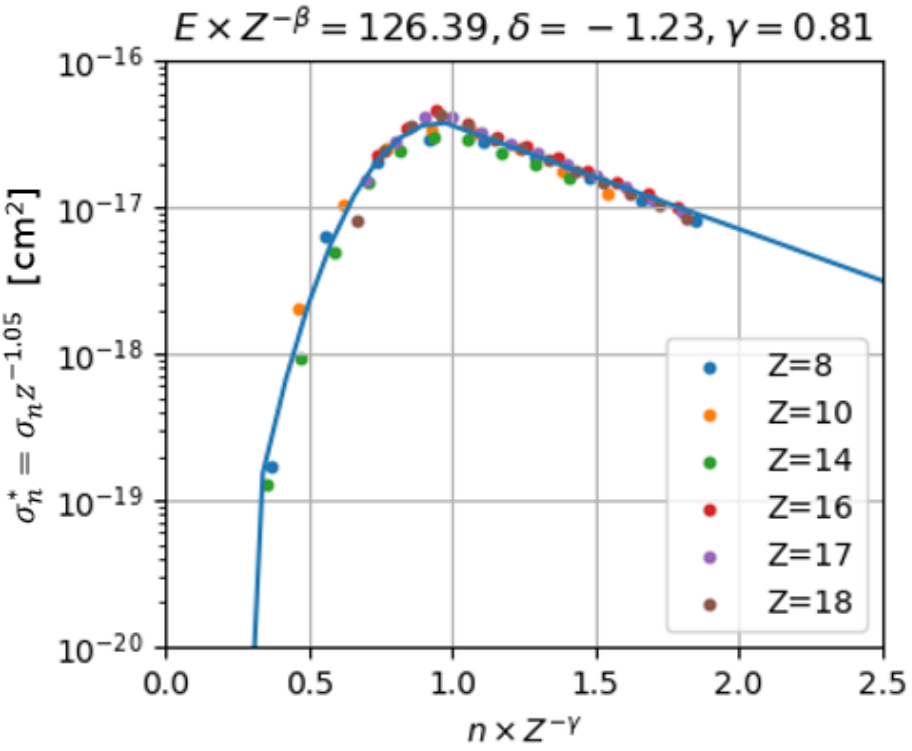


Figure 45: Re-scaled n-resolved charge exchange cross sections as a function of re-scaled n-level. The rescaled energy in this case is 126.39 keV/amu

sections. Here, the fitted values for $\delta$ and $\gamma$ are -1.23 and 0.81 respectively. The universal scaling results are then given in figure 45. Finally, to determine the partial cross sections necessary for equation 58, one can interpolate the necessary $n$ values onto the fitted function.

In addition to the partial cross sections, the Einstein A coefficients must be determined to allow for one to solve the matrix equation resulting from equation 58. For this, $n$ and $l$ resolved Einstein A coefficients can be calculated using the Autostructure code [95] which solves the wave-function using a Slater approach. This Fortran code is free to install online and performs its calculation in only a few seconds[96]. The user needs only to provide the valence electronic structure of the ground state ion, the net charge, and the number of energy levels it should calculate. Since the partial

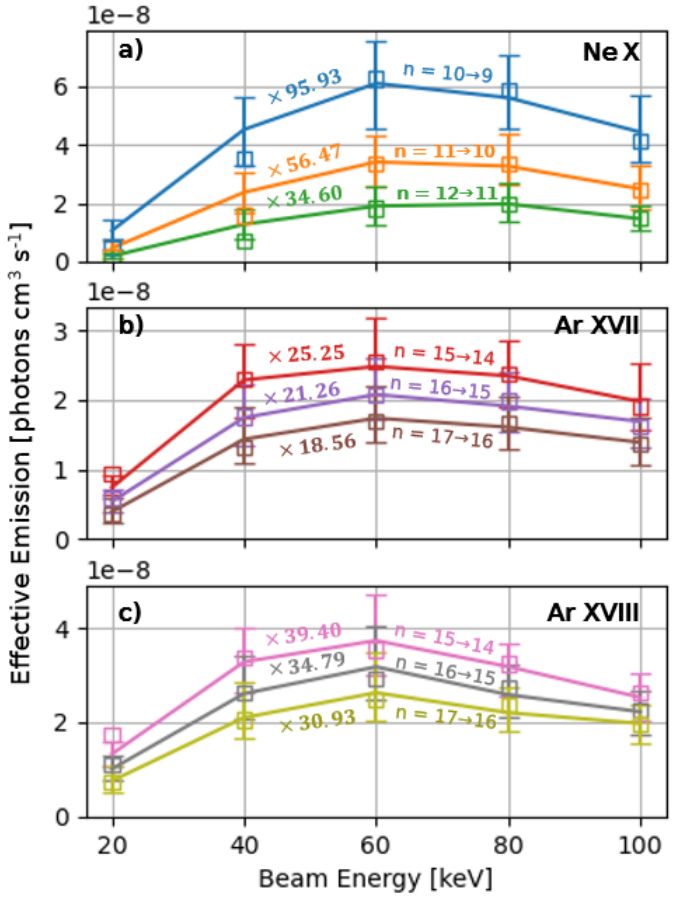


Figure 46: Calculated charge exchange effective emission coefficients for a) $Ne^{10+}$, b) $Ar^{17+}$, c) $Ar^{18+}$ plotted as a function of beam energy with error bars indicating fitting uncertainty. Each set of calculated data must be multiplied by a scaling factor (annotated next to each set data) to match the coefficients from the corresponding ADAS ADF12 datasets (shown in hollow squares). Plotted ADAS adf12 data is taken from the following files: *qef93#h_ne10.dat*, *qef07#h_arf#ar17.dat*, *qef07#h_arf#ar18.dat*.

charge exchange cross sections are not resolved for the angular momentum quantum number $l$, we assume that the $nl$ states are collisionally redistributed such that they are populated in accordance with the states' statistical weight (which is a measure of that $nl$ states level of degeneracy). In this scenario, we can rewrite equation 58 in the following form:

$$\frac{dN_{z,n}}{dt} = 0 \approx -N_{z,n} \sum_{n'<n} \sum_{l'<n'} \sum_{l<n} A_{nl\rightarrow n'l'} W_{nl} + \sum_{n'<n} N_{z,n'} \sum_{l'<n'} \sum_{l<n} A_{n'l'\rightarrow nl} W_{n'l'} + N_{z+1,gr} \langle \sigma_{z+1,gr\rightarrow n} v_{rel} \rangle N_0 \quad (64)$$

Here, we define the relative weight as the statistical weight of a particular $nl$ level divided by the sum of all statistical weights with principle quantum number $n$:

$$W_{nl} = w_{nl} / \sum_{l'} w_{nl'} \quad (65)$$

Since each of the $n$ level populations are coupled via equation 64, one can write out a matrix equation that describes the steady state balance of each $n$ level. The effective emission coefficients that appear in equation 57 for the transition between states $n_1 \rightarrow n_2$ are then:

$$\varepsilon_{n_1\rightarrow n_2} = \frac{N_{z,n_1}}{N_{z+1,gr} N_0} \sum_{l_2<n_2} \sum_{l_1<n_1} A_{n_1 l_1\rightarrow n_2 l_2} W_{n_1 l_1} \quad (66)$$

which can be evaluated by inverting the matrix generated by equation 64. Since the only populating terms we consider are the CX cross section and the cascade from higher energy levels, the matrix is upper triangular allowing for it to be solved trivially using the python numpy library. Final uncertainties in the effective emission coefficients are propagated from the fitting uncertainty in the CX cross sections using an approach similar to that described in section 6.1.6. The most time consuming step in the calculation of these effective emission coefficients is the universal cross section scaling extrapolation which, in order to converge to a best fit with well resolved uncertainties, takes $\sim 1$ hour.

Bench-marking results showing the comparison of effective emission coefficients calculated using this method and those available on OPEN ADAS are given in figure 46 for a range of beam energies representative of the energy ranges used in most experiments. The values found on the ADAS database are given by the hollow squares while those calculated using our presented method are shown by the lines with overlaid error bars. Note that the energy dependence for each transition matches the ADAS datasets very well while a scaling factor must be introduced to match the magnitude. This scaling factor along with labels indicating the transition energy levels are annotated next to the corresponding plotted data. This level of uncertainty in the effective emission coefficient magnitude is not unexpected. For example, figure 43 shows emission coefficients that are offset by 2 orders of magnitude depending on the utilized cross sectional dataset. To perform a more robust benchmarking, one would need to run the ADAS 308 code using the same input datasets as utilized here. For this work however, since we consider the relative magnitudes between given lines of sight, only the energy dependence is necessary to characterize the ratio between the emission coefficients for the first and second beam energy component.

The calculated effective emission coefficients used in the modeling of the Fe XXII and Fe XXIV signals are then given in figure 47 as a function of the beam energy. Additionally, a single ADAS calculation was acquired for the Fe XXIV transition (file: *qef07#h_arf#fe24.dat*) which is additionally plotted next to the newly calculated emission coefficients. Again, the calculated datasets are scaled up to easily compare the energy dependence to the existing data.

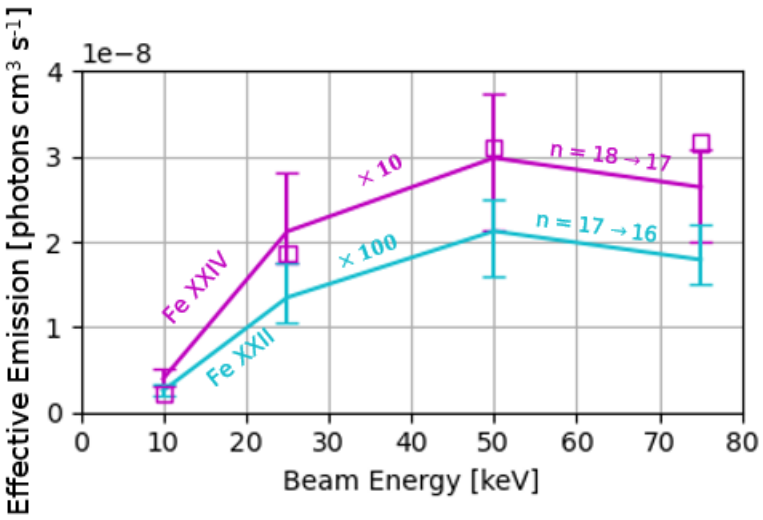


Figure 47: Effective emission coefficients calculated for $Fe^{22+}$ and $Fe^{24+}$ for the transitions observed in W7-X experiments. The data shown in hollow squares has been calculated previously using the ADAS code suite for $Fe^{24+}$.

# 7 Experimental Results

## 7.1 Description of Discharge #20230314.26

The most recent operational phase (OP 2.1) at W7-X occurred from December 2022 - April 2023. Data of varied quality was collected during the entire campaign however, the first several months required time for commissioning of the system. This constraint, along with the availability of kinetic profiles and supplementary diagnostics, led to a small number of high-quality datasets. One representative experiment (shot 20230314.26) will be discussed in detail in the remainder of this section.

An overview plot of the experimental program #20230314.26 is given in figure 48. In the top panel, the applied ECRH power is given (blue) along with an estimate of the total radiated power (red). The second panel shows the core electron density (green) as well as the line integrated density (blue). Panel three summarizes the core electron temperature as calculated by Thomson scattering (blue) and ECE (green).

Shortly before the iron LBO injection at t = 22.5 s, continuous NBI is introduced allowing for CXRS measurements.

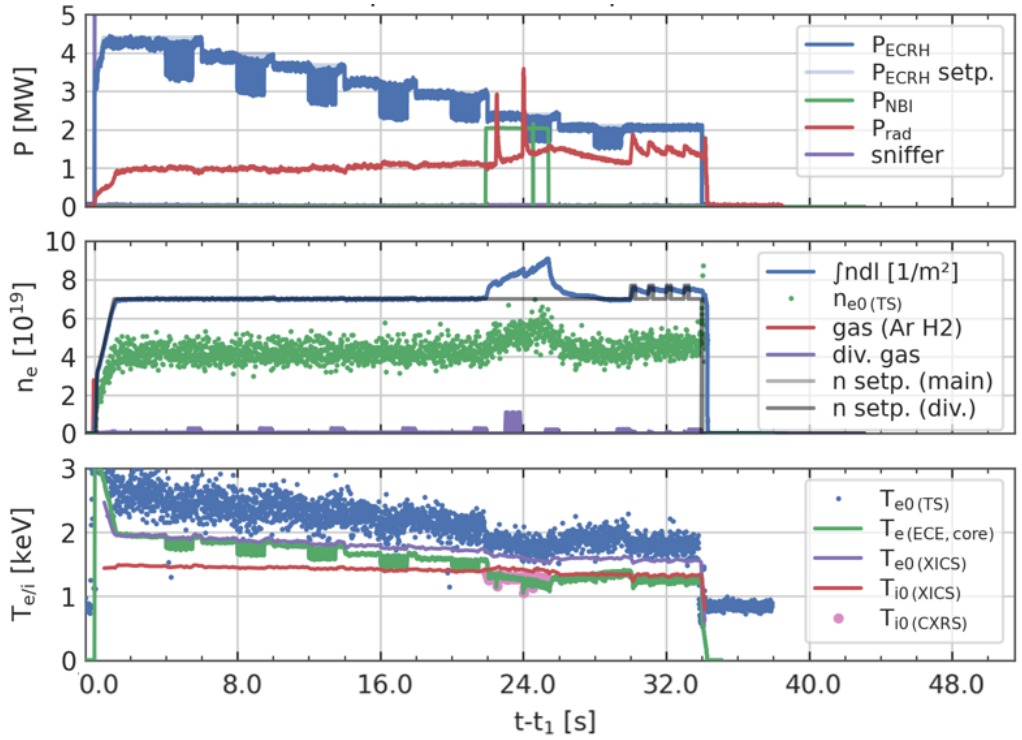


Figure 48: Overview of experiment 20230314.26. ECRH power and radiated power are shown in the top panel, electron densities are shown in the middle panel, and electron temperatures are shown in the botom panel. The iron injection takes place at 22.5 s.

Thomson scattering data is available which measures the electron temperature and density during the LBO injection at a discrete set of radial points. With this dataset, outboard measurements are used to fit an analytical function to the electron temperature and density data using an Markov Chain Monte Carlo (MCMC) method (see section 6.1.2 for description). Using this method, the median profile and one sigma confidence intervals can be determined. Additionally, the main ion temperature profiles are determined via CXRS measurements. Again, individual localized measurements are used to fit an analytical function to the data with uncertainties

determined by the MCMC method. These fitted kinetic profiles are given in figure 49.

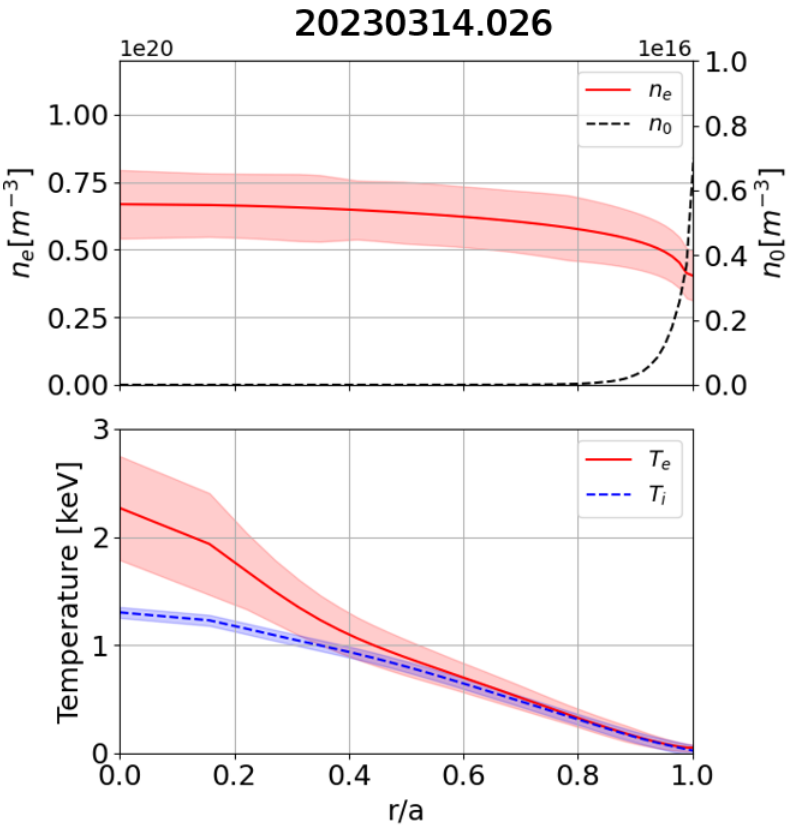


Figure 49: Electron density, electron temperature, and ion temperature along with neutral density profiles calculated using pyfidasim. Experimental profile data is collected at the time of the LBO injection ($t$ = 22.5 s). Uncertainties are given by shaded regions around the fitted profiles.

Several diagnostics measure the radiation from the impurity species after they have been injected into the plasma via the LBO method. The first system we consider is the HEXOS diagnostic; however, for the OP 2.1 campaign, standard use of the system was not available due to damage on two of the four MCP detectors. Despite this, several previously unreported lines can be observed in the wavelength range of 2.5 - 10.7 nm. A selection of these lines are highlighted in figure 50 and likely candidates for the observed line transitions are given in table 2 with wavelengths and Einstein

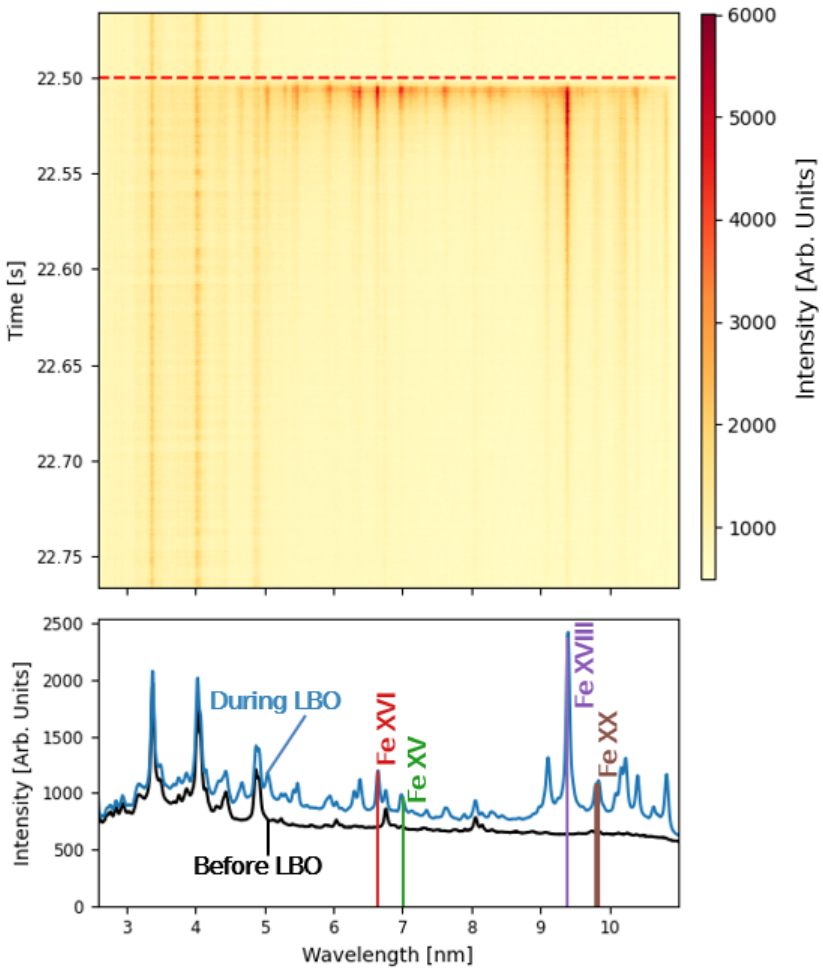


Figure 50: Top: Raw HEXOS signal from shot 20230314.26 depicting presence of X-Ray emission following LBO injection. Bottom: Time averaged spectra before and during the LBO event.

| Ion | $\lambda$ [nm] | Upper Level | Lower Level | $A_{ki}$ |
|---|---|---|---|---|
| Fe XV | 7.0054 | $3s3f(^3F_4)$ | $3s3d(^3D_3)$ | 8.80e+11 |
| Fe XVI | 6.6356 | $2p^64f(^2F_{7/2})$ | $2p^63d(^2D_{5/2})$ | 1.00e+12 |
| Fe XVIII | 9.3926 | $2s2p^6(^2S_{1/2})$ | $2s^22p^5(^2P_{3/2})$ | 9.13e+10 |
| Fe XX | 9.8075 | $2p^5(^2P_{1/2})$ | $2s2p^4(^2D_{3/2})$ | 4.62e+10 |
| Fe XX | 9.8358 | $2s2p^4(^2P_{1/2})$ | $2s^22p^3(^2P_{3/2})$ | 9.6e+10 |

Table 2: Wavelengths, Einstein Coefficients, and energy level terms consistent with the line transitions observed in the HEXOS spectrum following LBO. The two lines from the $Fe^{19+}$ charge state are close enough together that line blending is expected.

coefficients tabulated by the NIST database [70]. As an additional check, the temporal

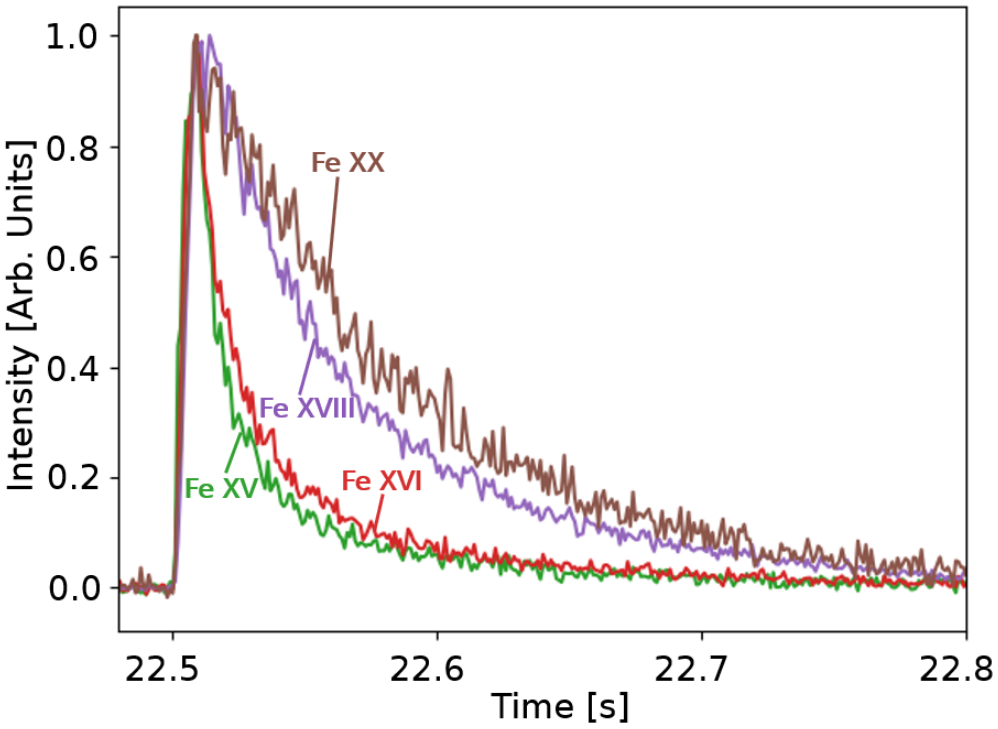


Figure 51: Time traces of emission from the four charge states identified in figure 50 for the impurity injection considered during experiment #20230314.26. Line emission decay times tend to increase as charge state increases.

evolution of each of these lines is plotted in figure 51. One can see an increased decay time for emission from higher charge states, consistent with the picture that lower charge states more quickly depopulate due to ionization. For forward modeling of HEXOS lines, a database of emission rates for all relevant lines in the wavelength range of interest is available for every charge state of Iron. While the lines shown in figure 50 can be mostly tied to specific line transitions, the synthetic signal is determined by summing contributions from all charge states and all line transitions within a wavelength range of 0.1 nm centered around the observed wavelength. For the inference framework described in this work, the Fe XVI and Fe XVIII lines were chosen due to their superior signal to noise ratio.

Finally, bolometer measurements are collected following the impurity injection which, using the tomographic inversion technique, provide time traces of the volume integrated radiated power inside of the LCFS with a frame rate of 600 Hz. Additionally, measurements of the radiated power fractions inside $r/a = 0.85$ and $r/a = 0.5$ are available with 15 Hz time resolution. To isolate the impurity signal specifically, the average radiated power prior to the injection is subtracted from the time traces. Uncertainties are assumed to be $\sim$ 15% prior to background subtraction. A time trace of the total volume integrated radiated power along with the radiation fractions measured during the impurity injection is given in figure 52. Here, $t = 0$ is defined to be at the time of injection.

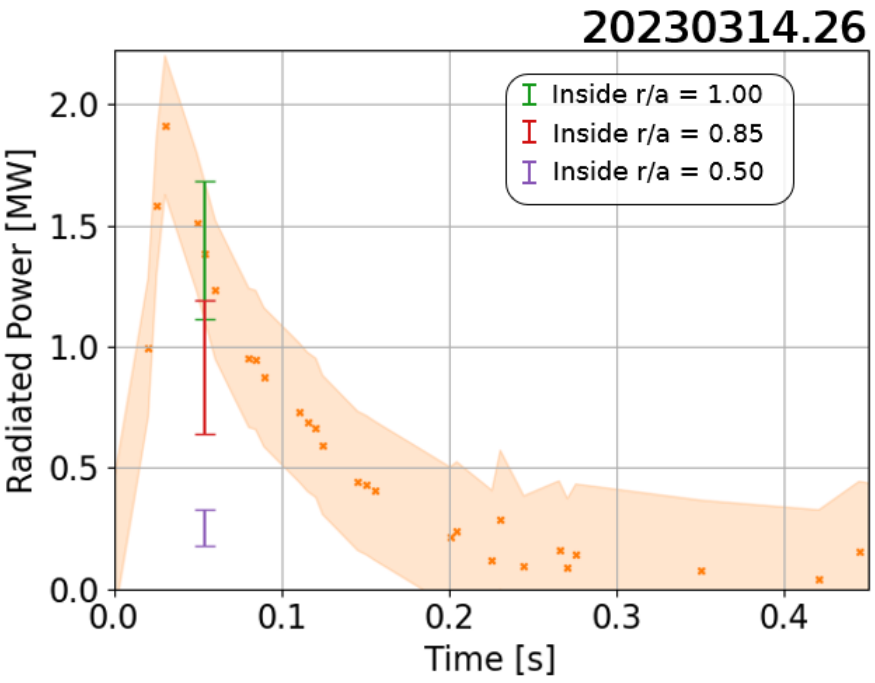


Figure 52: Total radiated power inside of $r/a = 1.0$ shown with orange x's and uncertainty depicted with shaded orange. Radiation fraction measurements are shown during the impurity injection with the error-bars for radiation inside of $r/a = 1.0$, 0.85, and 0.5.

## 7.2 Inference of Impurity Transport

### 7.2.1 Normalized and Relatively Calibrated CXRS Signals

Bayesian inference allows one to directly evaluate the improvement in inference uncertainty by self consistently including multiple diagnostic measurements in the user-defined statistical model. This is accomplished by using the "emcee" Markov Chain Monte Carlo sampler with 48 "walkers". Each inference is run until the number of steps taken is more than 25 times the calculated autocorrelation time. This typically takes 50,000 - 100,000 iterations and requires $\sim 10-20$ hours per inference when run on a desktop computer. All but the last 1000 steps are then discarded as so-called "burn in" samples such that the final sample population has 48,000 independent samples of the posterior distribution.

We start by considering the inference results from matching the CXRS signals on their own. Here we consider two inference cases. The first is where signals from each line of sight are normalized to one, which reflects the lack of knowledge of the emission coefficients and therefore the local impurity densities. Next, the effective emission coefficients determined in section 6.2.3.1 are utilized allowing one to take advantage of the relative intensity calibration between the lines of sight.The fitted CXRS signals are given in figure 53 and 54 for the case of the normalized CXRS and relatively calibrated CXRS signals respectively. Here, the Fe XXII and Fe XXIV charge exchange lines are considered in the inference.

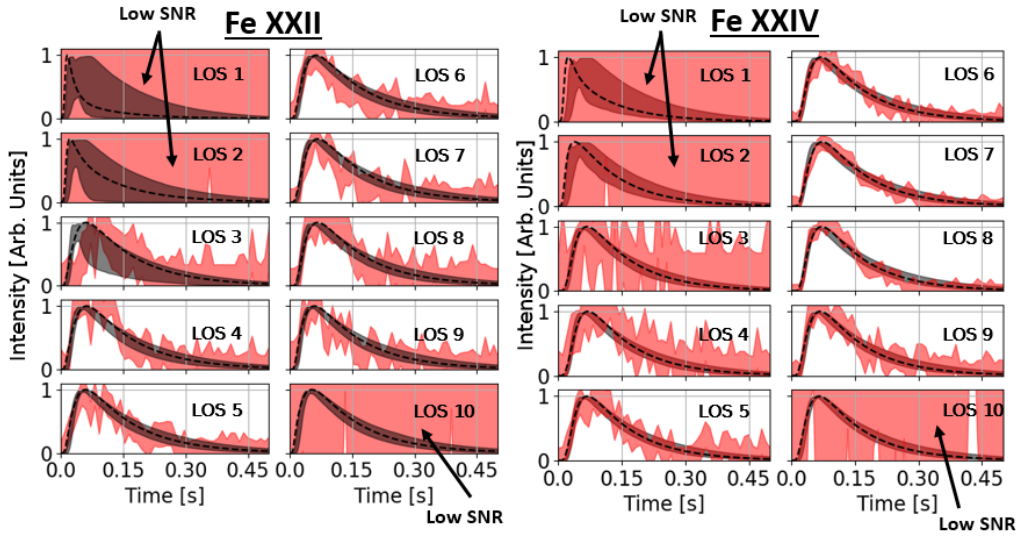


Figure 53: Synthetic signals matched to CXRS data that has been normalized to 1. Experimental uncertainty is given by shaded red with fitting uncertainty shown in shaded grey. The dashed black lines indicate the forward model from the posterior sample with the highest probability. Data from discharge 20230314.26

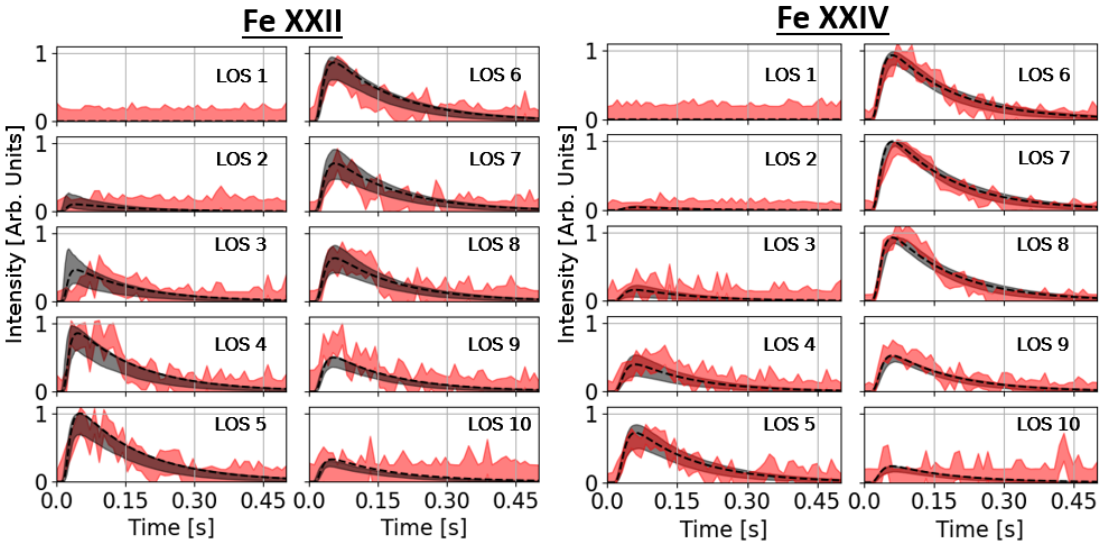


Figure 54: Synthetic signals matched to CXRS data that has been normalized to the brightest signal. Experimental uncertainty is given by shaded red with fitting uncertainty shown in shaded grey. Forward modeled signals utilized the effective emission coefficients derived in section 6.2.3.1. The dashed black lines indicate the forward model from the posterior sample with the highest probability. Data from discharge 20230314.26

Upon initial inspection one can see the sharp increase in emission followed by an exponential decay as the impurities leave the plasma. Additionally, the emission strengths are strongest nearer the core with the Fe XXIV emission strengths exhibiting a noticeable shift towards the core compared to the Fe XXII emission. This is consistent with the expected ionization balance for iron since the hotter core will more readily ionize the impurities. For most channels, we achieve excellent agreement for not only the decay, but also the impurity rise times and the relative intensities. For line of sight 3, the temporal behavior is not reproduced perfectly for the Fe XXII emission. One potential explanation is that this effect is not captured by the model due to the assumption of time-independent kinetic profiles. Core and mid-radius electron cyclotron emission (ECE) measurements indicate that there is a brief period of $\sim 40\%$ reduction in the electron temperature before the profile recovers $\sim$ 10ms later. During this period, temperatures at the locations of the active emissions seen by the inner lines of sight may still be sufficiently high that ionization up to the $Fe^{22+}$ charge state is fast. Line of sight 3 however, views local emission from a location in the plasma where the electron temperature is $\sim$ 800 eV. This temperature range is close to the left edge seen in figure 35 associated with a sharp drop-off in the ionization rate. Additionally, there is some disagreement in the fitted intensity for line of sight 9 which can be attributed to known overestimation of the beam attenuation by pyFIDASIM at the inboard side of W7-X[59].

A comparison of the inferred impurity diffusion and peaking ratio profiles is given in figure 55. Note the significant improvement in fitting uncertainty, particularly for the peaking ratio, when considering the relative calibration of the CXRS signals. In the case where the CXRS signals are each normalized to one, the lack of information on the impurity peaking is reflected in the very large uncertainties in the inferred peaking ratio. In contrast, introducing the relative calibration between lines of sight

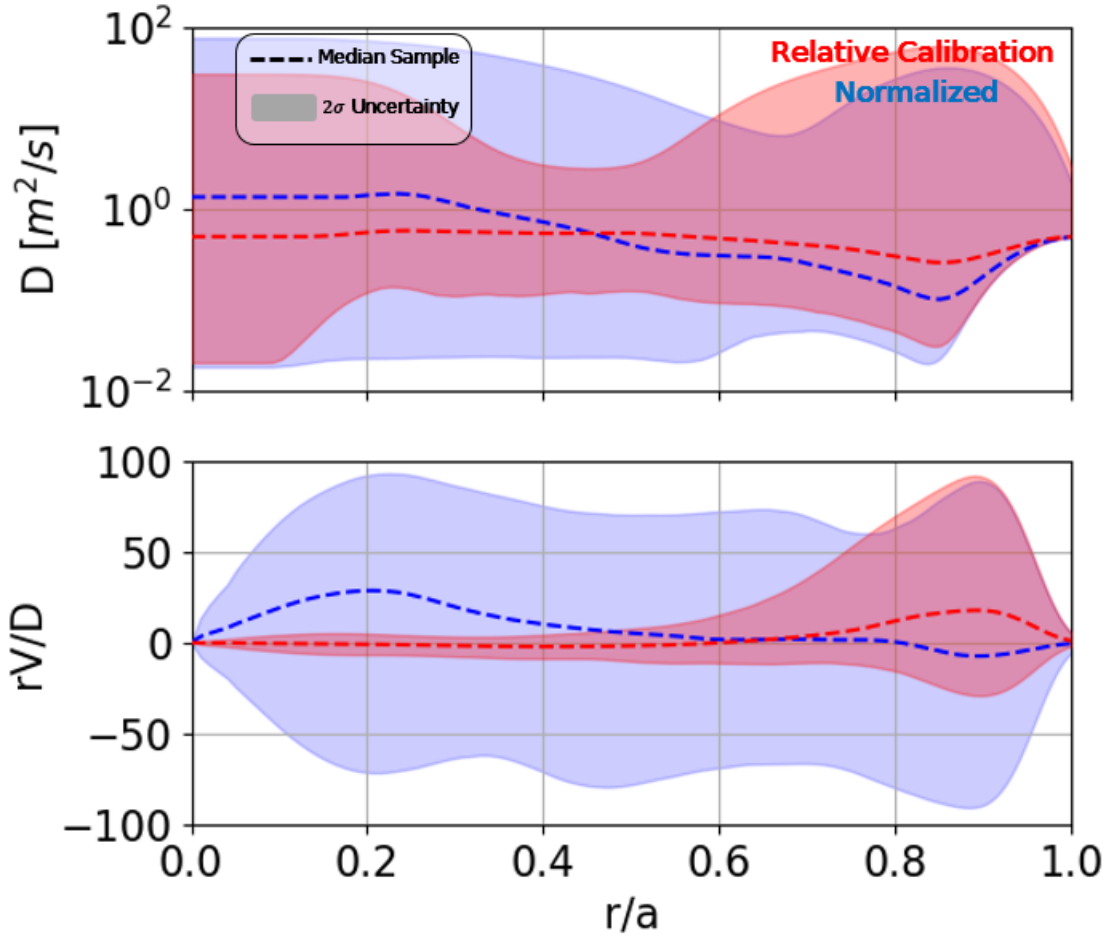


Figure 55: Inferred impurity diffusion and peaking ratio profiles for the case of fitting CXRS signals normalized to 1 (blue) and normalized to the brightest signal (red). $\pm 2\sigma$ uncertainties are shown with the shaded regions with the median profiles shown with the dashed lines.

to the inference scheme adds a constraint on the impurity density shapes and therefore the impurity peaking ratio. The significant improvement in the peaking ratio fitting uncertainty indicates that the method of analyzing calibrated high-n Rydberg emissions is well suited to the problem of simultaneously inferring the impurity D and V profiles.

### 7.2.2 HEXOS Measurements

In addition to the CXRS signals, multiple other diagnostics can be included in the inference framework to improve fitting uncertainty. First, we consider the inclusion of the HEXOS signals. For the forward model, the local emission is determined at each point along the HEXOS line of sight and is line integrated. The path of this line integral can be used to determine the $r/a$ values along its length which can be used to translate to the pySTRAHL radial grid. The forward modeled HEXOS signal can then be described by the integration over the full path of the HEXOS line of sight:

$$\varepsilon_{z,\lambda}(t) \sim \int n_z(\vec{x},t) n_e(\vec{x}) \alpha_{z,\lambda}\left(T_e(\vec{x}), n_e(\vec{x})\right) dl \ . \tag{67}$$

Here, $n_z$, $n_e$, and $T_e$ represent the local impurity density of charge state $z$ (as calculated by pySTRAHL), the electron density, and the electron temperature at a point in space along the line of sight, $\vec{x}$. As is the case for the main pySTRAHL calculation, the background kinetic profiles are assumed to be constant. $\alpha_{z,lambda}$ is the local photo-emission coefficient (PEC) for charge state $z$ which undergoes a line transition with wavelength $\lambda$ and is a function of the local electron temperature and density. These PECs are tabulated and available for many impurity species on the OPEN ADAS database (adf 15 format). Note here that since intensity calibrations are not available for the HEXOS emissions, measured and modeled signals are normalized to a maximum value of 1

Figure 56 shows comparison between the fitted synthetic and measured Fe line emissions seen by the HEXOS system when fitting both the relatively calibrated CXRS and HEXOS signals. Additionally, figure 57 shows a comparison between the fitted impurity D & rV/D profiles for the case of just fitting the HEXOS signals, just fitting the CXRS signals, and fitting both simultaneously. While the improvement in

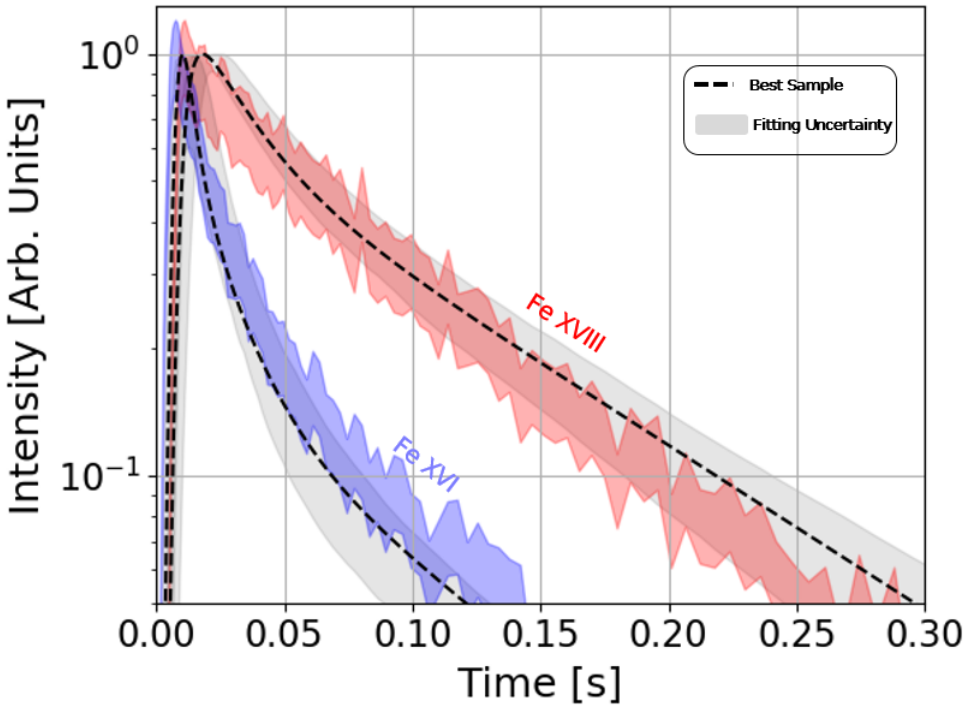


Figure 56: Fitted Fe XVI and Fe XVIII signals when fitted alongside relatively calibrated CXRS signals. The dashed black lines indicate the forward model from the posterior sample with the highest probability. Experimental uncertainty is given by the shaded region with fitting uncertainty given by the shaded gray.

fitting uncertainty for the diffusion profile is minimal, it is interesting to note that the most significant improvement in the peaking ratio profile occurs in the outer region of the plasma where the $Fe^{15+}$ and $Fe^{17+}$ charge states are expected to dominate the charge state balance (see fig. 35). This can be explained since the outermost line of sight for which the CXRS signals can be observed (LOS 3) views at $r/a \sim 0.5$ By including the HEXOS signals, valuable constraints on the region outside $r/a = 0.5$ are introduced.

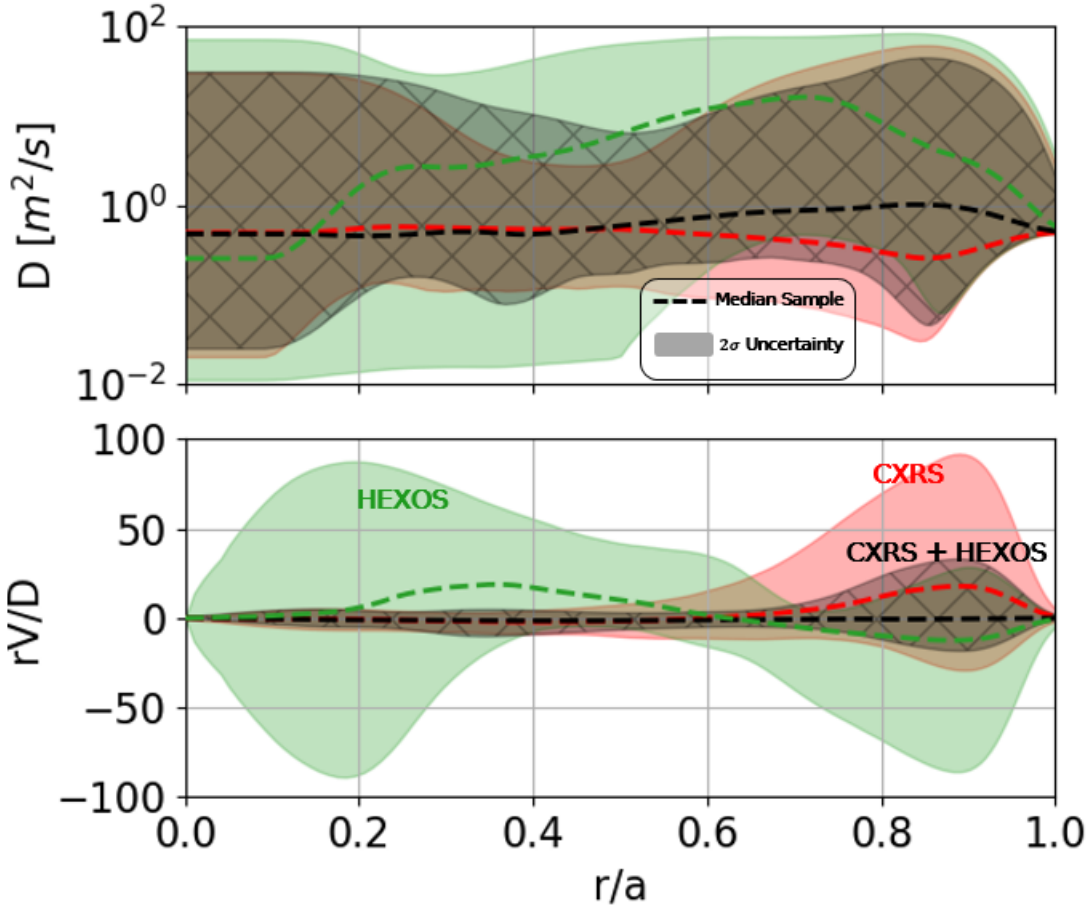


Figure 57: Inferred impurity diffusion and peaking ratio profiles for the case of fitting relatively calibrated CXRS signals (red), HEXOS signals (green), and both simultaneously (black hatched).

### 7.2.3 Bolometer Measurements

The bolometer measurements utilized in this work are the result of a tomographic inversion such that a measure of the total radiation contained inside of the LCFS is available. This method also allows for the determination of the total radiated power inside of $r/a = 0.85$ and $r/a = 0.5$. Additionally, the diagnostic is designed to be particularly sensitive to wavelengths in the X-ray to VUV range such that the measured signals are representative of the total impurity radiation[65]. To simulate the total radiated power from the impurity species, ADAS cooling rate coefficients[16]

are utilized alongside the pySTRAHL calculated impurity densities:

$$P(t) = \int_V \sum_z n_z\left(r_{eff}, t\right)\left(n_e(r_{eff})\left(PLT\left(T_e(r_{eff}), n_e(r_{eff})\right) + PRB\left(T_e(r_{eff}), n_e(r_{eff})\right) + \langle n_0\rangle(r_{eff}) PRC\left(T_e(r_{eff}), n_e(r_{eff})\right) dV \quad (68)$$

Here $PLT$, $PRB$, and $PRC$ indicate the effective radiated power coefficients for impact excitation, recombination, and charge exchange contributions respectively and are functions of the local electron temperature and density. $\langle n_0\rangle$ represents the flux surface averaged neutral density. $n_Z$ represents the impurity density for charge state $Z$ which is calculated via the pySTRAHL code. For increased computational speed, the volume integral is performed considering a simple torus with circular cross section described by the effective radius, $r_{eff}$. All values in equation 68 are assumed to have no dependence on poloidal or toroidal angle. This calculation has been compared to a more computationally intensive calculation of the radiated power which considers flux surface volumes based on a VMEC equilibrium. Differences in the calculated radiated power were found to be $\sim 1 - 2\%$. Note that since the modeled signals only consider radiation from the injected impurities, the background plasma radiation levels are subtracted from the experimental signals to isolate the response from the injection.

Figure 58 shows a comparison between the measured and modeled radiated power along with the radiation fractions inside $r/a = 0.85$ and $r/a = 0.5$. Figure 59 depicts the fitted D & rV/D profiles when considering only the CXRS signals, only the bolometer measurements, and a combination of the two. It is clearly seen that the inclusion of the bolometer signals in the inference framework have a strong effect on the uncertainty in the impurity transport. Specifically, the peaking ratio is constrained

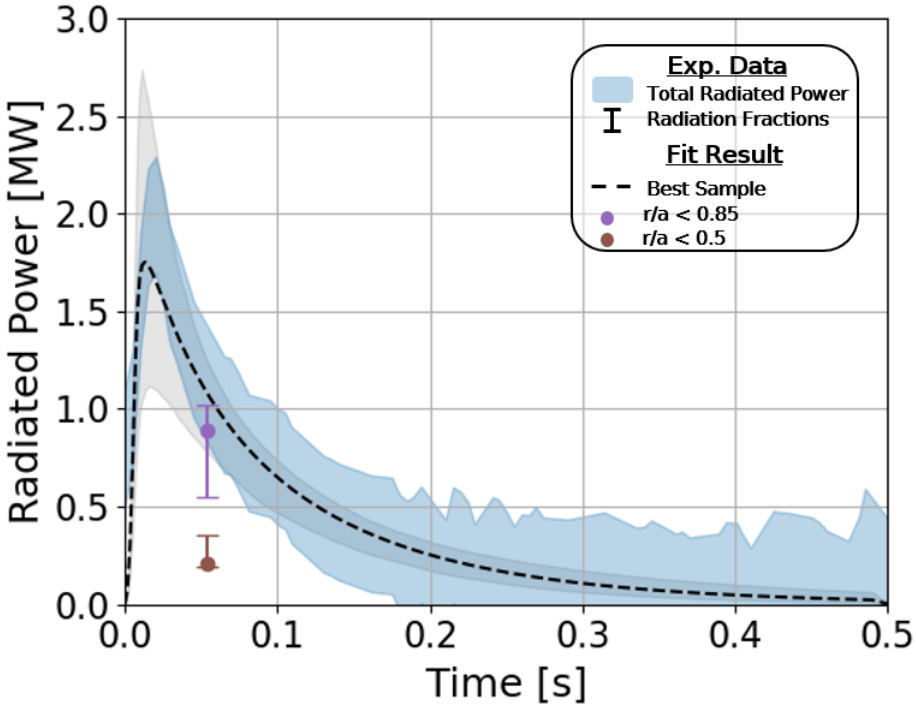


Figure 58: Fitted bolometer signal when fitted alongside relatively calibrated CXRS signals. The dashed black line and the circular markers indicate the forward model from the posterior sample with the highest probability.

to be well below ±10. Such a strong effect on the peaking ratio can be understood by the introduced constraint on the total impurity density profile. While the relatively calibrated CXRS measurements will provide insight to the profile shape for the $Fe^{21+}$ and $Fe^{23+}$ states individually, the bolometer signal is sensitive to emission from all charge states. Hence, the inclusion of the bolometer radiation fraction measurements provide a more robust metric for the overall impurity density profile.

### 7.2.4 Inclusion of All Diagnostics

Considering the benefits of adding the HEXOS and Bolometer data, figure 60 shows the resulting D, rV/D, and V profiles when including all three diagnostics in the inference framework simultaneously. Also shown are the ion root neoclassical diffusion

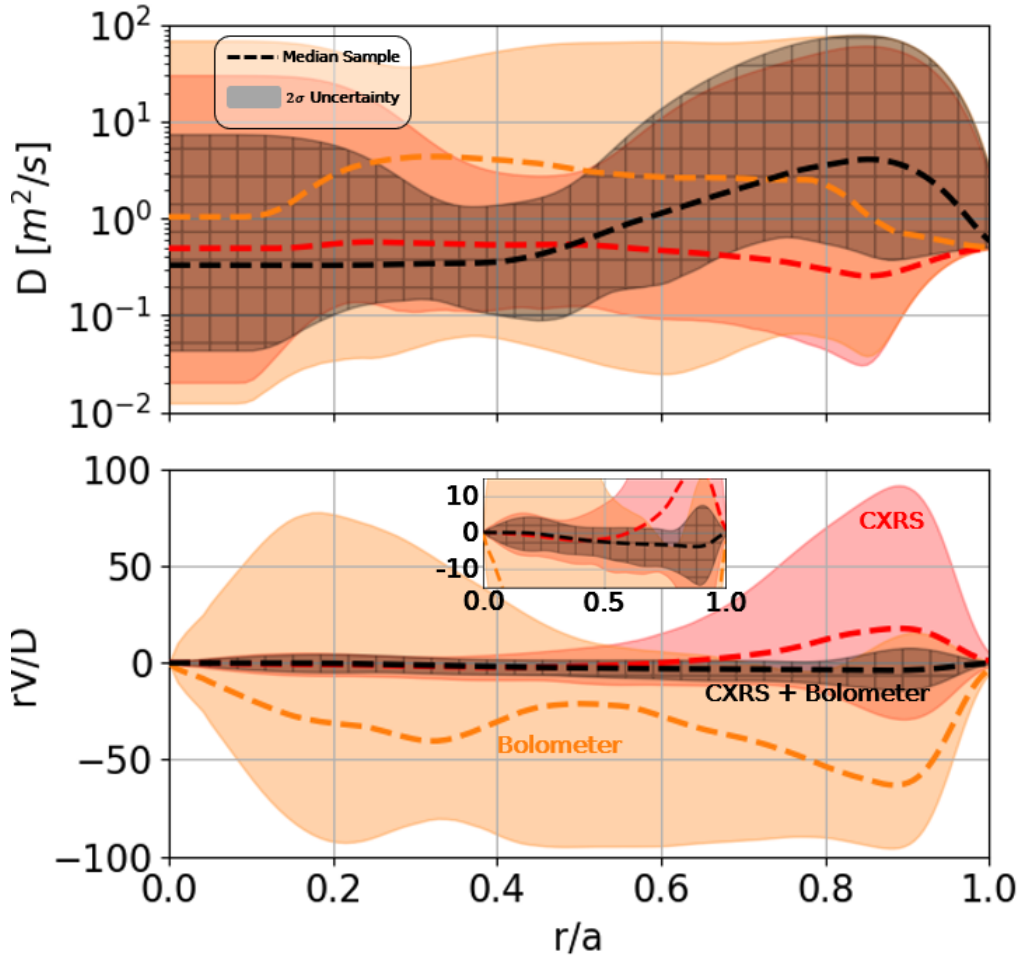


Figure 59: Inferred impurity diffusion and peaking ratio profiles for the case of fitting relatively calibrated CXRS signals (red), bolometer signals (cyan), and both simultaneously (black hatched).

and convection for the $Fe^{23+}$ charge state as calculated by the DKES code[97]. Note also, the experimentally measured radial electric field which has been acquired via analysis of the doppler shifted carbon emission seen by the ILS spectrometer. These results indicate that the impurity transport is significantly larger than the neoclassical expectation for highly ionized iron. Additionally, the turbulence seems to have a strong effect on the convection velocity near the edge region where an inward pinch is observed. Note that this observation is consistent with the expectation for ITG

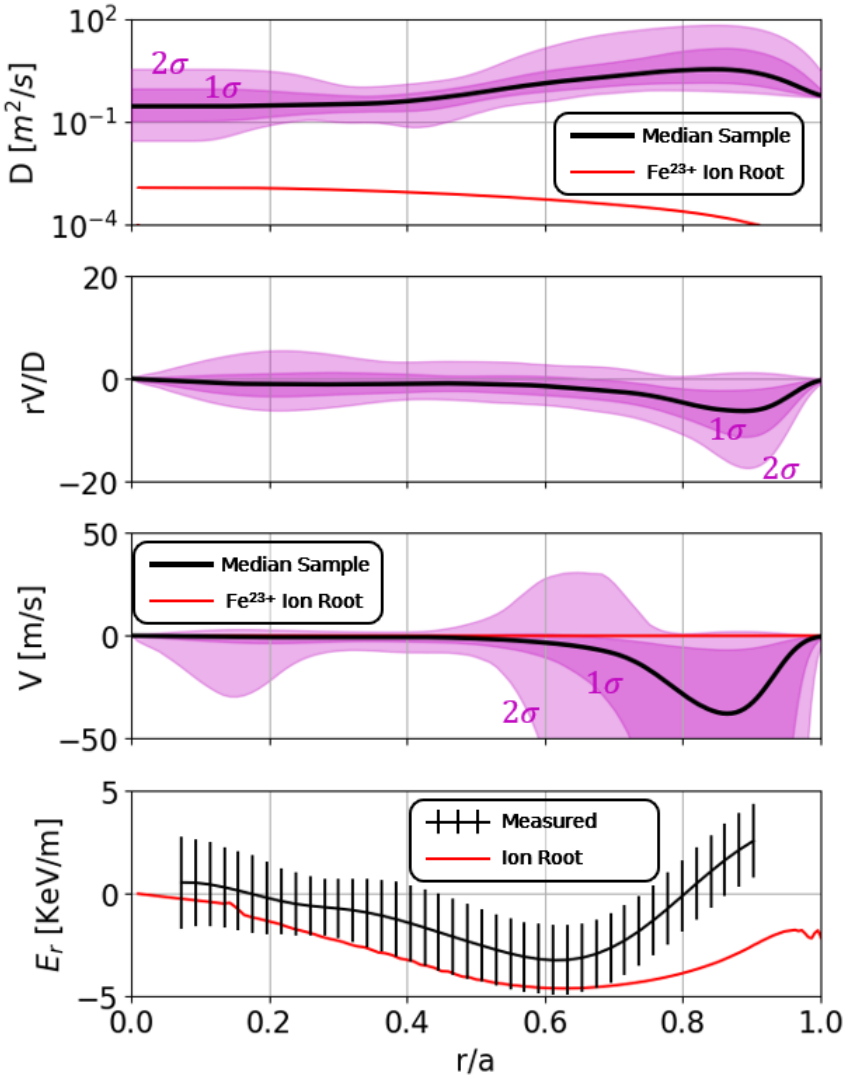


Figure 60: Inferred impurity diffusion and peaking ratio profiles for the case of fitting of CXRS, HEXOS, and bolometer signals simultaneously.

turbulence as predicted in figure 9 [98, 24].

One final measurement which is relevant to the impurity transport is the steady state intrinsic carbon density. The $C^{6+}$ profile can be determined via analysis of data from the ILS spectrometer [59]. The carbon density profile can be forward modeled in pySTRAHL by assuming the same model used for the iron injection simulations with continuous sourcing rather than a short injection. The simulation

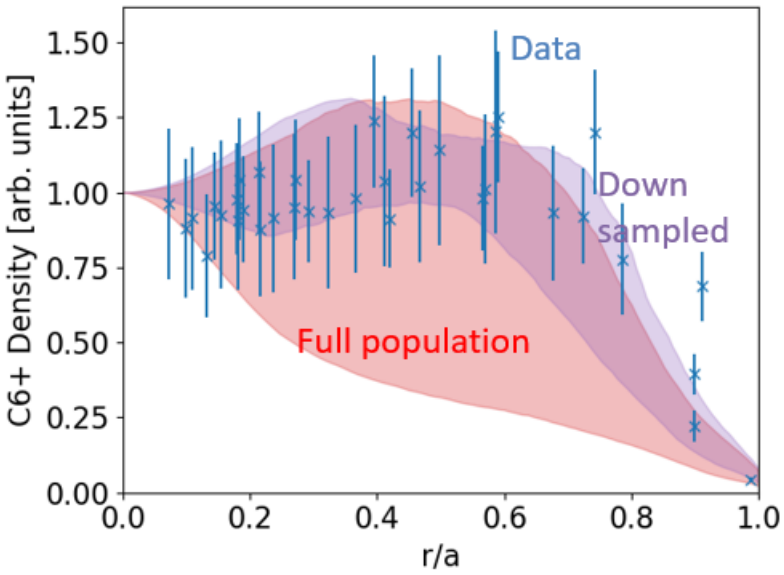


Figure 61: Measured C6+ density profile (blue error bars) plotted alongside $1\sigma$ uncertainty bands for forward modeled steady state carbon densities. Carbon density profiles are calculated for the distribution of possible transport profiles given in figure 60. The bands shown in red correspond to the full population of possible transport profiles while the shaded violet bands are down-sampled to isolate only samples which agree with measurement

is run for enough time steps to reach a steady state solution and the normalized $C^{6+}$ densities can be compared to measurement. The resulting $1\sigma$ bounds on the forward modeled, normalized carbon density is shown shaded red in figure 61. It can be seen that a large number of model samples do not agree well with the carbon density measurements. We can, however, down-sample the model samples to only consider the sub-population that agrees well with the carbon density measurements (shown in shaded violet). The corresponding down-sampled transport profiles are shown in figure 62. Note that this sub-population of inference results differs mainly in the impurity convection in the core. While the full population of parameter samples does not rule out the possibility of an inward pinch in the core, only the samples with approximately zero core convection can explain the carbon data. This agrees with

expectation since an inward pinch in the core would cause peaking of the $C^{6+}$ density.

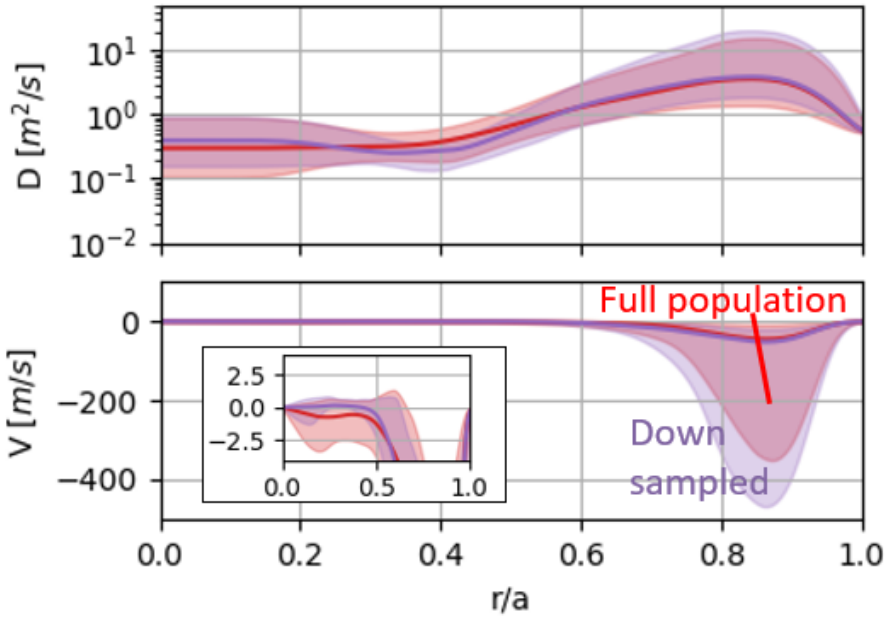


Figure 62: The median and $1\sigma$ error bands when considering full population of possible transport profiles (red, identical to those shown in figure 60) and when down-sampling to isolate those that agree with measured carbon densities (violet). An exploded view of the convection velocity zoomed into $\pm 3$ m/s is shown to depict the effect down-sampling has on the sample population in the core.

Finally, since the bolometer measurements give a strong constraint on the total number of impurities in the confined region and an absolute intensity calibration is available for the CXRS measurements, the magnitude of the effective emission coefficients calculated in section 6.2.3.1 can be determined. This can be accomplished by considering two additional free parameters in the Bayesian inference. These scale the Fe XXII and Fe XXIV emission coefficients respectively. The final inferred emission coefficients are shown in figure 63 alongside datasets available from adf12 files. These inferred effective emission coefficients are indicated by hollow diamonds with fitting uncertainty given by the error bars. Note that the single adf12 dataset available for Fe XXIV emission is in agreement with the inferred value. Other than this single

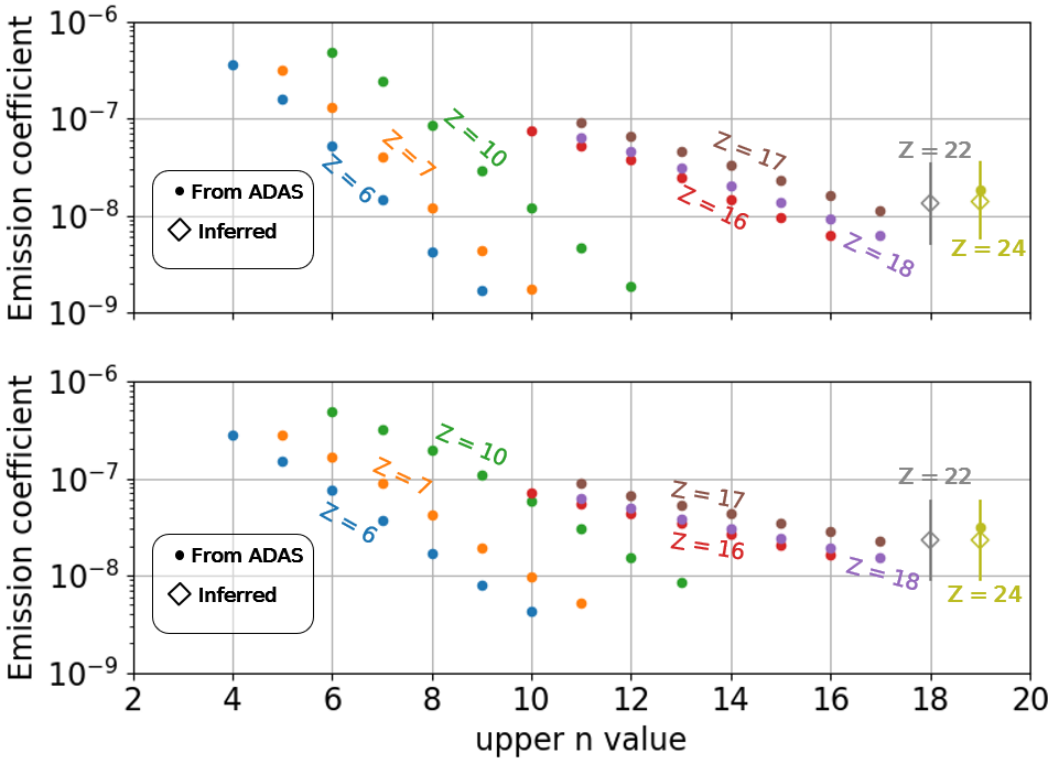


Figure 63: Tabulated and inferred effective emission coefficients for a variety of charge states and transitions. Data available via adf12 files is given with filled circles while the inferred values are given with hollow diamonds. Additionally shown is the $1\sigma$ uncertainty in the inferred magnitudes.

data point, only a qualitative comparison can be made indicating that the emission coefficients are of reasonable order of magnitude. It could be of great interest to perform future validation studies which apply this technique to impurities which have emission data readily available.

# 8 Conclusions

## 8.1 Summary of Results

The focus of the work presented here has been to investigate the transport of heavy impurities in the W7-X stellarator.

Five Czerny-Turner style spectrometers were installed at W7-X for use during the OP2.1 campaign. This system provided ten spatial channels which were designed to view active impurity emission along the neutral heating beam. Each spectrometer was built in order to provide excellent photon throughput and enable observation of line radiation from impurities at 1kHz. Several high quality datasets were collected during the campaign providing measurements of both injected iron and tungsten. Observed in the collected spectra, were high-n Rydberg emissions from charge exchange between the neutral beam and the injected impurities. Analysis of these emissions provides a novel way to directly measure the local impurity densities in experiments at W7-X enabling advanced impurity transport studies. These emissions were found to be agnostic to the particular injected impurity making their observation a flexible technique that can be applied to a wide range of impurity species. Additionally, experiments indicated that for highly ionized impurity ions, the only mechanism for populating the high-n Rydberg states is CX with the neutral beam. This means that their emissions lack a passive component.

To simulate the 1D transport of impurities, the pySTRAHL code has been developed. The python implementation has enabled its use in tandem with a variety of python libraries and other simulation codes. Moreover, the acceleration of this code via the numba package has allowed for pySTRAHL calculations to be performed quickly enough to be embedded into a Markov-Chain Monte Carlo inference framework. This code base has been adapted for use in W7-X as well as several other

devices including HSX, DIII-D, and Pegasus. With many current users, pySTRAHL will continue to be useful for future research studies.

Since effective emission coefficients were unavailable for the measured impurity line transitions, a simplified collisional radiative model was developed to determine them based on a universal charge exchange cross section fit and Einstein A coefficients determined via the Autostructure code. A benchmarking exercise indicates that the new method accurately predicts the functional form of the effective emission coefficients. With this rate data in hand, the relative intensities of each CXRS line of sight can be accurately modeled with the pySTRAHL and pyFIDASIM codes.

By comparing synthetic signals simulated with the pySTRAHL code to the collected impurity emission data, the impurity diffusion and convection velocities could be inferred. The Bayesian framework utilized in this study allowed for a robust accounting of model uncertainties and their propagation to the uncertainties in the inferred impurity transport. It was seen that the consideration of the relative intensities of the CXRS lines of sight (enabled by the calculated effective emission coefficients) provided much stronger constraints on the impurity transport than when matching only the normalized signal intensities. In addition to the CXRS measurements, soft X-ray and bolometry measurements provided constraints on the impurity transport. When including these diagnostics in the inference framework along with the CXRS signals, it can be seen that uncertainties in the impurity diffusion and convection velocities are smaller than when considering any of the diagnostics on their own. Additional measurements of $C^{6+}$ density profiles are also found to be consistent with inferred transport profiles.

These results indicate a measured impurity diffusion profile which is relatively small in the core ($\sim$ 0.3 $m^2/s$) which becomes elevated near the edge region ($\sim$ 3 $m^2/s$). The inferred diffusion profile is quantitatively consistent with previous exper-

imental results [23], though one should note the difference in experimental conditions (the previous study was performed in plasmas with $T_{e,core} \approx 5$keV and $n_{e,core} \approx 2 \times 10^{19}$ m$^{-3}$). Additionally, results indicate an impurity pinch velocity in the edge region characterized by a peaking ratio of $\sim -5$. Previous gyrokinetic studies indicate that impurities affected by ITG turbulence would experience an inward pinch velocity[98], however, in order to validate these results, turbulence simulations would need to be performed for the experimental conditions considered in this work.

Finally, since the bolometer measurements strongly constrain the total impurity content, one can additionally infer the absolute magnitude of the calculated emission coefficients. Comparison to the ADAS database indicates good qualitative agreement with similar datasets.

## 8.2 Avenues for Future Work

The new diagnostic system has opened up a fresh set of capabilities for impurity studies at W7-X though additional improvements could be made to the spectroscopy system. Currently, in order to perform wavelength calibrations, the round to linear fiber bundles must be removed from their patch panel and illuminated with a calibration lamp. Since removing and replacing these fibers invalidates any intensity calibrations, a method to perform in-situ wavelength calibration is desired. Future designs for the dual fiber holders could allow for this by including a small $\sim$ 1mm gap either directly above or below the two fiber bundles which would allow one to slip in a bare, 100$\mu$m, fiber in and out of the optics without removing the fiber bundles. Additionally, the mechanical stability of the optics can be improved by replacing 3D printed parts with machined, metal components. In particular, the grating height block that fixes the grating holders to the rotational stage should be replaced since

the grating holders can potentially rotate if disturbed, ruining alignment. With a threaded metal height block, these grating holders would fasten tighter to the stage preventing this issue.

During the following experimental campaigns at W7-X, one interesting experiment would be to perform injection experiments at a variety of collisionalities. This could be accomplished by attempting to match the electron and ion temperature profiles between shots while scanning across different electron density values. Holding the temperatures constant would maintain a given $T_i/T_e$ and therefore the ITG turbulence characteristics. If TEM contributions become non-negligible, their degree of stability would be altered by the changing collisionality. TEM and ITG driven turbulence are predicted to exhibit different levels of transport, particularly the direction of the convective velocity [47]. Therefore, a detailed understanding of their contributions to the overall transport would be of interest when considering the screening of impurities from the core.

Additionally, previous experiments at W7-X have uncovered a regime of significantly reduced turbulence levels [99]. These conditions are achieved by primarily using NBI heating and systematically reducing the ECRH power input. In these conditions, it is found that anomalous contributions to the impurity transport are reduced below the neoclassical levels. These studies however impose several constraints on the impurity transport profiles. As such, it could be of great interest to validate these studies by simultaneously inferring the impurity D & V profiles using the Bayesian integrated data analysis framework presented in this thesis.

The suitability of this diagnostic framework has been demonstrated for experiments which inject Iron impurities. However, in principle, equation 38 is agnostic to the particular impurity species. This can be seen in the limited tungsten dataset presented in figure 34 which shows impurity lines that appear at the same wavelength

as the corresponding Fe charge states. Since many fusion experiments and power plant designs are planning to utilize tungsten first wall materials, the analysis of high-n Rydberg transitions could provide a flexible way to analyze the accumulation or screening of sputtered material.

Finally, section 7.2 discusses a method for experimental validation of effective charge exchange emission coefficients. The unique integrated data analysis approach allows one to constrain the overall impurity density, and therefore the emission strengths by comparing CX signals with total radiated power measurements. This approach can be applied to either the rates calculated using the method in this thesis or those determined via the ADAS codes. Experiments could be performed which vary the neutral beam acceleration energy to evaluate the effect of the neutral-impurity collision velocity on the CX cross sections.

# References

[1] C. Swee, B. Geiger, R. Albosta, O. Ford, S. Loch, M. D. Nornberg, J. Schellpheffer, T. Wegner, and W.-X. Team, "Design of a new charge exchange recombination spectroscopy diagnostic for impurity transport experiments at Wendelstein 7-X," *Review of Scientific Instruments*, vol. 93, no. 10, p. 103523, 2022.

[2] C. Swee, B. Geiger, R. Dux, S. T. A. Kumar, J. F. Castillo, A. Bader, and M. Gerard, "Impurity transport studies at the HSX stellarator using active and passive CVI spectroscopy," *Plasma Physics and Controlled Fusion*, vol. 64, no. 1, p. 015008, 2022.

[3] B. Geiger *et al.*, "Progress in modelling fast-ion D-alpha spectra and neutral particle analyzer fluxes using FIDASIM," *Plasma Physics and Controlled Fusion*, vol. 62, 2020.

[4] K. Moser, *Gaussian Processes for Emission Tomography at ASDEX Upgrade*. PhD thesis, "Max-Planck-Institut für Plasmaphysik", 2020.

[5] F. F. Chen, *Plasma physics*. Planum Press, 1984.

[6] J. Wesson, *Tokamaks*. Oxford Press, 2004. isbn: 9780199592234.

[7] D. Brown *et al.*, "Endf/b-viii.0: The 8th major release of the nuclear reaction data library with cielo-project cross sections, new standards and thermal scattering data," *Nuclear Data Sheets*, vol. 148, pp. 1–142, 2018. Special Issue on Nuclear Reaction Data.

[8] M. Jakobs, N. L. Cardozo, and R. Jaspers, "Fusion burn equilibria sensitive to the ratio," *Nuclear Fusion*, vol. 54, no. 12, pp. 2–7, 2014.

[9] A. Kallenbach *et al.*, "Impurity seeding for tokamak power exhaust: from present devices via iter to demo," *Plasma Physics and Controlled Fusion*, vol. 55, no. 12, p. 124041, 2013.

[10] G. Xu *et al.*, "Divertor impurity seeding with a new feedback control scheme for maintaining good core confinement in grassy-elm h-mode regime with tungsten monoblock divertor in east," *Nuclear Fusion*, vol. 60, no. 8, p. 086001, 2020.

[11] J. Gao *et al.*, "The effect of impurity seeding into the closed divertor on plasma detachment in the hl-2a tokamak," *Nuclear Fusion*, vol. 63, no. 3, p. 036006, 2023.

[12] G. Maddison *et al.*, "Moderation of divertor heat loads by fuelling and impurity seeding in well-confined elmy h-mode plasmas on jet," *Nuclear Fusion*, vol. 51, no. 4, p. 042001, 2011.

[13] T. Osborne *et al.*, "Enhanced h-mode pedestals with lithium injection in diii-d," *Nuclear Fusion*, vol. 55, no. 6, p. 063018, 2015.

[14] R. Maingi *et al.*, "Elm elimination with li powder injection in east discharges using the tungsten upper divertor," *Nuclear Fusion*, vol. 58, no. 2, p. 024003, 2018.

[15] R. Burhenn, Y. Feng, K. Ida, H. Maassberg, K. McCarthy, D. Kalinina, M. Kobayashi, S. Morita, Y. Nakamura, H. Nozato, S. Okamura, S. Sudo, C. Suzuki, N. Tamura, A. Weller, M. Yoshinuma, and B. Zurro, "On impurity handling in high performance stellarator/heliotron plasmas," *Nuclear Fusion*, vol. 49, no. 6, p. 065005, 2009.

[16] H. P. Summers, W. J. Dickson, M. G. O'Mullane, N. R. Badnell, A. D. Whiteford, D. H. Brooks, J. Lang, S. D. Loch, and D. C. Griffin, "Ionization state, excited populations and emission of impurities in dynamic finite density plasmas: I. the generalized collisional–radiative model for light elements," *Plasma Physics and Controlled Fusion*, vol. 48, no. 2, pp. 263–293, 2006.

[17] T. Pütterich, E. Fable, R. Dux, M. O'Mullane, R. Neu, and M. Siccinio, "Determination of the tolerable impurity concentrations in a fusion reactor using a consistent set of cooling factors," *Nuclear Fusion*, vol. 59, no. 5, p. 056013, 2019.

[18] "Flux surface." `http://fusionwiki.ciemat.es/wiki/Flux_surface`.

[19] A. H. Boozer, "Physics of magnetically confined plasmas," *Rev. Mod. Phys.*, vol. 76, pp. 1071–1141, 2005.

[20] J. Spitzer, Lyman, "The Stellarator Concept," *The Physics of Fluids*, vol. 1, no. 4, pp. 253–264, 1958.

[21] G. Xu, Z. Lu, D. Chen, and B. Wan, "A promising approach to steady-state fusion: High-temperature superconducting strong-field stellarator with precise omnigenity," *The Innovation*, vol. 5, no. 1, p. 100537, 2024.

[22] J. F. Castillo, C. Clark, A. Bader, K. M. Likin, D. T. Anderson, B. Geiger, S. T. A. Kumar, and C. Swee, "Laser blow-off with photodiode detection system at the helically symmetric experiment," *Journal of Instrumentation*, vol. 16, no. 11, 2021.

[23] B. Geiger *et al.*, "Observation of anomalous impurity transport during low-density experiments in W7-X with laser blow-off injections of iron," *Nuclear Fusion*, vol. 59, no. 4, 2019.

[24] T. Wegner *et al.*, "Impact of the temperature ratio on turbulent impurity transport in Wendelstein 7-X," *Nuclear Fusion*, vol. 60, no. 12, 2020.

[25] L.-M. Imbert-Gerard, E. J. Paul, and A. M. Wright, "An introduction to stellarators: From magnetic fields to symmetries and optimization," *arXiv preprint arXiv:1908.05360*, 2019.

[26] N. Mcgreivy, *Classical , Neoclassical , and Anamolous Transport*. 2018. available at: https://nickmcgreivy.scholar.princeton.edu/sites/g/files /toruqf5041/files /nickmcgreivy/files/classical_neoclassical_and_anamolous_transport_notes-2.pdf.

[27] P. Helander *et al.*, "Stellarator and tokamak plasmas: A comparison," *Plasma Physics and Controlled Fusion*, vol. 54, no. 12, 2012.

[28] M. Hirsch *et al.*, "Major results from the stellarator wendelstein 7-as," *Plasma Physics and Controlled Fusion*, vol. 50, p. 053001, mar 2008.

[29] F. S. Anderson, A. F. Almagri, D. T. Anderson, P. G. Matthews, J. N. Talmadge, and J. L. Shohet, "Helically symmetric experiment, (hsx) goals, design and status," *Fusion Technology*.

[30] C. D. Beidler and et. al, "Demonstration of reduced neoclassical energy transport in wendelstein 7-x," *Nature*, vol. 596, no. 7871, pp. 221–226, 2021.

[31] M. Landreman and E. Paul, "Magnetic fields with precise quasisymmetry for plasma confinement," *Phys. Rev. Lett.*, vol. 128, p. 035001, 2022.

[32] C. D. Beidler *et al.*, "Benchmarking of the mono-energetic transport coefficients - Results from the International Collaboration on Neoclassical Transport in Stellarators (ICNTS)," *Nuclear Fusion*, vol. 51, no. 7, 2011.

[33] A. N. Kolmogorov, "The local structure of turbulence in incompressible viscous fluid for very large reynolds numbers," *Proceedings: Mathematical and Physical Sciences*, vol. 434, no. 1890, pp. 9–13, 1991.

[34] F. Wagner and U. Stroth, "Transport in toroidal devices the experimentalist's view," *Plasma Physics and Controlled Fusion*, vol. 35, no. 10, 1993.

[35] P. H. Diamond, S.-I. Itoh, K. Itoh, and T. S. Hahm, "Zonal flows in plasma—a review," *Plasma Physics and Controlled Fusion*, vol. 47, no. 5, p. R35, 2005.

[36] B. B. Kadomtsev, O. P. Pogutse, and I. V. Kurchatov, "Trapped particles in toroidal magnetic systems," *Nuclear Fusion*, vol. 11, no. 1, pp. 67–92, 1971.

[37] W. Stacey, *Fusion Plasma Physics*. Wiley, 2005. isbn: 978-3-527-61874-3.

[38] W. Horton, D. I. Choi, and W. M. Tang, "Toroidal drift modes driven by ion pressure gradients," *Physics of Fluids*, vol. 24, no. 6, pp. 1077–1085, 1981.

[39] A. Mariani, P. Mantica, S. Brunner, M. Fontana, A. Karpushov, C. Marini, L. Porte, O. Sauter, the TCV Team, and the EUROfusion MST1 Team, "Investigation of the role of electron temperature gradient modes in electron heat transport in tcv plasmas," *Nuclear Fusion*, vol. 59, no. 12, p. 126017, 2019.

[40] G. Weir *et al.*, "Heat pulse propagation and anomalous electron heat transport measurements on the optimized stellarator w7-x," *Nuclear Fusion*, vol. 61, no. 5, p. 056001, 2021.

[41] J. H. E. Proll, P. Helander, J. W. Connor, and G. G. Plunk, "Resilience of quasi-isodynamic stellarators against trapped-particle instabilities," *Phys. Rev. Lett.*, vol. 108, p. 245002, 2012.

[42] J. A. Alcusón, P. Xanthopoulos, G. G. Plunk, P. Helander, F. Wilms, Y. Turkin, A. V. Stechow, and O. Grulke, "Suppression of electrostatic micro-instabilities in maximum-J stellarators," *Plasma Physics and Controlled Fusion*, vol. 62, no. 3, 2020.

[43] O. Ford *et al.*, "Turbulence-reduced high-performance scenarios in wendelstein 7-x," *Nuclear Fusion*, vol. 64, p. 086067, jul 2024.

[44] I. G. Abel, G. G. Plunk, E. Wang, M. Barnes, S. C. Cowley, W. Dorland, and A. A. Schekochihin, "Multiscale gyrokinetics for rotating tokamak plasmas: Fluctuations, transport and energy flows," *Reports on Progress in Physics*, vol. 76, no. 11, 2013.

[45] F. Merz, *Gyrokinetic Simulation of Multimode Plasma Turbulence.* thesis, Westfälische Wilhelms-Universität Münster, 2008.

[46] I. J. McKinney, M. J. Pueschel, B. J. Faber, C. C. Hegna, J. N. Talmadge, D. T. Anderson, H. E. Mynick, and P. Xanthopoulos, "A comparison of turbulent transport in a quasi-helical and a quasi-axisymmetric stellarator," *Journal of Plasma Physics*, vol. 85, no. 5, pp. 1–22, 2019.

[47] J. M. Garcia-Regaña *et al.*, "Turbulent impurity transport simulations in Wendelstein 7-X plasmas," *Journal of Plasma Physics*, vol. 87, 2021.

[48] J. Nührenberg, "Development of quasi-isodynamic stellarators," *Plasma Physics and Controlled Fusion*, vol. 52, no. 12, pp. 1–7, 2010.

[49] C. Beidler *et al.*, "Physics and engineering design for wendelstein vii-x," *Fusion Technology*, vol. 17, no. 1, pp. 148–168, 1990.

[50] T. Andreeva *et al.*, "Magnetic configuration scans during divertor operation of wendelstein 7-x," *Nuclear Fusion*, vol. 62, no. 2, p. 026032, 2022.

[51] A. H. Boozer, "Transport and isomorphic equilibria," *Physics of Fluids*, vol. 26, no. 2, pp. 496–499, 1983.

[52] T. Klinger *et al.*, "Overview of first wendelstein 7-x high-performance operation," *Nuclear Fusion*, vol. 59, no. 11, p. 112004, 2019.

[53] T. S. Pedersen *et al.*, "First results from divertor operation in wendelstein 7-x," *Plasma Physics and Controlled Fusion*, vol. 61, no. 1, p. 014035, 2018.

[54] R. C. Wolf *et al.*, "Electron-cyclotron-resonance heating in wendelstein 7-x: A versatile heating and current-drive method and a tool for in-depth physics studies," *Plasma Physics and Controlled Fusion*, vol. 61, p. 014037, nov 2018.

[55] T. Stange *et al.*, "Advanced electron cyclotron heating and current drive experiments on the stellarator wendelstein 7-x," *EPJ Web Conf.*, vol. 157, p. 02008, 2017.

[56] M. Machielsen, J. Graves, H. Patten, C. Slaby, and S. Lazerson, "Fast ion generation by combined rf-nbi heating in w7-x," *Journal of Plasma Physics*, vol. 89, no. 2, p. 955890202, 2023.

[57] P. Z. Poloskei, B. Geiger, A. J. van Vuuren, S. Äkäslompolo, O. Ford, A. Spanier, T. Neelis, P. McNeely, D. Hartmann, and the W7-X Team, "Experimental characterization of the active and passive fast-ion h-alpha emission in w7-x using fidasim," *Nuclear Fusion*, vol. 64, no. 2, p. 026008, 2023.

[58] P. McNeely *et al.*, "Commissioning and initial operation of the w7-x neutral beam injection heating system," *Fusion Engineering and Design*, vol. 161, p. 111997, 2020.

[59] T. Romba, "Validation of the w7-x cxrs for impurity density profiles," thesis, Eindhoven University of Technology, 2021.

[60] S. A. Bozhenkov *et al.*, "The thomson scattering diagnostic at wendelstein 7-x and its performance in the first operation phase," *Journal of Instrumentation*, vol. 12, no. 10, 2017.

[61] T. Wegner *et al.*, "Design, capabilities, and first results of the new laser blow-off system on Wendelstein 7-X," *Review of Scientific Instruments*, vol. 89, no. 7, 2018.

[62] T. Wegner and F. Kunkel, "Development of a new manipulator for the laser blow-off system at wendelstein 7-x," *Fusion Engineering and Design*, vol. 193, p. 113691, 2023.

[63] W. Biel and A. Greiche, "High efficiency extreme ultraviolet overview spectrometer: Construction and laboratory testing," *Review of Scientific Instruments*, vol. 77, no. 10, 2006.

[64] R. J. Fonck, A. T. Ramsey, and R. V. Yelle, "Multichannel grazing-incidence spectrometer for plasma impurity diagnosis: Spred," *Appl. Opt.*, vol. 21, no. 12, pp. 2115–2123, 1982.

[65] D. Zhang *et al.*, "Bolometer tomography on wendelstein 7-x for study of radiation asymmetry," *Nuclear Fusion*, vol. 61, no. 11, p. 116043, 2021.

[66] H. Meister, M. Willmeroth, D. Zhang, A. Gottwald, M. Krumrey, and F. Scholze, "Broad-band efficiency calibration of iter bolometer prototypes using pt absorbers on sin membranes," *Review of Scientific Instruments*, vol. 84, no. 12, 2013.

[67] L. Giannone, K. Mast, and M. Schubert, "Derivation of bolometer equations relevant to operation in fusion experiments," *Review of Scientific Instruments*, vol. 73, pp. 3205–3214, 09 2002.

[68] O. P. Ford *et al.*, "Charge exchange recombination spectroscopy at wendelstein 7-x," *Review of Scientific Instruments*, vol. 91, no. 2, 2020.

[69] C. Swee, B. Geiger, O. Ford, M. Nornberg, M. O'Mullane, P. Poloskei, F. Reimold, T. Romba, T. Wegner, and the W7-X Team, "Impurity transport study based on measurement of visible wavelength high-n charge exchange transitions at w7-x," *Nuclear Fusion*, vol. 64, p. 086062, jul 2024.

[70] P. Linstrom and W. Mallard, *NIST Chemistry WebBook, NIST Standard Reference Database Number 69*. Gaithersburg MD, 20899: National Institute of Standards and Technology. available at: https://doi.org/10.18434/T4D303.

[71] K. Igenbergs, J. Schweinzer, A. Veiter, L. Perneczky, E. Frühwirth, M. Wallerberger, R. E. Olson, and F. Aumayr, "Charge exchange and ionization in $N^{7+}$ -, $N^{6+}$ - $C^{6+}$-H(n=2,1) collisions studied systematically by theoretical approaches," *J. Phys. B*, vol. 45, no. 6, p. 065203, 2012.

[72] C. Johnson, S. Loch, and D. Ennis, "Colradpy: A python collisional radiative solver," *Nuclear Materials and Energy*, vol. 20, p. 100579, 2019.

[73] N. Šibalić and C. S. Adams, *Rydberg Physics*. 2399-2891, IOP Publishing, 2018. isbn: 978-0-7503-1635-4.

[74] A. Thorman *et al.*, "Visible spectroscopy of highly charged tungsten ions with the jet charge exchange diagnostic," *Physica Scripta*, vol. 96, no. 12, p. 125631, 2021.

[75] E. Haug, "The relativistic rydberg's formula in greater depth and for any atom," *Modern Physics*, vol. 11, no. 4, 2020.

[76] R. E. Olson *Physical Review A*, vol. 24, no. 4, pp. 1726–1733, 1981.

[77] R. Bussiahn, N. Tamura, K. J. McCarthy, R. Burhenn, H. Hayashi, R. Laube, T. Klinger, L. E. Group, and W.-X. Team, "Tracer-Encapsulated Solid Pellet (TESPEL) injection system for Wendelstein 7-X," *Review of Scientific Instruments*, vol. 89, p. 10K112, 10 2018.

[78] M. Arnaud and J. Raymond, "Iron ionization and recombination rates and ionization equilibrium," *Journ. Astrophysics*, vol. 398, p. 394, 1992.

[79] U. Von Toussaint, "Bayesian inference in physics," *Reviews of Modern Physics*, vol. 83, no. 3, pp. 943–999, 2011.

[80] A. E. Gelfand, S. E. Hills, A. Racine-Poon, and A. F. M. Smith, "Illustration of bayesian inference in normal data models using gibbs sampling," *Journal of the American Statistical Association*, vol. 85, no. 412, pp. 972–985, 1990.

[81] W. K. Hastings, "Monte Carlo sampling methods using Markov chains and their applications," *Biometrika*, vol. 57, no. 1, pp. 97–109, 1970.

[82] D. Foreman-Mackey, D. W. Hogg, D. Lang, and J. Goodman, "emcee : The MCMC Hammer ," *Publications of the Astronomical Society of the Pacific*, vol. 125, no. 925, pp. 306–312, 2013.

[83] J. Goodman and J. Weare, "Ensemble Samplers With Affine Invariance," *Communications in Applied Mathematics and Computational Science*, vol. 5, no. 1, pp. 65–80, 2010.

[84] F. N. Fritsch and R. E. Carlson, "Monotone piecewise cubic interpolation," *SIAM Journal on Numerical Analysis*, vol. 17, no. 2, pp. 238–246, 1980.

[85] S. N. Nahar, A. K. Pradhan, and H. L. Zhang, "Electron-ion recombination rate coefficients and photoionization cross sections for astrophysically abundant elements. v. relativistic calculations for fe xxiv and fe xxv for x-ray modeling," *The Astrophysical Journal Supplement Series*, vol. 133, no. 1, p. 255, 2001.

[86] R. Dux, *STRAHL User Manual*. "Max-Planck-Institut für Plasmaphysik", 2018.

[87] S. P. Hirshman and H. K. Meier, "Optimized fourier representations for three-dimensional magnetic surfaces," *The Physics of Fluids*, vol. 28, no. 5, pp. 1387–1391, 1985.

[88] C. Killer *et al.*, "Characterization of the w7-x scrape-off layer using reciprocating probes," *Nuclear Fusion*, vol. 59, no. 8, p. 086013, 2019.

[89] J. Crank and P. Nicolson, "A practical method for numerical evaluation of solutions of partial differential equations of the heat-conduction type," *Mathematical Proceedings of the Cambridge Philosophical Society*, vol. 43, no. 1, p. 50–67, 1947.

[90] K. Behringer, "Description of the impurity transport code 'strahl'," tech. rep., IAEA, 1987.

[91] W. W. Heidbrink, D. Liu, Y. Luo, E. Ruskov, and B. Geiger, "A Code that Simulates Fast-Ion D$\alpha$ and Neutral Particle Measurements," *Communications in Computational Physics*, vol. 10, no. 3, p. 716–741, 2011.

[92] B. Geiger, A. Edmondson, M. Gerard, L. Henning, S. T. A. Kumar, P. Poloskei, and C. Swee, "pyFIDASIM simulations of the neutral density and charge-exchange losses in the HSX stellarator," in *TTF conference proceedings*, vol. 2021, 2021.

[93] R. McDermott, R. Dux, F. Guzman, T. Pütterich, R. Fischer, A. Kappatou, and the ASDEX Upgrade team, "Development of ar$^{+16}$ charge exchange recombination spectroscopy measurements at asdex upgrade," *Nuclear Fusion*, vol. 61, no. 1, p. 016019, 2020.

[94] A. Foster, *On the behaviour and radiating properties of heavy elements in Fusion Plasmas*. PhD thesis, University of Strathclyde, 2009.

[95] N. R. Badnell, "Dielectronic recombination of fe22+ and fe21+," *Journal of Physics B: Atomic and Molecular Physics*, vol. 19, no. 22, p. 3827, 1986.

[96] Autostructure available at: http://amdpp.phys.strath.ac.uk/autos/.

[97] D. A. Spong, "Generation and damping of neoclassical plasma flows in stellarators," *Physics of Plasmas*, vol. 12, no. 5, p. 056114, 2005.

[98] García-Regaña *et al.*, "Turbulent impurity transport simulations in wendelstein 7-x plasmas," *Journal of Plasma Physics*, vol. 87, no. 1, p. 855870103, 2021.

[99] T. Romba, F. Reimold, R. Jaspers, O. Ford, L. Vanó, T. Klinger, and the W7-X Team, "Suppression of anomalous impurity transport in nbi-heated w7-x plasmas," *Nuclear Fusion*, vol. 63, no. 7, p. 076023, 2023.

# A Validation of Inferred Impurity Transport Results via a Second Experiment

In order to validate the impurity transport inference result, a second discharge (20230314.22) was analyzed with very similar experimental conditions to discharge 20230314.26. An overview summary of discharge 20230314.22 is given in figure 64 for which the impurity injection occurs at 3.6 seconds. The kinetic profiles during the LBO injection are given in 65. The most notable difference in the plasma conditions in this case is the electron density profile which is larger by $\sim 30\%$.

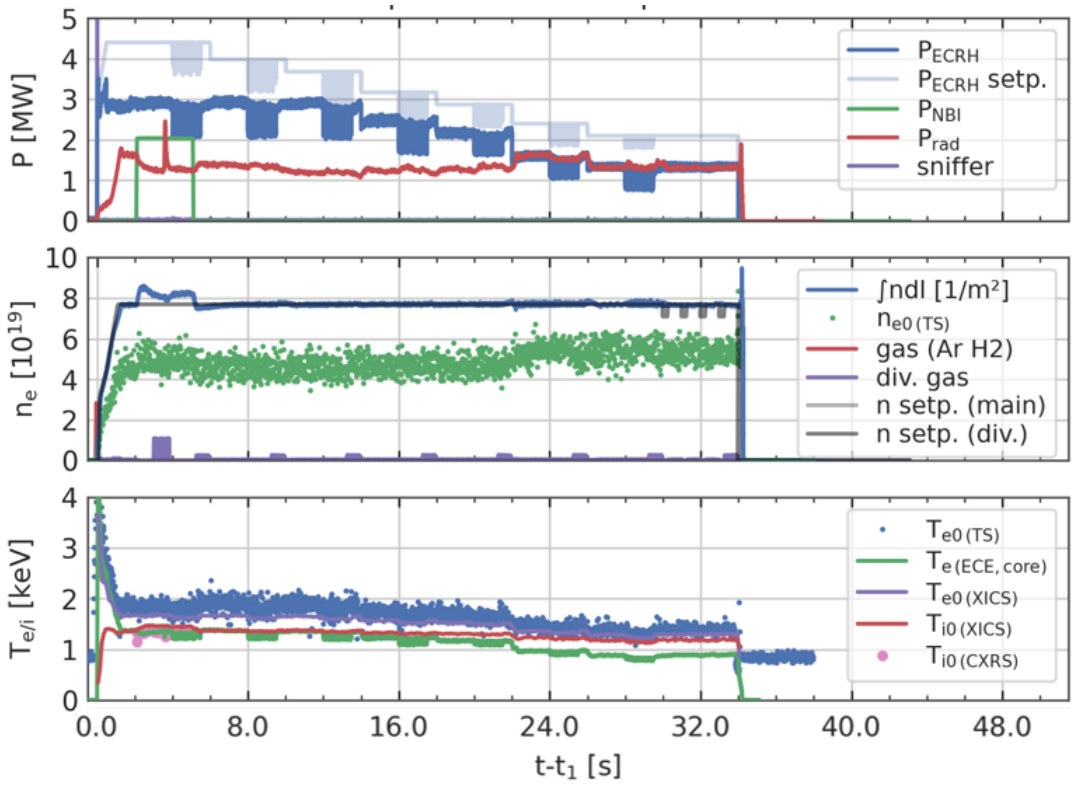


Figure 64: Overview of experiment 20230314.22. ECRH power and radiated power are shown in the top panel, electron densities are shown in the middle panel, and electron temperatures are shown in the bottom panel. The iron injection takes place at 3.6 s.

CXRS, HEXOS, and Bolometer data has also been collected for discharge 22 and

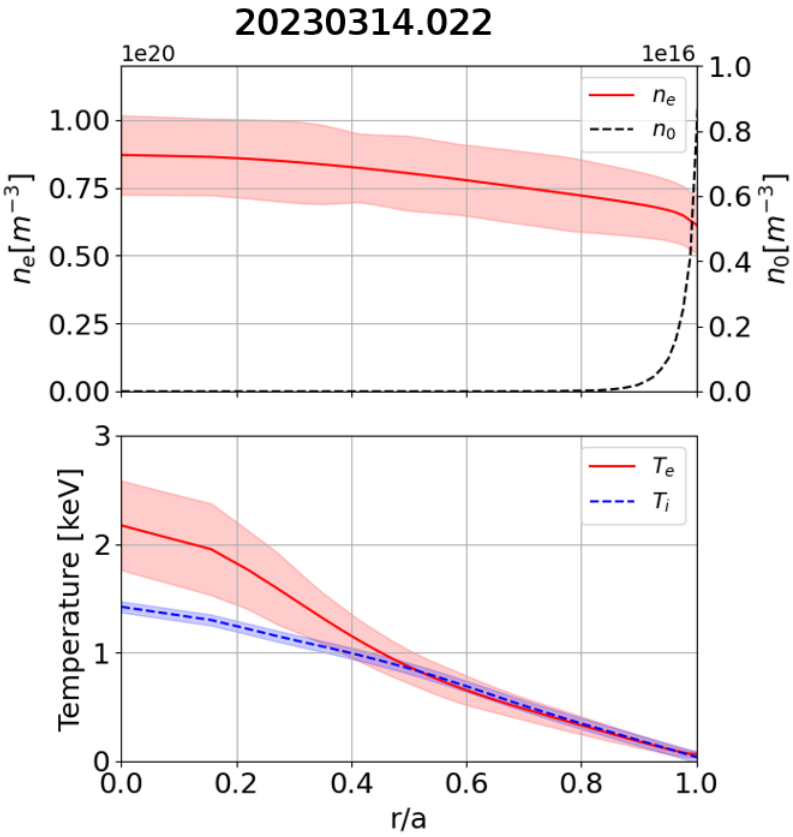


Figure 65: Electron density, electron temperature, and ion temperature along with neutral density profiles calculated using pyfidasim. Uncertainties are given by shaded regions around the fitted profiles.

is shown in figures 66, 67, and 68 respectively.

The inferred impurity diffusion and convection velocities for the two compared shots (22 and 26) are given in figure 69. Notably, the two datasets are explained by very similar transport profiles. Qualitatively, it seems that shot 26 has a more pronounced inward pinch velocity near the edge of the plasma compared to shot 22 however this difference can be well explained by the fitting uncertainties. Besides this, the two results show good agreement in the inferred transport profiles.

Since the two discharges share nearly matched experimental conditions and their analysis leads to the same inferred D and rV/D profiles, their comparison indicates

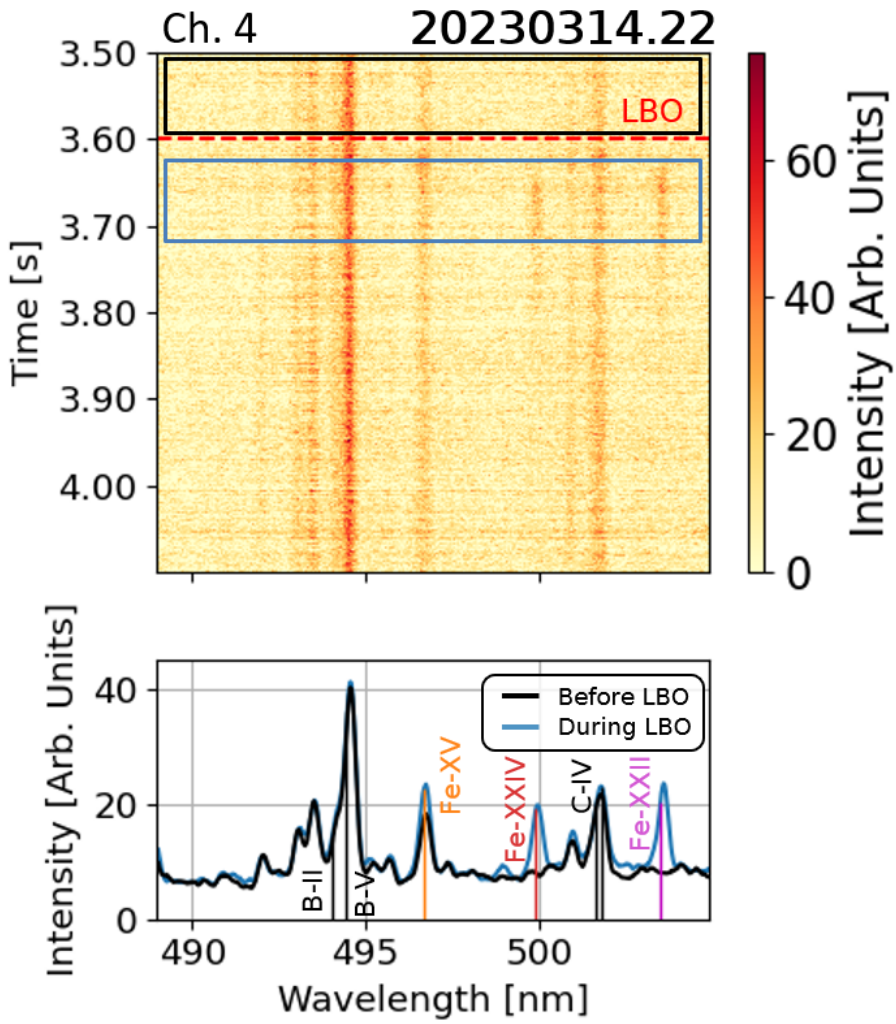


Figure 66: CXRS data originating from the WISC spectrometers (channel 4) for discharge 20230314.22. The top plot shows the intensity in the color scale versus time and wavelength. The time at which the impurity injection is indicated by a dashed red line. The bottom plot shows the averaged spectra over the time windows depicted by the boxes in the top plot.

that the presented method for inferring the impurity transport is well validated.

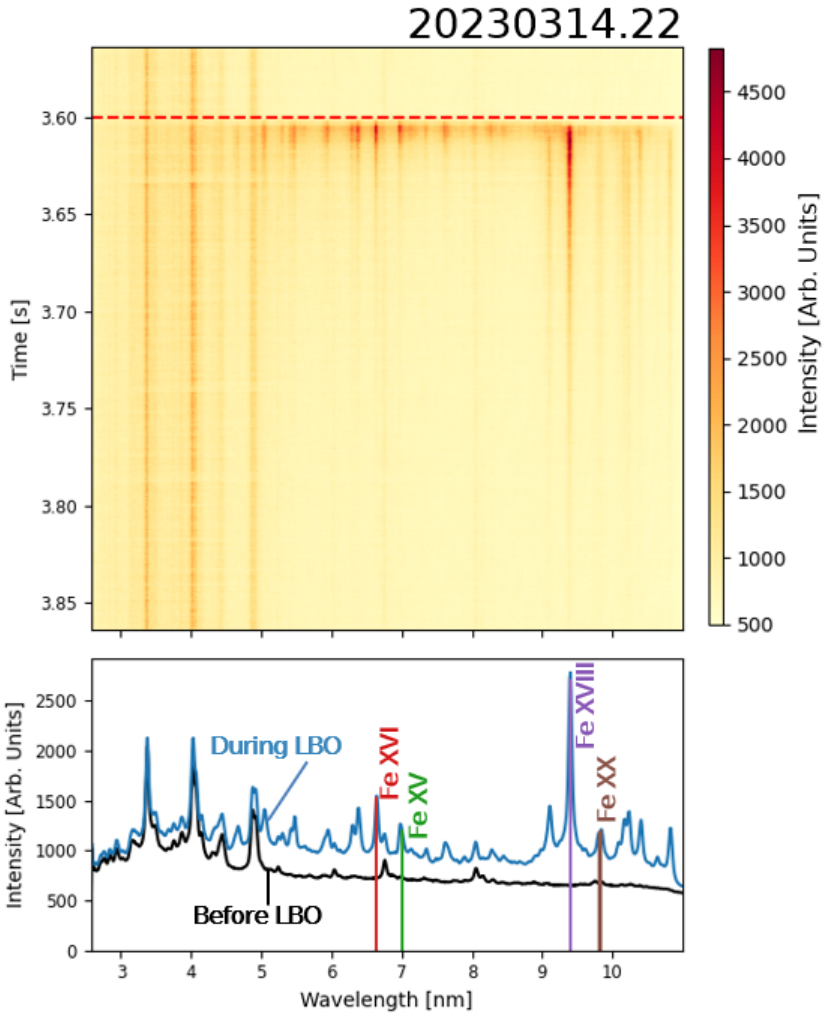


Figure 67: Top: Raw HEXOS signal from shot 20230314.22 depicting presence of X-Ray emission following LBO injection. Bottom: Time averaged spectra before and during the LBO event.

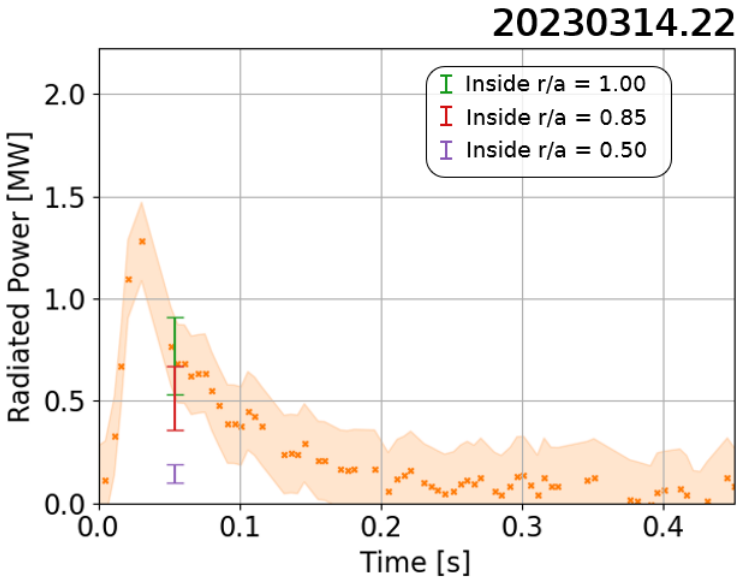


Figure 68: Total radiated power inside of $r/a = 1.0$ shown with orange x's and uncertainty depicted with shaded orange. Radiation fraction measurements are shown during the impurity injection with the error-bars for radiation inside of $r/a = 1.0$, 0.85, and 0.5.

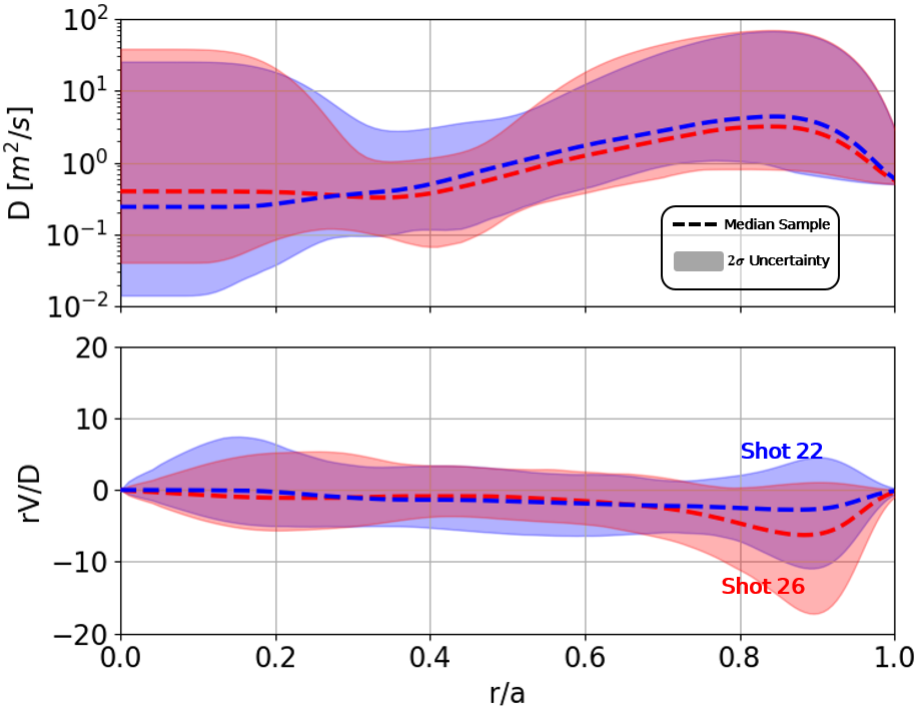


Figure 69: Comparison of inferred impurity diffusion and convection velocities for discharges 22 and 26.

# B Summary of Measured and Inferred Impurity Signals

Section 7.2 a total of 7 inferences in order to compare and contrast the fitting uncertainties when considering different combinations of diagnostics. Each of these inferences produced 1-3 figures describing the fitted diagnostic signals. In total, 11 of these figures were generated though their inclusion in the main text body is not necessary for the interpretation of the study results. Rather, these figures are curated below for reference.

## B.1 Normalized and Relatively Calibrated CXRS Measurements

Fitted CXRS signals for the case of normalized signals and relatively calibrated signals are shown in in figures 53 and 54 respectively.

## B.2 HEXOS Only

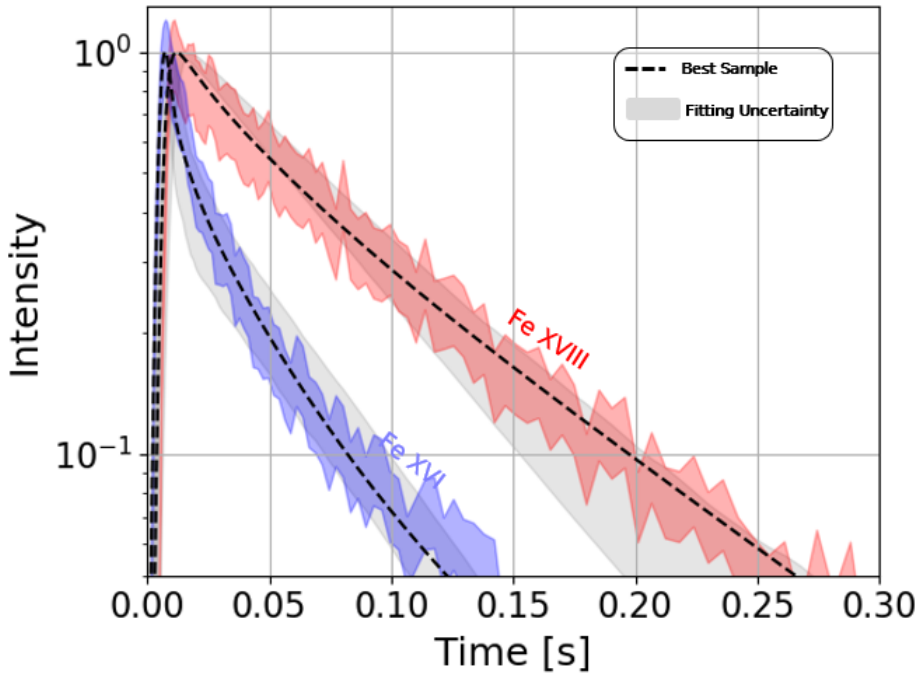


Figure 70: Fitted Fe XVI and Fe XVIII signals when only the HEXOS signals are included in the inference framework. The dashed black lines indicate the forward model from the posterior sample with the highest probability. Experimental uncertainty is given by the shaded region with fitting uncertainty given by the shaded gray.

## B.3 HEXOS and CXRS

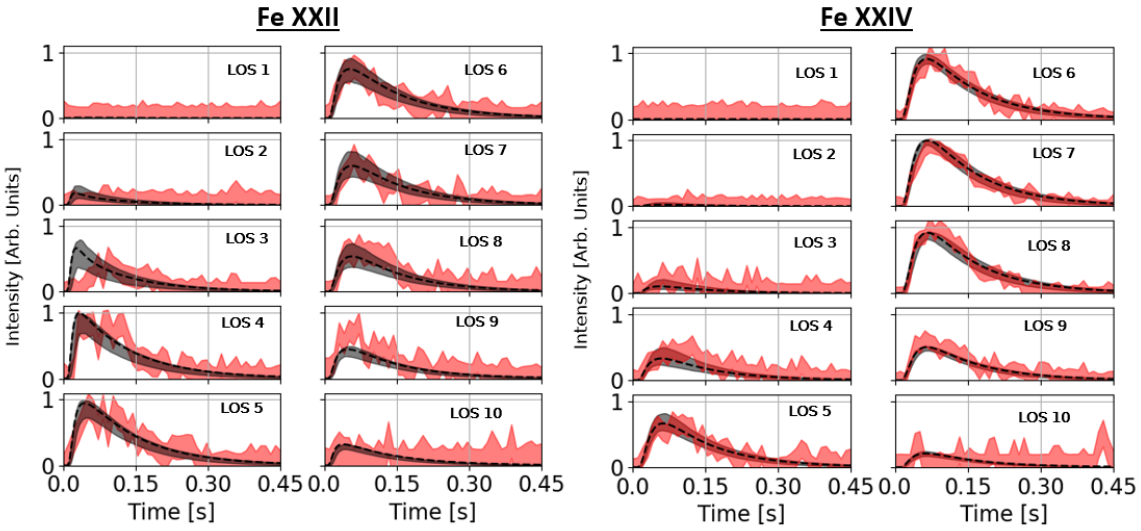


Figure 71: Synthetic signals matched to CXRS data when simultaneously matching HEXOS signals. The data has been normalized to the brightest signal. Experimental uncertainty is given by shaded red with fitting uncertainty shown in shaded grey. The dashed black lines indicate the forward model from the posterior sample with the highest probability. Data from discharge 20230314.26

The fitted HEXOS signals when simultaneously considering CXRS signals is given in figure 56

## B.4 Bolometer Only

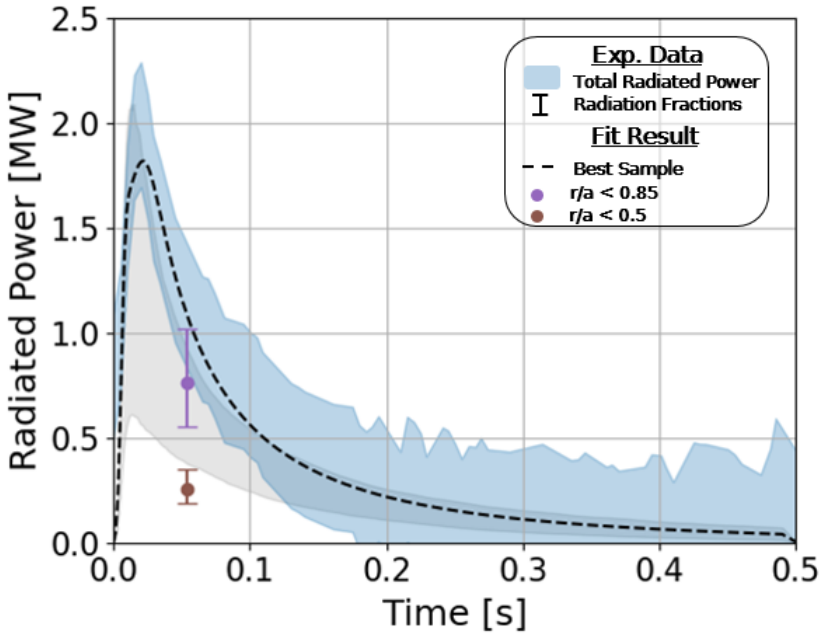


Figure 72: Fitted bolometer signal when fitted by itself. The dashed black line and the circular markers indicate the forward model from the posterior sample with the highest probability.

## B.5 Bolometer and CXRS

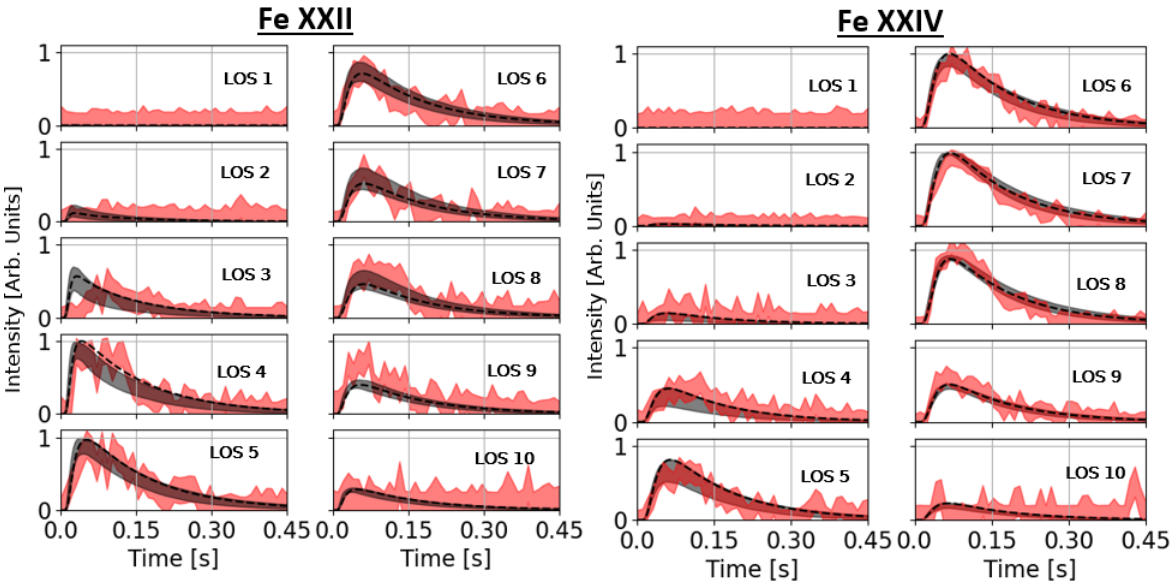


Figure 73: Synthetic signals matched to CXRS data when simultaneously matching Bolometer signals. The data has been normalized to the brightest signal. Experimental uncertainty is given by shaded red with fitting uncertainty shown in shaded grey. The dashed black lines indicate the forward model from the posterior sample with the highest probability. Data from discharge 20230314.26

The fitted bolometer signal when simultaneously considering CXRS signals is given in figure 58.

## B.6 Bolometer, HEXOS, and CXRS

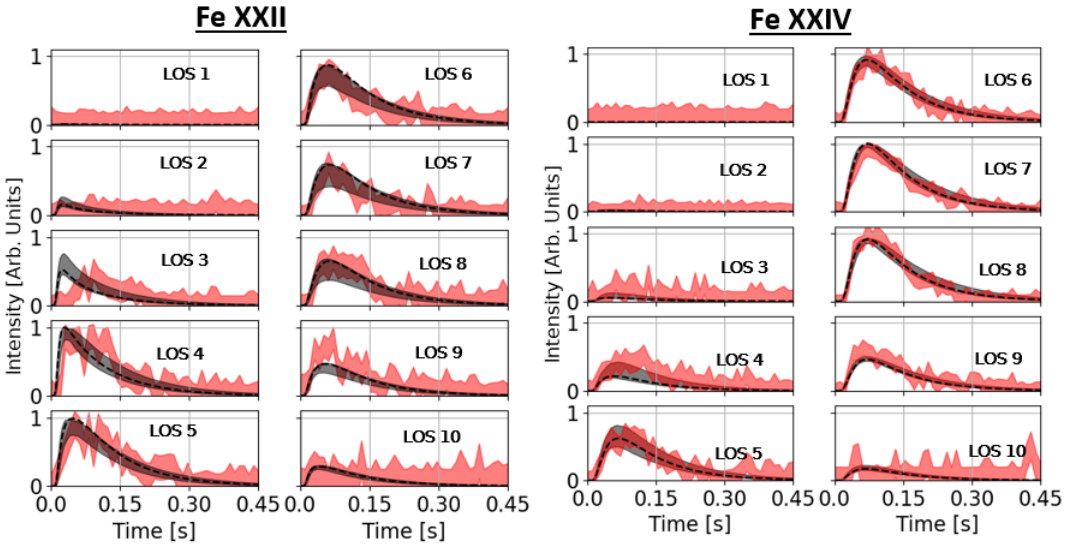


Figure 74: Synthetic signals matched to CXRS data when simultaneously matching Bolometer and HEXOS signals. The data has been normalized to the brightest signal. Experimental uncertainty is given by shaded red with fitting uncertainty shown in shaded grey. The dashed black lines indicate the forward model from the posterior sample with the highest probability. Data from discharge 20230314.26

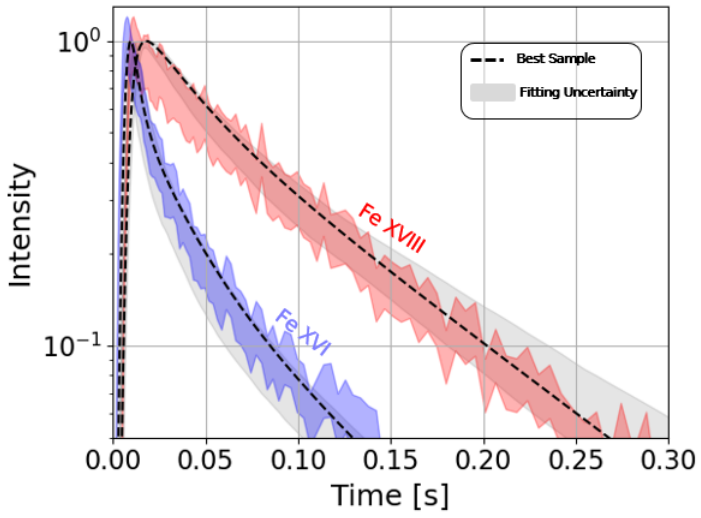


Figure 75: Fitted Fe XVI and Fe XVIII signals when simultaneously fitting CXRS, HEXOS, and Bolometer signals. The dashed black lines indicate the forward model from the posterior sample with the highest probability. Experimental uncertainty is given by the shaded region with fitting uncertainty given by the shaded gray.

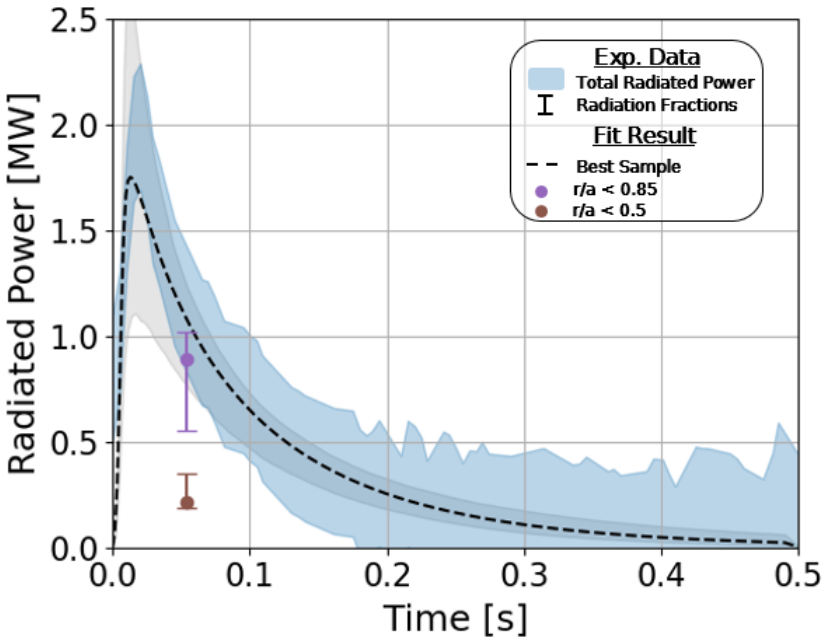


Figure 76: Fitted bolometer signal when fitted alongside CXRS and HEXOS measurements. The dashed black line and the circular markers indicate the forward model from the posterior sample with the highest probability.